Theoretical Study of Metal-Insulator Transition and Antiferromagnetism in Hubbard Model on Honeycomb Lattice

(ハニカム格子上ハバード模型に於ける金属 - 絶縁体転移と反強磁性の理論的研究)

Tomoya Ueda
(上田 倫也)

Department of Physics, Graduate School of Science
Osaka University

December 2010

Acknoledgements

I would like to express my deep and sincere gratitude to Prof. Tetsuo Ogawa for his invaluable guidance and encouragement during the course of my study. I am greatly indebted to Prof. Kenichi Asano and Prof. Takuma Ohashi for providing me with many suggestive advices and for supporting me in various ways to pursue my study throughout the years. Without their infinite and fruitful help, this work would not have been done. I also thank Prof. Hisazumi Akai, Prof. Yasuhiro Akutsu and Prof. Macoto Kikuchi for examining the present thesis and for giving me a lot of constructive comments. Last but not least I wish to thank my parents and sister for their hearty and unconditional support.

Contents

Chapter 1

Introduction

The discovery of the heavy fermion compounds and of the high-temperature superconductors has revived interest in strong correlations between electrons. It has been recognized that the many-body effects ascribable to the Coulomb interaction between electrons mutate the behavior of systems radically. These systems, where the electron-electron interaction is essentially important, are called *strongly correlated electron systems*, and have provided one of the most active research fields. One of intriguing phenomena in strongly correlated electron systems is the Mott transition, which is the metal-insulator transition caused by the Coulomb repulsion between electrons. It is a fundamental phenomenon of condensed matter physics, however, has not yet been well-understood. The first sample of the Mott insulator NiO was discovered in the last 1930s and then many kinds of transition metal oxides have been found to be the Mott insulators. Various two-dimensional organic compounds which show the Mott transition have also been discovered. In particular, the family of κ-(BEDT-TTF)$_2X$ has an anisotropic triangular lattice structure and this system is regarded as the strongly correlated system with geometrical frustration. One of novel features of these frustrated systems is the spin liquid ground state. Some of κ-type organics show the Mott transition under pressure but do not show any signals of magnetic ordering in the insulating phase at very low temperature. Therefore, these compounds are expected to have a novel spin liquid ground state, which might be a key to reveal Mott physics. Another interesting two-dimensional system is the honeycomb lattice system. The honeycomb lattice has the least coordinate number among two-dimensional systems and strong quantum fluctuations. Furthermore, this lattice provides a nontrivial dispersion relation in the electron motion and the single electron density of states. A typecal example of honeycomb lattice systems is graphene. This system has been intensively studied both experimentally and theoretically and a lot of exotic electronic properties have

been reported. Interaction effects on the honeycomb lattice system have been studied by means of the mean field theory for the Hubbard Hamiltonian and they have been revealed that the metallic ground state without long-range order appears at half filling due to its peculiar density of states. Therefore, in the honeycomb lattice Hubbard model, the Mott transition might occur not accompanied by antiferromagnetic order and there might be the spin liquid ground state. This is a very interesting problem.

In this chapter, we first outline the Mott transition and introduce a typical Mott insulator V_2O_3 in the next section. In the section 1.2, we briefly review geometrical frustration in the triangular lattice organic materials κ-(BEDT-TTF)$_2X$ as an example of correlation systems with frustration. In the section 1.3, we introduce honeycomb lattice systems and its physics. Finally, we present the purpose of this study in the section 1.4.

1.1 Mott Transition

The studies on the Mott transition have come on the discoveries of the insulating behavior of transition metal oxides such as NiO, which is expected to be metallic within the band theory. In the band theory, the dispersion relation of electrons is determined by the kinetic energy and periodic potential induced by atoms. If the energy band where the Fermi level lies is seperated by the band gap and is fully occupied by electrons, the system is regarded as an insulator because electrons cannot be excited by infinitesimal energy. Particularly in single band systems, this indicates that if the electron number per unit cell is odd, the system is metallic, and the even number of electrons per unit cell gives an insulator. Nonetheless, many of insulating transition metal oxides are half filled, namely only a half of its band is filled with electrons, and hence the band theory cannot explain this phenomenon. Mott and Slater have independently suggested their theories for this problem. Mott pointed out that insulating state with a half-filled band could be realized by the strong electron-electron repulsion which localizes the electrons around each atom [1, 2]. In contrast, Slater focused on the fact that many of Mott insulators are accompanied with magnetic order and argued that the Mott insulator is stabilized by the band gap induced by long-range order such as antiferromagnetic order with translational symmetry breaking which folds the Brillouin zone [3].

One of the minimal model to study the Mott transition is the Hubbard model, which is given as

$$H = \sum_{i,j,\sigma} t_{ij} c^{\dagger}_{i\sigma} c_{j\sigma} + U \sum_{i} n_{i\uparrow} n_{i\downarrow}, \tag{1.1}$$

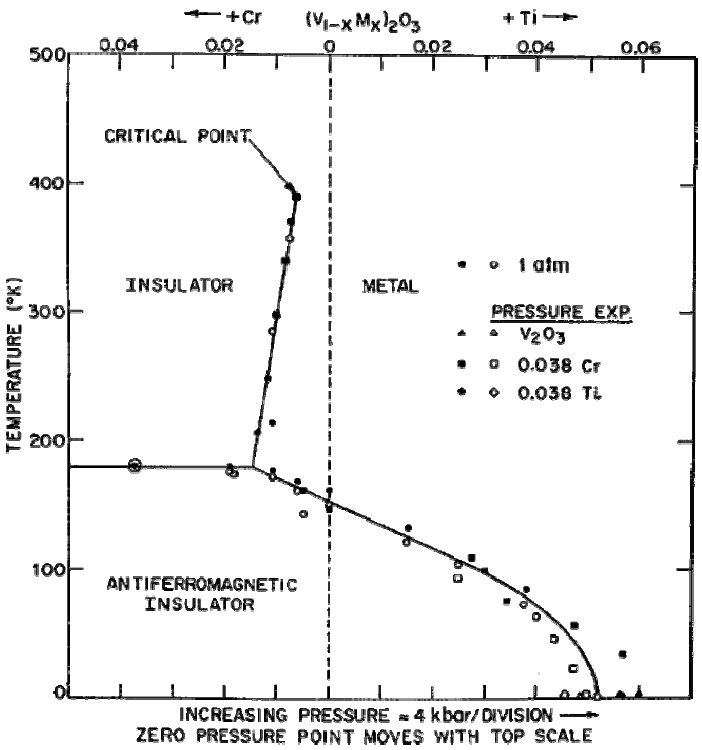

Figure 1.1: Phase diagram in V_2O_3 as a function of doping with Cr or Ti and as a function of pressure [5]. The closed and open symbols are for increasing and decreasing pressure or temperature. Increasing pressure corresponds to decreasing U/W. There is an empirical scaling of the addition of Cr (Ti) and a negative (positive) pressure. The behavior of hysteresis shows that The metal-insulator transition is the first order.

where the first term denotes the kinetic energy and the second one the Coulomb repulsion between the electrons at the same site. This model is too difficult to treat except for the trivial limit because it includes the competition between itinerancy and localization of electrons. In the weak coupling limit $U/W \ll 1$, this model reproduces the metallic behavior described by the band theory. Here, W denotes the band-width. On the other hand, in the strong coupling limit $U/W \gg 1$, the electrons are localized because of refusal to energy loss by the strong Coulomb repulsion and the system becomes Mott insulating state. In this regime, the original band is split into the two sub-bands with energy difference $\Delta \sim U$, which are called Hubbard bands. However, the proper description of the Mott transition is quite difficult and there have remained many problems.

The Mott transition is typically found in V_2O_3, $NiS_{2-x}Se_x$ and so forth [4]. We take vanadium sesquioxide V_2O_3 for instance and overview Mott physics. When applying pressure on V_2O_3, the band-width W decreases. Doping with Cr (Ti) also increases (decreases) the band-width because of decrease (increase) in internal pressure. The phase diagram shown in Fig. 1.1 was obtained by experiments on V_2O_3 using temperature and pressure as variables. This phase diagram has three well-defined regions; metal, paramagnetic and antiferromagnetic insulator. In Fig. 1.1, the transition from paramagnetic metal to antiferromagnetic insulator accompanied by translational symmetry breaking is seen at temperature $T < 200$K. Note that also at high temperature, $200\text{K} < T < 400\text{K}$, the metal to insulator transition in the paramagnetic phase is observed. This indicates that the metal-insulator transition is not explaind only by the magnetic ordering. We can see hysteresis behavior in both the transitions, therefore the transitions are the first order. One thus finds that the metal-insulator transition is induced by varying the interaction strength U/W and temperature T.

In addition, it is pointed out that the values of specific heat coefficient and Pauli susceptibility measured for the metallic state near the transition point are extremely larger than those predicted by the band theory [6]. It implies enhancement of electron mass in the proximity of the Mott transition. Formation of Hubbard bands and mass enhancement are explained in the unified framework by applying the dynamical mean field theory to the Hubbard model in the infinite spatial dimensions [7]. In fact, the phase diagram close to the experimental results shown in Fig. 1.1 is obtained by the dynamical mean field theory [7]. The dynamical mean field theory has strongly promoted research of the Mott transition. Additionally, much effort has been recently devoted to describe realistic electronic structure by means of the combination of *ab initio* calculation and the dynamical mean field theory [8–11]. We will give an explanation of the dynamical mean field theory in detail in Chap. 2.

1.2 Geometrical Frustration

Recently, many kinds of materials with geometrically frustrated lattice systems have been systematically made because of advances in the technology of material synthesis. Geometrical frustration means the situation that expected spin order state is inhibited due to geometry of lattice structure in some specific lattice systems such as triangular, kagomé and pyrochlore lattice systems.

As a simplest example of geometrically frustrated systems, we now con-

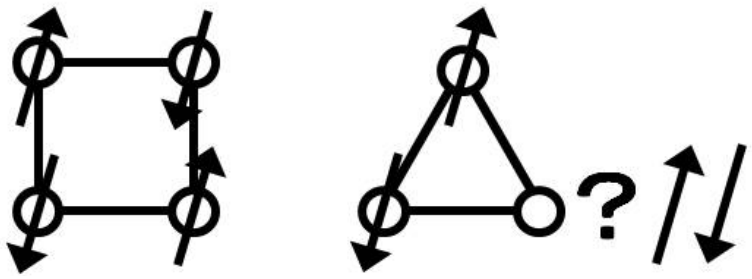

Figure 1.2: Sketch of geometrical frustration. Up and down arrows represent the degrees of freedom of spins. In the left panel, there is no geometrical frustration because spin configuration is specified uniquely. On the other hand, the right panel shows that no configuration can be realized that all the three interactions between neighboring spins are simultaneously minimal on the single-triangular lattice.

sider the configuration of spins with two degrees of freedom on each site in the single-triangular lattice shown in Fig. 1.2. The single-square lattice system is also shown as a sample of unfrustrated systems for comparison. The degrees of freedom of spins are represented by up- and down-pointing arrows. Here, we assume that there are antiferromagnetic interactions between the neighboring spins. On the single-square lattice, the configuration that the four spins are antiparallel alternately is energetically stable as shown in the left panel in Fig. 1.2. On the other hand, it is impossible that all the three interactions between neighboring spins are simultaneously minimal on the single-triangular lattice as shown in the right panel in Fig. 1.2. As seen above, the antiferromagnetic ordered state cannot be realized due to geometry of the lattice in frustrated systems.

One of the interesting phase expected in frustrated systems is the spin liquid state, which was theoretically suggested by P. W. Anderson in 1973 [12]. The spin liquid has no magnetic order unlike antiferromagnet. In such systems at very low temperature, novel properties are expected to emerge due to quantum effects. The competition between charge degrees of freedom and geometrical frustration effects may also generate unprecedented physics.

A variety of materials with geometrical frustration have been discovered so far. For example, $ZnCu_3(OH)_6Cl_2$, which consists of Cu kagomé layers, shows spin liquid behavior at low temperatures [13–15] and LiV_2O_4, where V ions form the pyrochlore lattice structure, shows heavy Fermi liquid behaviors characteristic of those of the heaviest-mass f-electron systems [16–19].

Here, we consider the family of κ-(BEDT-TTF)$_2X$ [20–25] and refer to

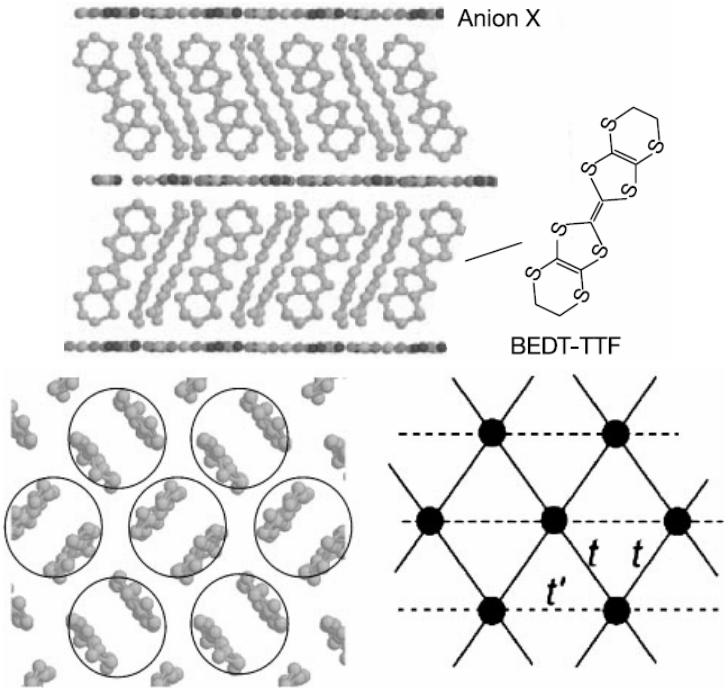

Figure 1.3: Crystal structure of κ-(BEDT-TTF)$_2X$ [22]. The top and left lower figures are vertical and side sectional (in a BEDT-TTF mlecule plane) views of κ-(BEDT-TTF)$_2X$ respectively. We can see that BEDT-TTF molecule and anion X layers are stacked alternately (top) and BEDT-TTF molecules are dimerized (left lower). The lower right figure is the sketch of the crystal structure of κ-(BEDT-TTF)$_2X$ where a site corresponds to a dimer of BEDT-TTF molecules and the dimers form an anisotropic triangular lattice.

physical properties of the triangular lattice systems. The organic materials κ-(BEDT-TTF)$_2X$ are based on BEDT-TTF molecules, where BEDT-TTF is the abbreviation of bis(ethylenedithio)tetrathiafulvalene, and have the two-dimensional triangular lattice systems. Here, X denotes a monovalent anion for example Cu[N(CN)$_2$]Cl, Cu[N(CN)$_2$]Br, CuN(NCS)$_2$, Cu$_2$(CN)$_3$, etc. The BEDT-TTF molecule has a near planer shape and BEDT-TTF molecule and anion X layers are stacked alternately as shown in the top panel in Fig. 1.3. In this system, the anion X sheets play the role of insulating layer and there is one hole per dimer. Thus, this system can be regarded as the two-dimensional anisotropic triangular lattice system at half filling as shown in the lower panels in Fig 1.3. In the lower right panel, t and t' denote the transfer integrals and the ratio t'/t determines the strength of anisotropy. In particular, this

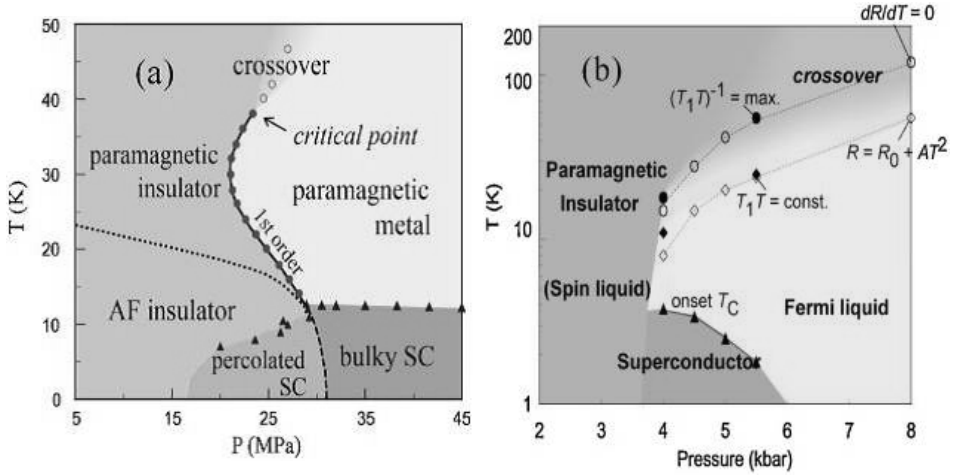

Figure 1.4: Phase diagrams on pressure-temperature plane of κ-(BEDT-TTF)$_2$Cu[N(CN)$_2$]Cl ($t'/t = 0.75$) (left) and of κ-(BEDT-TTF)$_2$Cu$_2$(CN)$_3$ ($t'/t = 1.06$) (right) [24]. Antiferromagnetic order is absent at very low temperatures in κ-(BEDT-TTF)$_2$Cu$_2$(CN)$_3$, which is remarkablly different from κ-(BEDT-TTF)$_2$Cu[N(CN)$_2$]Cl. Additionally, we can see the reentrant behavior in the Mott transition in κ-(BEDT-TTF)$_2$Cu[N(CN)$_2$]Cl.

lattice corresponds to square lattice at $t'/t = 0$ and isotropic triangular lattice at $t'/t = 1$, respectively. The replacement of anions or deuteration of BEDT-TTF molecules are powerful ways to apply chemical pressure or to change strength of anisotropy to these materials. Experimental phase diagrams of κ-(BEDT-TTF)$_2$Cu[N(CN)$_2$]Cl and of κ-(BEDT-TTF)$_2$Cu$_2$(CN)$_3$ are shown on the temperature-pressure plane in Fig. 1.4. The strength of anisotropy $t'/t = 0.75$ for κ-(BEDT-TTF)$_2$Cu[N(CN)$_2$]Cl corresponds to intermediate frustration. On the other hand, κ-(BEDT-TTF)$_2$Cu$_2$(CN)$_3$ has almost isotropic triangular lattice structure due to $t'/t = 1.06$. Both of them show the Mott transition by applying pressure, which corresponds to decreasing U. Antiferromagnetic insulating state is stable in κ-(BEDT-TTF)$_2$Cu[N(CN)$_2$]Cl at low temperatures. In contrast, long-range magnetic order is absent in κ-(BEDT-TTF)$_2$Cu$_2$(CN)$_3$ at least down to 32mK, which is 4 orders of magnitude lower than the exchange interaction $J \sim 250$K. The result strongly suggests the realization of a quantum spin liquid in κ-(BEDT-TTF)$_2$Cu$_2$(CN)$_3$ due to strong geometrical frustration [24, 26]. It is interesting that the Mott transition line of κ-(BEDT-TTF)$_2$Cu[N(CN)$_2$]Cl curves around 30K under pressure, which is called the reentrant Mott transition. It is suggested that competition of moderate geometrical frustration and antiferromagnetic correlation leads to the reentrant transition [25, 27].

1.3 Honeycomb Lattice

The studies of strongly correlated electron systems on the honeycomb lattice have been strongly promoted by first isolation of graphene, a single atomic layer of graphite in 2004 [28]. The exotic properties of graphene, such as Dirac fermion behavior at low energies and anomalous integer quantum Hall effect, were theoretically predicted several decades ago [29–32]. The exotic properties stem from the honeycomb lattice structure, *i.e.*, a hexagonal tiling of carbon atoms, and they are entirely different from those of conventional two-dimensional systems. In addition, boron nitride [33], magnesium diboride superconductor [34], etc. have been known as honeycomb lattice systems.

The unique feature of the honeycomb lattice appears the tight-binding spectrum shown in Fig. 1.5. As shown in the left panel in Fig. 1.5, There are the two bands and they contact each other only at the so-called Dirac points. This results in the pseudogap at the Fermi level as seen in the right panel in Fig. 1.5. This gapless state is called *semi-metal* or zero-gap semiconductor because of the existence of the pseudogap. Further, the density of states in vicinity of the Fermi level is known to be linear. This linearity of the spectrum around the Dirac points gives rise to an effective low energy description of the electrons that mimics the spectrum of massless Dirac particles, namely the quantum mechanical description of the relativistic electrons is given [35].

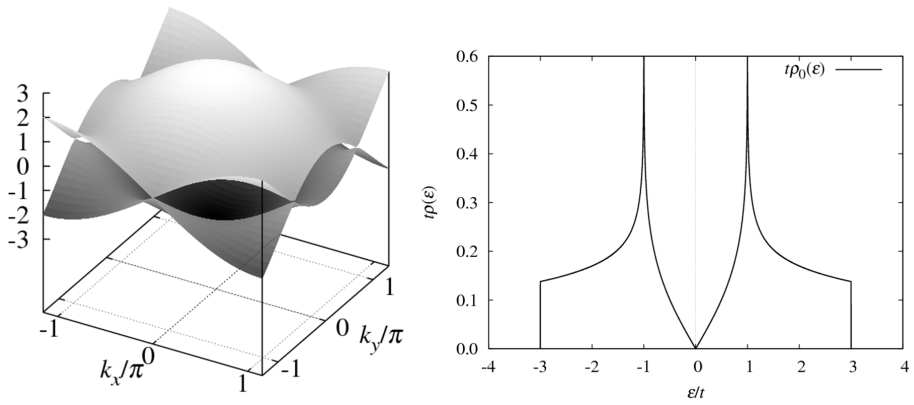

Figure 1.5: Tight-binding spectrum of honeycomb lattice. The band structure (left) and the density of states (right) are shown.

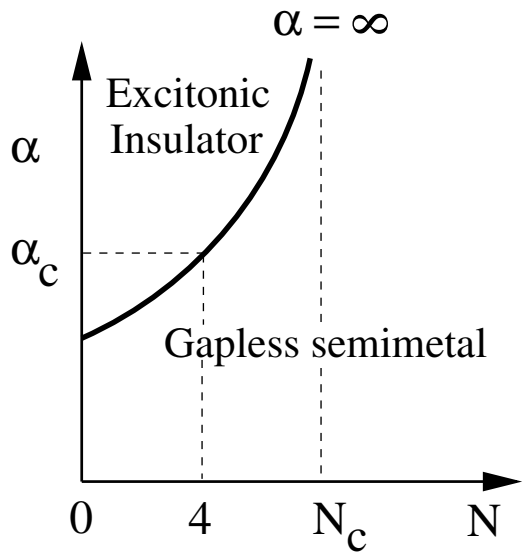

Figure 1.6: Schematic phase diagram in the α-N plane [36]. The critical parameters $\alpha_c \sim 1$ and $N_c \sim 7$ to 9. Here, α and N denote a coupling constant and the number of fermion flavors, respectively.

We overview the properties of honeycomb lattice taking graphene for instance. The quasi-particle properties of graphene are modified by the presence of electron-electron interactions [36]. It is possible that the metal-insulator transition happens by long-range Coulomb interaction because, for example, spontaneous gap generation due to an excitonic pairing mechanism. This excitonic insulating state have been intensively studied by means of the random phase approximation [37–41] and by the Monte Carlo method of simulating lattice field theories [42–45]. According to the random phase approximation, a transition to a gapped state is found above a critical coupling $\alpha_c \sim 1$ for the number of fermion flavors $N = 4$ [37, 39]. Here, a coupling α is defined as the ratio of Coulomb to kinetic energy, namely $\alpha = e^2/(\epsilon_0 \hbar v_{\rm F})$, where e, ϵ_0 and $v_{\rm F}$ are the electron charge, the dielectric constant of the medium and the Fermi velocity, respectively. It has also been found that the gap is non-zero only below the critical number of fermion flavors $N_c \sim 7$ at strong coupling limit $\alpha \to \infty$ [39, 41]. These results are consistent with those obtained by the Monte Carlo calculation: $N_c \sim 9.6, \alpha \gg 1$ [45] and $\alpha_c = 1.1, N = 4$ [43]. Those results are shown in Fig. 1.6, which describes the excitonic insulating phase emerges in strong coupling and the small number of fermion flavors. For graphene deposited on SiO the value of $\alpha_{\rm SiO_2} \sim 0.79$ and is therefore not enough to generate a gap. Further, it is suggested that

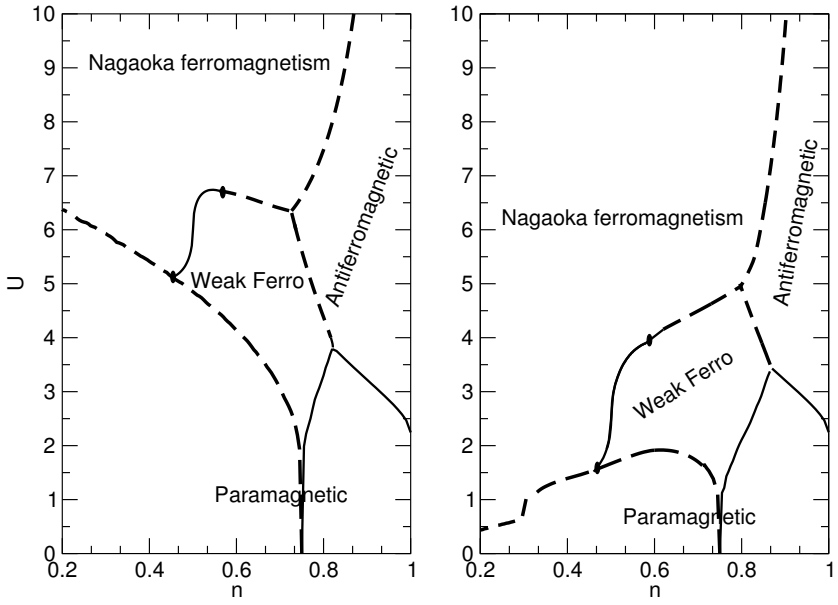

Figure 1.7: Ground state phase diagram of the Hubbard model in the n-U plane [53]. The next-nearest hopping integral $t'/t = 0$ (left) and $t'/t = -0.2$ (right). Here, n denotes particle density and U is interaction strength. In both cases, dashed and solid lines represent first and second order transitions, respectively.

some factors change the excitonic instability. The finite doping destroys the gap very quickly [41]. The magnetic field perpendicular to the graphene opens an excitonic gap due to the formation of Landau levels [38,46,47], and an in-plane magnetic field leads to the formation of electron- and holelike Fermi surfaces which stabilizes a gapped excitonic state [48].

There have also been a lot of studies on mechanism of mass gap generation, for example the sublattice inversion symmetry breaking due to applying a staggered magnetic field [49]. Another mechanism is due to spin orbit coupling which induces a quantum spin Hall state. When the mirror symmetry is broken either by a substrate or external electric field, a Rashba term is added to Hamiltonian. As a result of additional Rashba term, the mass gap is induced [50]. Kekulé lattice distortions, which break the translational symmetry of the lattice, also lead to the opening gaps in graphene [51]. The possibility of Nagaoka ferromagnetism in doped systems is also predicted by means of variational [52] and mean field calculations [53]. The magnetic instability in the Hubbard model obtained by the mean field calculation is shown in Fig. 1.7. We can see the two types of ferromagnetic ground states:

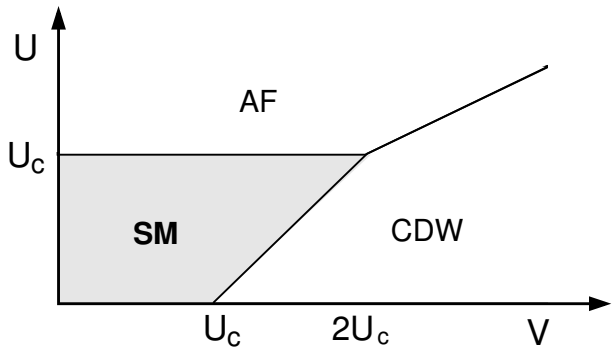

Figure 1.8: Phase diagram of the extended Hubbard model in the U-V plane obtained by the renormalization group analysis in large N expansion. [36, 56]. Here, U and V denote on-site and the nearest neighbor site Coulomb repulsion, respectively, and U_c stands for the critical coupling. In this phase diagram, three regions appear: semi-metal (SM), antiferromagnetic phase (AF) and charge density wave state (CDW).

the Nagaoka ground state with maximally polarized spin ($m_{\rm F} = n$), and a weak ferromagnetic state with $m_{\rm F} < n$, where $m_{\rm F}$ and n denote magnetization and particle density, respectively. Further, a negative t' stabilizes ferromagnetic states as shown in the right panel in Fig. 1.7. At $n = 0.75$, the instability line towards the ferromagnetic phase shows a dip, which is due to the logarithmic van Hove singularity at $n = 0.75$ as shown in the right panel in Fig. 1.5. It is noteworthy that the validity of Hubbard model, which does not include long-range Coulomb interactions, for investigating graphene, could be justified either in the presence of strong screening effects from substrates or by accounting for dynamical screening effects from graphene itself [54]. As shown in Fig. 1.7, at half filling, the antiferromagnetic state is favored by the on-site repulsion and competes with the long-range part of the Coulomb field. The long-range Coulomb interaction can favor charge density wave instability [40–43, 47, 55]. The effect of the long-range Coulomb interaction is investigated by the renormalization group analysis of the extended Hubbard model [56]. The results of semi-metal insulator transition is shown in Fig. 1.8. When the nearest neighbor site Coulomb interaction V is enough large, the charge density wave state is stable. Further, the possibility of spin density wave instability at half filling and of d-wave super conductivitng state in doped regime are suggested by functional renormalization group calculation for the $t - J$ model on honeycomb lattice with on-site and nearest neighbor repulsion [57].

Let us focus on the Mott transition and antiferromagnetic instability in the honeycomb lattice Hubbard model only with the nearest-neighbor hopping integral. It is predicted that the metal-insulator transition happens at finite Hubbard $U_{\rm AF}/t = 2.23$ by means of the static mean field theory, which is different from conventional two-dimensional bipartite systems, where the insulating state is stable for any non-zero U. Here, t denotes the nearest-neighbor hopping integral. That is because of the existence of the pseudogap at the Fermi level. Recently, there have been a lot of theoretical studies on the electronic properties in the Hubbard model on the honeycomb systems with taking into account quantum fluctuations. S. Sorella and E. Tosatti point out that the transition between semi-metallic and antiferromagnetic insulating phases occurs at $U_{\rm AF}/t = 4.5 \pm 0.5$ by quantum Monte Carlo simulations for a finite system [58]. T. Paiva *et al.* obtained similar results by means of quantum Monte Carlo and series expansion techniques [59] as well as L. M. Martelo *et al.* [60] and N. Furukawa [61] by using a variational method. Those critical values acquired by them are much larger than that by means of the static mean field theory, which indicates the importance of quantum fluctuations. In the framework of the cellular dynamical mean field theory under the assumption that no long-range order is present, the Mott transition is found at $U_{\rm MI}/t \sim 3.3$ [62, 63], which is close to the above-mentioned critical value $U_{\rm AF}$. The U(1) gauge theory suggests the existence of nonmagnetic insulating phase in the narrow range $1.68 < U/t < 1.74$ [64], and similar results have been obtained by the SU(2) slave-rotor theory [65, 66], On the other hand, G. Y. Sun and S. P. Kou report that nonmagnetic insulator appears for $2.88 < U/t < 2.93$ and antiferromagnetic insulator for $2.23 < U/t < 2.88$ and $U/t > 2.93$ calculated by using O(3) nonlinear σ model for the Hubbard model [67]. These slave-fermion theories sometimes give an artifactitious phase transition because of expanding Hilbert space. From this viewpoint, the difference of those results may stem from above artifact. Recently, Z. Y. Meng *et al.* have found that the two phase transitions as increasing U, the first from semi-metal to spin liquid, the second to an antiferromagnetic insulator at $U_{\rm MI}/t = 3.5$ and $U_{\rm AF}/t = 4.3$ respectively, by projective determinantal quantum Monte Carlo simulations [68]. This is of significance in treating semi-metal, nonmagnetic and antiferromagnetic insulator in a unified framework at zero temperature, however, the results are obtained by calculations for finite systems and with a large statistical error.

Meanwhile, the single-site dynamical mean field theory gives the critical values $U_{\rm MI}/t \sim 13.3$ for the iterative perturbation theory [69] and $U_{\rm MI}/t \sim 10$ by combining with the exact diagonal method as an impurity solver [70], which are much larger than those by other methods. This fact means that non-local correlations play quite an important role.

In spite of many researches have been done for some decades, a lot of questions remain unclear in the Hubbard model on the honeycomb lattice, for example how antiferromagnetic correlations affect the phase transitions and if nonmagnetic insulating phase is stable in strong correlated electron systems on the honeycomb lattice. It can be the first sample of the nonmagnetic insulating state without geometrical frustration.

1.4 Organization of the Thesis

In the present thesis, we address the Mott transition on the square and honeycomb lattice systems and present the systematic perspective on the Mott transition influenced by geometrical frustrations or quantum fluctuations.

Organization of this thesis is as follows; the dynamical mean field theory and its cluster expansions are reviewed in Chap. 2. These theories are powerful methods to study strongly correlated electron systems. In Chap. 3, we propose the new methods derived by extension to the cluster version of the two-site dynamical mean field theory, which enable us to study the spatial fluctuation effects systematically. By means of these methods obtained in Chap. 3, we investigate the square Hubbard model with/without geometrical frustration and describe the competition between itinerancy of electrons and antiferromagnetic short-range order in Chap. 4. Our method is also applied to the Hubbard model on the honeycomb lattice and the presence of nonmagnetic insulating state is considered in Chap. 5.

Chapter 2

Dynamical Mean Field Theory and Cluster DMFT

The mean field theory is the most convenient method which describes various physics such as superconductivity, magnetism, etc. In the system with strongly correlated electrons, however, effects of dynamical fluctuations which cannot be incorporated by the *static* mean field theory, that is, the *electron correlation effects* are very important. It is one of the most important problem to establish a theoretical method which properly treats these many-body effects due to the electron correlations.

As a theoretical method to study the electron correlation effects, for one-dimensional systems, the Bethe ansatz solution and/or conformal field theory is applicable to specific systems, which gives an exact solution of specific physical properties. The density matrix renormalization group, which is the powerful numerical calculation, can be also applied to the one-dimensional systems. On the other hand, for the systems with more than two spatial dimensions, the conclusive methods has not yet been established so far. As a weak coupling theory, the perturbative renormalization group or fluctuation exchange approximation [71] are known as a good method. The slave-boson/fermion mean field theory or variational Monte Carlo method might be able to be applied to the strong coupling regime. As a numerical simulation for the finite cluster, the Quantum Monte Carlo method is popular [72–74], and the path integral renormalization group method has recently developed [26, 75–78].

Against this background, the dynamical mean field theory has recently been developed. This method starts from the limit of the infinite spatial dimensions and correctly incorporates local electron correlations. The dynamical mean field theory has, at first, been proposed as an exact theory in the spatial dimension $d \to \infty$ by Metzner and Vollhardt [79]. Now, it

has been regarded as a powerful theoretical framework to study the strongly correlated electron systems and applied to various systems [7].

2.1 Dynamical Mean Field Theory

In the dynamical mean field theory, the lattice models such as Hubbard model and periodic Anderson model, which describe the strongly correlated electron systems, are mapped onto the *effective* quantum impurity model. In the effective impurity model, the *impurity* is coupled to the dynamical or time-dependently fluctuating field. This is the different point of the *dynamical* mean field theory from the *static* mean field theory.

Here, we consider the Hubbard model,

$$H = \sum_{i,j,\sigma} t_{ij} c^{\dagger}_{i\sigma} c_{j\sigma} - \mu \sum_{i,\sigma} c^{\dagger}_{i\sigma} c_{i\sigma} + U \sum_{i} n_{i\uparrow} n_{i\downarrow}, \tag{2.1}$$

and briefly explain the dynamical mean field theory. In (2.1), t_{ij} denotes the hopping integral from ith to jth site, μ is the chemical potential, and U denotes the Hubbard interaction.

At first, we introduce a brief overview of the dynamical mean field theory. Figure 2.1. shows its basic concept. The path integral representation [80] is convenient to derive the effective action in the dynamical mean field theory. The partition function for the Hamiltonian (2.1) is described by the path

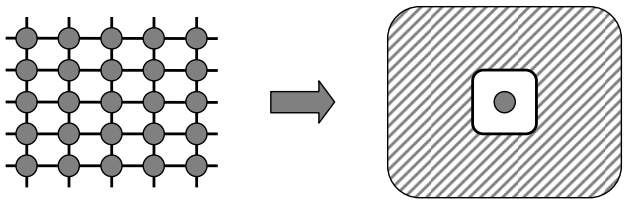

Figure 2.1: In the dynamical mean field theory, an arbitrary site in the lattice model (left) is chosen as an *impurity*. The lattice model is then mapped onto the effective impurity model (right) with the dynamical effective medium which incorporates the contribution from the surrounding other sites to the *impurity*.

integral representation as

$$Z = \int \prod_{i,\sigma} \mathcal{D}c^{\dagger}_{i\sigma} \mathcal{D}c_{i\sigma} e^{-S} \tag{2.2}$$

$$S = \int_0^{\beta} d\tau \left\{ \sum_{i,j,\sigma} c^{\dagger}_{i\sigma}(\tau) \left[\left(\frac{\partial}{\partial \tau} - \mu \right) \delta_{ij} + t_{ij} \right] c_{j\sigma}(\tau) + U \sum_i n_{i\uparrow}(\tau) n_{i\downarrow}(\tau) \right\}. \tag{2.3}$$

Here, S is the action and, c and $c^{\dagger}$ are Grassmann numbers. The mapping shown in Fig. 2.1 corresponds to (i) choice of an arbitrary site (referred to as site 0) as an *impurity* and (ii) integrating out all the degrees of freedom of the sites other than the *impurity* in the path integral. Of course, the path integral cannot be carried out exactly. If the path integral approximately is carried out, it is expected that the effective action $S_{\rm eff}$ for the site 0 would be

$$S_{\rm eff} = -\int_0^{\beta} d\tau_1 d\tau_2 \sum_{\sigma} c^{\dagger}_{0\sigma}(\tau_1) \mathcal{G}^{-1}_{\sigma}(\tau_1 - \tau_2) c_{0\sigma}(\tau_2) + U \int_0^{\beta} d\tau n_{0\uparrow}(\tau) n_{0\downarrow}(\tau), \tag{2.4}$$

where, $\mathcal{G}_{\sigma}(\tau)$ is the unperturbed Green's function which is defined as, $\mathcal{G}_{\sigma}(\tau) = -\langle T_{\tau} c_{0\sigma}(\tau) c^{\dagger}_{0\sigma}(0) \rangle_0$, in the effective action $S_{\rm eff}$, which describes the time-dependent effective medium. Here, T_{τ} is the time ordering operator and $\langle \cdots \rangle_0$ denotes the statistical average in $S_{\rm eff}$ without the interaction term. The effective action (2.4) corresponds to the right panel in Fig. 2.1. If we impose that the full Green's function G_{σ} satisfy the Dyson equation,

$$G_{\sigma} = \mathcal{G}_{\sigma} + \mathcal{G}_{\sigma} \Sigma_{\sigma} G_{\sigma}, \tag{2.5}$$

we obtain the relation among G_{σ}, $\mathcal{G}_{\sigma}$ and Σ_{σ}. Here, G_{σ} is defined as $G_{\sigma}(\tau) = -\langle T_{\tau} c_{0\sigma}(\tau) c^{\dagger}_{0\sigma}(0) \rangle$, by using the statistical average in $S_{\rm eff}$. Therefore, when the effective medium $\mathcal{G}_{\sigma}$ is given, we can obtain the self-energy Σ_{σ} and Green's function G_{σ} by solving the effective action (2.4).

On the other hand, the Green's function G_{σ} must be consistent with the local Green's function in the original lattice model (2.1), because G_{σ} is the local Green's function for the electron at site 0. The local Green's function in the Hamiltonian (2.1) is generally written as

$$G_{\sigma}(\omega) = \frac{1}{N} \sum_{\mathbf{k}} \frac{1}{\omega - \varepsilon_{\mathbf{k}} + \mu - \Sigma_{\mathbf{k}\sigma}(\omega)}. \tag{2.6}$$

Here, $\varepsilon_{\mathbf{k}}$ is the dispersion,

$$\varepsilon_{\mathbf{k}} = \frac{1}{N}\sum_{i,j} e^{i\mathbf{k}\cdot(\mathbf{r}_i-\mathbf{r}_j)} t_{ij}, \tag{2.7}$$

and $\Sigma_{\mathbf{k}\sigma}(\omega)$ is the self-energy for the electron with the wave vector $\mathbf{k}$ and spin σ. In the dynamical mean field theory, only the local self-energy Σ_σ is obtained due to the above local approximation. If we neglect the $\mathbf{k}$-dependence of the self-energy, we obtain the Green's function,

$$G_\sigma(\omega) = \frac{1}{N}\sum_{\mathbf{k}} \frac{1}{\omega - \varepsilon_{\mathbf{k}} + \mu - \Sigma_\sigma(\omega)}, \tag{2.8}$$

in terms of the local self-energy Σ_σ. By using Eqs. (2.5) and (2.8), the Green's function for the effective medium $\mathcal{G}_\sigma$ is determined by

$$\mathcal{G}_\sigma^{-1}(\omega) = \left[\frac{1}{N}\sum_{\mathbf{k}} \frac{1}{\omega - \varepsilon_{\mathbf{k}} + \mu - \Sigma_\sigma(\omega)}\right]^{-1} + \Sigma_\sigma(\omega). \tag{2.9}$$

If $\mathcal{G}_\sigma$ given, we can solve the effective action (2.4) and calculate the self-energy Σ_σ. For given Σ_σ, we can calculate $\mathcal{G}_\sigma$ using Eq. (2.9). Therefore, these equations are the self-consistent equations. This is an overview of the dynamical mean field theory.

In the above discussions, however, we used some assumptions to derive the self-consistent equation (2.9). So, we next proceed with the microscopic derivation of the dynamical mean field theory. The calculations below are important for systematic extensions of the dynamical mean field theory. For microscopic derivation, we first divide the action for the Hubbard model (2.3) into three parts,

$$S = S_0 + \Delta S + S^{(0)}, \tag{2.10}$$

$$S_0 = \int_0^\beta d\tau \left\{ \sum_\sigma c_{0\sigma}^\dagger(\tau)\left(\frac{\partial}{\partial\tau} - \mu\right) c_{0\sigma}(\tau) + U n_{0\uparrow}(\tau) n_{0\downarrow}(\tau) \right\}, \tag{2.11}$$

$$\Delta S = \int_0^\beta d\tau \left\{ \sum_{i,\sigma} \left[t_{i0} c_{i\sigma}^\dagger(\tau) c_{0\sigma}(\tau) + t_{0i} c_{0\sigma}^\dagger(\tau) c_{i\sigma}(\tau) \right] \right\}, \tag{2.12}$$

$$S^{(0)} = \int_0^\beta d\tau \left\{ \sum_{i,j\neq 0,\sigma} c_{i\sigma}^\dagger(\tau) \left[\left(\frac{\partial}{\partial\tau} - \mu\right)\delta_{ij} + t_{ij} \right] c_{j\sigma}(\tau) + \sum_{i\neq 0} U n_{i\uparrow}(\tau) n_{i\downarrow}(\tau) \right\}. \tag{2.13}$$

Here, S_0 is the action for the site 0 chosen as an *impurity*, ΔS is the coupling between the site 0 and other sites, and $S^{(0)}$ is for sites except the site 0. The partition function Z is rewritten by the three actions,

$$\begin{aligned} Z &= \int \mathcal{D}c_{0\sigma}^{\dagger}\mathcal{D}c_{0\sigma}e^{-S_0}\int\prod_{i\neq 0,\sigma}\mathcal{D}c_{i\sigma}^{\dagger}\mathcal{D}c_{i\sigma}e^{-S^{(0)}}e^{-\Delta S} \\ &= Z^{(0)}\int \mathcal{D}c_{0\sigma}^{\dagger}\mathcal{D}c_{0\sigma}e^{-S_0}\langle e^{-\Delta S}\rangle^{(0)}. \end{aligned} \tag{2.14}$$

Here, $\langle\cdots\rangle^{(0)}$ represents the statistical average for the action $S^{(0)}$, which is referred to as the *cavity average* below,

$$\langle\cdots\rangle^{(0)} = \frac{1}{Z^{(0)}}\int\prod_{i\neq 0,\sigma}\mathcal{D}c_{i\sigma}^{\dagger}\mathcal{D}c_{i\sigma}[\cdots]e^{-S^{(0)}}, \tag{2.15}$$

$$Z^{(0)} = \int\prod_{i\neq 0,\sigma}\mathcal{D}c_{i\sigma}^{\dagger}\mathcal{D}c_{i\sigma}e^{-S^{(0)}}. \tag{2.16}$$

Using the above expressions, we carry out the path integral for degrees of freedom of all the sites except the site 0. In Eq. (2.14), the action for the coupling between the site 0 and the other sites, $\langle e^{-\Delta S}\rangle^{(0)}$ is expanded in powers of ΔS,

$$\left\langle e^{-\Delta S}\right\rangle^{(0)} = 1 - \langle\Delta S\rangle^{(0)} + \frac{1}{2}\left\langle(\Delta S)^2\right\rangle^{(0)} - + \cdots. \tag{2.17}$$

In the first order term of the expansion, $\langle c_{i\sigma}^{\dagger}(\tau)\rangle^{(0)}c_{0\sigma}(\tau)$, $c_{0\sigma}^{\dagger}(\tau)\langle c_{i\sigma}(\tau)\rangle^{(0)}$, etc. appear and these terms are not allowed to be by the conservation rule of the particle number. Also by considering the conservation rule, the second order term is explicitly written down as

$$\begin{aligned} \frac{1}{2}\left\langle(\Delta S)^2\right\rangle^{(0)} = \int_0^{\beta} d\tau_1 d\tau_2 \sum_{\sigma} c_{0\sigma}^{\dagger}(\tau_1) \\ \left[\sum_{ij} t_{i0}t_{0j}\left\langle T_{\tau}c_{i\sigma}(\tau_1)c_{j\sigma}^{\dagger}(\tau_2)\right\rangle^{(0)}\right] c_{0\sigma}(\tau_2). \end{aligned} \tag{2.18}$$

For higher order terms, the approximation which is exact in the limit of the infinite spatial dimensions, $d\to\infty$ is applied. In order to keep the band width invariant with increasing the spatial dimension, the hopping integral t_{ij} is scaled as $t_{ij}\to t_{ij}/\sqrt{d}$. Under the scaling, the two-point Green's function in Eq. (2.18), $\left\langle T_{\tau}c_{i\sigma}(\tau_1)c_{j\sigma}^{\dagger}(\tau_2)\right\rangle^{(0)}$ is of the order of $1/d$, because two hopping

processes are needed for an electron to move from ith to jth site which are the nearest neighbor sites of the site 0. On the other hand, in Eq. (2.18), the hopping integral t_{ij}^2 and the summation $\sum_{i,j}$ give contributions of order $1/d$ and d^2, respectively. Therefore, the order of the second order term is $1/d \times 1/d \times d^2 = 1$, which gives a non-negligible contribution in the limit of $d \to \infty$. In the nth order in the expansion, less than n-point Green's function appears. As above mentioned, at least two hopping processes appear in electron transfer between two sites except the site 0. In the n-point Green's function, the electron transfers $n-1$ times appear, which gives contribution of the order of $(1/d)^{n-1}$. In this Green's function, t_{ij}^n and n summations also appears. Therefore, n-point Green's function is of the order of $(1/d)^{n-1} \times (1/\sqrt{d})^n \times d^n = (1/\sqrt{d})^{n-2}$. From the above discussions, more than three-point Green's function vanishes in the limit of $d \to \infty$. In higher order terms, only the terms which are divided into the product of the two-point Green's function survives. Therefore, $\left\langle e^{-\Delta S} \right\rangle^{(0)}$ is calculated in the limit of the infinite spatial dimensions, $d \to \infty$, as,

$$\left\langle e^{-\Delta S} \right\rangle^{(0)} \to \exp\left\{ - \int_0^\beta d\tau_1 d\tau_2 \right. \\ \left. \sum_\sigma c_{0\sigma}^\dagger(\tau_1) \left[\sum_{ij} t_{i0} t_{0j} G_{ij}^{(0)}(\tau_1 - \tau_2) \right] c_{0\sigma}(\tau_2) \right\}, \tag{2.19}$$

$$G_{ij\sigma}^{(0)}(\tau_1 - \tau_2) \equiv - \left\langle T_\tau c_{i\sigma}(\tau_1) c_{j\sigma}^\dagger(\tau_2) \right\rangle^{(0)}. \tag{2.20}$$

Here, $G_{ij\sigma}^{(0)}$ is called the *cavity Green's function*, which describes the influence of the other sites to the electron at site 0. Substituting the above expression into Eq. (2.14), we obtain the effective action,

$$\begin{aligned} S_{\text{eff}} &= \int_0^\beta d\tau \left\{ \sum_\sigma c_{0\sigma}^\dagger(\tau) \left(\frac{\partial}{\partial \tau} - \mu \right) c_{0\sigma}(\tau) + U n_{0\uparrow}(\tau) n_{0\downarrow}(\tau) \right\} \\ &\quad + \int_0^\beta d\tau_1 d\tau_2 \sum_\sigma c_{0\sigma}^\dagger(\tau_1) \left[\sum_{ij} t_{i0} t_{0j} G_{ij\sigma}^{(0)}(\tau_1 - \tau_2) \right] c_{0\sigma}(\tau_2) \\ &= - \int_0^\beta d\tau_1 d\tau_2 \sum_\sigma c_{0\sigma}^\dagger(\tau_1) \mathcal{G}_\sigma^{-1}(\tau_1 - \tau_2) c_{0\sigma}(\tau_2) \\ &\quad + U \int_0^\beta d\tau n_{0\uparrow}(\tau) n_{0\downarrow}(\tau). \end{aligned} \tag{2.21}$$

Here, $\mathcal{G}_\sigma$ is the Green's function describing the effective medium,

$$\mathcal{G}_\sigma^{-1}(\omega) = \omega + \mu - \sum_{ij} t_{i0} t_{0j} G^{(0)}_{ij\sigma}(\omega). \tag{2.22}$$

The expression (2.21) is consistent with Eq. (2.4), and we confirm that the Hubbard model is mapped onto the effective impurity model (2.4) in the infinite spatial dimensions, $d \to \infty$.

In the above discussions, we used the *action* representation. The *Hamiltonian* representation is also useful. To move to the Hamiltonian formula, we should only prepare the effective Hamiltonian which corresponds to the effective action (2.21). The Anderson impurity Hamiltonian,

$$H = \sum_{l,\sigma} \varepsilon_l a^\dagger_{l\sigma} a_{l\sigma} - \mu \sum_\sigma c^\dagger_{0\sigma} c_{0\sigma} + U n_{0\uparrow} n_{0\downarrow} + \sum_{l,\sigma} \left(V_l a^\dagger_{l\sigma} c_\sigma + \text{H.c.} \right), \tag{2.23}$$

is one of the typical Hamiltonian which leads to the action (2.21). This Hamiltonian is well known as the model describing the Kondo effect. Here, $a^\dagger_{l\sigma}$ ($a_{l\sigma}$) creates (annihilates) electrons with the effective bath degrees of freedom l and spin σ. Note that the infinite bath sites are needed to reproduce the effective action (2.21). The bath electrons have the dispersion ε_l and they are coupled with the *impurity* by the hybridization V_l. By using the path integral representation, it is confirmed that the action for the Hamiltonian (2.23) is equivalent to the effective action (2.21). In the action, the Green's function describing the effective medium $\mathcal{G}_\sigma$ is written in terms of bath parameters ε_l and V_l as

$$\mathcal{G}_\sigma^{-1}(\omega) = \omega + \mu - \sum_l \frac{|V_l|^2}{\omega - \varepsilon_l}. \tag{2.24}$$

Comparing Eq. (2.24) with Eq. (2.22), we obtain,

$$\sum_{ij} t_{i0} t_{0j} G^{(0)}_{ij\sigma}(\omega) = \sum_l \frac{|V_l|^2}{\omega - \varepsilon_l} \equiv \Delta(\omega), \tag{2.25}$$

which is called the hybridization function.

We now turn to calculation of the hybridization function $\Delta(\omega)$. The cavity Green's function $G^{(0)}_{ij\sigma}$ in $\Delta(\omega)$ is written by the cavity average, which is the statistical average by degrees of freedom except for the site 0, so that it is difficult to directly calculate this quantity. Therefore, we use the relation between the cavity Green's function $G^{(0)}_{ij\sigma}$ and the lattice Green's function $G_{ij\sigma}$,

$$G^{(0)}_{ij\sigma} = G_{ij\sigma} - G_{i0\sigma} G^{-1}_{00\sigma} G_{0j\sigma}, \tag{2.26}$$

which is shown by using the expansion of the lattice Green's function in the hopping integral t_{ij} [81]. Substituting this equation into $\Delta(\omega)$ (2.25) and using the Fourier transformation, we obtain

$$\begin{aligned}\Delta(\omega) &= \sum_{ij} t_{i0}t_{0j}\left[G_{ij\sigma} - G_{i0\sigma}G_{00\sigma}^{-1}G_{0j\sigma}\right] \\ &= \frac{1}{N}\sum_{\mathbf{k}} \varepsilon_{\mathbf{k}}^2 G_{\mathbf{k}\sigma} \\ &\quad - \left[\frac{1}{N}\sum_{\mathbf{k}} \varepsilon_{\mathbf{k}} G_{\mathbf{k}\sigma}\right] G_{00\sigma}^{-1} \left[\frac{1}{N}\sum_{\mathbf{k}} \varepsilon_{\mathbf{k}} G_{\mathbf{k}\sigma}\right]. \end{aligned} \tag{2.27}$$

Here, $G_{00\sigma}$ is the local Green's function in the lattice system and $G_{\mathbf{k}\sigma}$ is the lattice Green's function for the wave vector $\mathbf{k}$ and spin σ. By applying the approximation which neglects the $\mathbf{k}$-dependence of the self-energy to these Green's function, they are written as

$$G_{00\sigma}(\omega) = \frac{1}{N}\sum_{\mathbf{k}} G_{\mathbf{k}\sigma}(\omega), \tag{2.28}$$

$$G_{\mathbf{k}\sigma}(\omega) = \frac{1}{\zeta - \varepsilon_{\mathbf{k}}}, \tag{2.29}$$

$$\zeta \equiv \omega + \mu - \Sigma_\sigma(\omega) \tag{2.30}$$

Using the above equations, the summations over the wave vector in (2.27) are computed as

$$\frac{1}{N}\sum_{\mathbf{k}} \varepsilon_{\mathbf{k}}^2 G_{\mathbf{k}\sigma} = -\frac{1}{N}\sum_{\mathbf{k}} \varepsilon_{\mathbf{k}} - \zeta + \zeta^2 G_{00\sigma}, \tag{2.31}$$

$$\frac{1}{N}\sum_{\mathbf{k}} \varepsilon_{\mathbf{k}} G_{\mathbf{k}\sigma} = -1 + \zeta G_{00\sigma}. \tag{2.32}$$

Here, we use the fact, $\frac{1}{N}\sum_{\mathbf{k}} \varepsilon_{\mathbf{k}} = t_{00} = 0$. By using the above expressions, the hybridization is computed as

$$\Delta(\omega) = \zeta - G_{00\sigma}^{-1}. \tag{2.33}$$

Finally, we obtain the Green's function for the effective medium,

$$\mathcal{G}_\sigma^{-1}(\omega) = \left[\frac{1}{N}\sum_{\mathbf{k}} \frac{1}{\omega - \varepsilon_{\mathbf{k}} + \mu - \Sigma_\sigma(\omega)}\right]^{-1} + \Sigma_\sigma(\omega), \tag{2.34}$$

which is equivalent to Eq. (2.9). From the above discussions, we have microscopically derived the self-consistent equation in the dynamical mean field

theory. The dynamical mean field theory has been successfully applied to the single band Hubbard model [82–88], multi-band Hubbard model [89–97], periodic Anderson model [98–103], etc.

2.2 Cluster Dynamical Mean Field Theories

In the dynamical mean field theory explained in the previous section, the *local* quantum fluctuations are treated but *spatial* fluctuations are not incorporated. Therefore, it is difficult for the dynamical mean field theory to describe the high-T_c superconductivity, spin wave excitations, etc, where the *non-local* correlations are important. In order to study these phenomena, great effort for including the non-local fluctuations to the dynamical mean field theory has been made so far. The dynamical mean field theory is exact in the limit of infinite spatial dimensions, $d \to \infty$. So, a systematic $1/d$ expansion has been tried to recover the spatial fluctuations [104–108]. The higher order terms in the $1/d$ expansion, however, gives rise to violation of causality and the $1/d$ corrected dynamical mean field theory has not yet well established. Among them, the extended dynamical mean field theory is one of successful example in extensions of the dynamical mean field theory and it is the extended method which allows us to treat the inter-site interactions [109–111]. In this method, by explicitly introducing the inter-site interactions to the model Hamiltonian, the inter-site correlations are incorporated in the dynamical mean field theory. The dynamical vertex approximation perturbatively includes the non-local corrections to the self-energy obtained by the dynamical mean field theory [112]. In the dual fermion approach, the virtual fermions which undertakes the non-local correlation effects are introduced. The dynamical mean field type treatment is applied to the real fermions and the non-local correlations due to the virtual fermions are diagrammatically treated. This approach is applied to the one- and two-dimensional Hubbard model, and it is demonstrated that the results show a good agreement with those by the density matrix renormalization group and quantum Monte Carlo method [113–115].

These approaches are all extended methods based on the *single-site* dynamical mean field theory. It is also useful for the purpose of incorporating the spatial fluctuations that the effective *impurity* model in the dynamical mean field theory is extended to the effective *cluster* model. In this section, the cellular dynamical mean field theory [104, 116, 117] and the dynamical cluster approximation [118–121] which are the *cluster* extensions of the dynamical mean field theory will be briefly explained.

2.2.1 Cellular Dynamical Mean Field Theory

One of the methods which include the spatial correlations in the dynamical mean field theory is cluster-extended method, where the effective *impurity* model is replaced with the multi-impurity model, *i.e.* the effective *cluster* model. Several versions of the cluster extension of the dynamical mean field theory have been proposed. Typical methods are the cellular dynamical mean field theory [104, 116, 117] proposed by Kotliar *et al.* and the dynamical cluster approximation [118–121] by Jarrell *et al.* In this subsection, the cellular dynamical mean field theory is explained and the dynamical cluster approximation is introduced in the next subsection.

As shown in Fig. 2.2, in the cellular dynamical mean field theory, the original lattice model is approximately mapped onto the effective cluster model which consists of a few site cluster and an effective medium. In the effective cluster model, the short-range correlation effects in addition to the local correlations in the cluster are correctly calculated. In the following, as an example, in the $N_c = 2 \times 2$ site cluster cellular dynamical mean field theory for the two-dimensional Hubbard model, the way to map the original model onto the effective cluster model is explained.

To carry out the mapping onto the effective cluster model shown in Fig. 2.2, the original lattice is divided into four sublattices, as shown in Fig. 2.3. Four sites surrounded by dotted line in Fig. 2.3 are regarded as one site. Then, the length of the primitive translation vectors become twice, as shown by the arrows in the figure so that the corresponding reciprocal vectors become half.

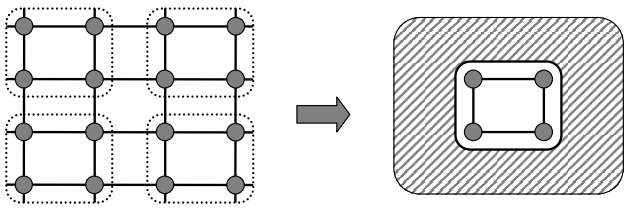

Figure 2.2: In the cellular dynamical mean field theory, the original lattice model (left) is mapped onto the effective cluster model (right) which consists of a few site cluster coupled to an effective medium. A cluster including some sites is regard as one site in the framework of the cellular dynamical mean field theory.

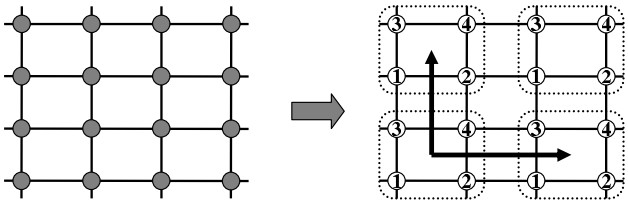

Figure 2.3: The original lattice (left) and the lattice divided into four sublattices (right). The arrow in the right figure denotes the primitive translation vector which connects between the same sublattices.

In the sublattice representation, the Hubbard Hamiltonian reads

$$H = H_0 + H_I, \tag{2.35}$$

$$H_0 = \sum_{i,j,\gamma,\delta,\sigma} t_{\gamma\delta}\,(i,j)\, c^\dagger_{i\gamma\sigma} c_{j\delta\sigma} - \mu \sum_{i,\gamma,\sigma} c^\dagger_{i\gamma\sigma} c_{i\gamma\sigma}, \tag{2.36}$$

$$H_I = U \sum_{i,\gamma} n_{i\gamma\uparrow} n_{i\gamma\downarrow}. \tag{2.37}$$

Here, $c^\dagger_{i\gamma}$ ($c_{i\gamma}$) creates (annihilates) an electron at the ith site in the sublattice γ ($\gamma = 1, 2, 3, 4$). The hopping integral between the ith site in the sublattice γ and jth site in the sublattice δ is described by $t_{\gamma\delta}(i,j)$ and U is the Hubbard interaction. In the above expressions, an electron with spin σ at each site has four sublattice degrees of freedom, $1, 2, 3, 4$. In order to derive the cellular dynamical mean field theory, it is convenient to regard sublattice indices as not an index which denotes a particular site in the real space but *an internal degree of freedom* at a site.

Under this expression, the non-interacting Hamiltonian is converted to the wave vector representation. The usual Fourier transformation is defined as

$$c_{\tilde{\mathbf{k}}\gamma\sigma} = \frac{1}{\sqrt{N'}} \sum_i \mathrm{e}^{-i\tilde{\mathbf{k}}\cdot(\tilde{\mathbf{r}}_i + \mathbf{R}_\gamma)} c_{i\gamma\sigma}. \tag{2.38}$$

In the expression in Eq. (2.36), however, the sublattice indices are regarded as internal degrees of freedom so the Fourier transformation is defined as

$$\tilde{c}_{\tilde{\mathbf{k}}\gamma\sigma} = \frac{1}{\sqrt{N'}} \sum_i \mathrm{e}^{-i\tilde{\mathbf{k}}\cdot\tilde{\mathbf{r}}_i} c_{i\gamma\sigma}. \tag{2.39}$$

Here, N' is the number of sites and the total number of sites which includes all sublattices is $N = N_c \times N'$. By using the Fourier transformation (2.39),

H_0 is rewritten as

$$H_0 = \sum_{\tilde{\mathbf{k}},\gamma,\delta,\sigma} t_{\gamma\delta}\left(\tilde{\mathbf{k}}\right) \tilde{c}^{\dagger}_{\tilde{\mathbf{k}}\gamma\sigma} \tilde{c}_{\tilde{\mathbf{k}}\delta\sigma} - \mu \sum_{\tilde{\mathbf{k}},\gamma,\sigma} \tilde{c}^{\dagger}_{\tilde{\mathbf{k}}\gamma\sigma} \tilde{c}_{\tilde{\mathbf{k}}\gamma\sigma}, \tag{2.40}$$

$$t_{\gamma\delta}\left(\tilde{\mathbf{k}}\right) = \frac{1}{N'} \sum_{i,j} e^{-i\tilde{\mathbf{k}}\cdot(\tilde{\mathbf{r}}_i - \tilde{\mathbf{r}}_j)} t_{\gamma\delta}\left(i,j\right). \tag{2.41}$$

The full Green's function for the total Hamiltonian defined by

$$\tilde{G}_{\gamma\delta\sigma}\left(\tilde{\mathbf{k}} : \tau\right) = -\left\langle T_\tau \tilde{c}_{\tilde{\mathbf{k}}\delta\sigma}\left(\tau\right) \tilde{c}^{\dagger}_{\tilde{\mathbf{k}}\gamma\sigma}\left(0\right)\right\rangle, \tag{2.42}$$

is obtained as

$$\hat{\tilde{G}}_\sigma\left(\tilde{\mathbf{k}} : \omega\right) = \left[(\omega+\mu)\hat{1} - \hat{t}\left(\tilde{\mathbf{k}}\right) - \hat{\tilde{\Sigma}}_\sigma\left(\tilde{\mathbf{k}} : \omega\right)\right]^{-1}, \tag{2.43}$$

in terms of the self-energy $\Sigma_{\gamma\delta\sigma}$. Here, $\hat{O}$ denotes that O is $N_c \times N_c$ matrix.

Under the above preparations, the model (2.35) is mapped onto the effective cluster model. We regarded sublattice degrees of freedom as internal degrees of freedom so then we can derive the effective cluster model in the cellular dynamical mean field theory by almost the same procedure as the standard dynamical mean field theory explained in the previous section. Starting from the path integral representation of the partition function given by

$$Z = \int \prod_{i,\gamma,\sigma} \mathcal{D}c^{\dagger}_{i\gamma\sigma} \mathcal{D}c_{i\gamma\sigma} e^{-S}, \tag{2.44}$$

$$S = S_0 + \Delta S + S^{(0)}, \tag{2.45}$$

$$\begin{aligned} S_0 = \int_0^\beta d\tau \Bigg\{ \sum_{\gamma,\sigma} c^{\dagger}_{0\gamma\sigma}(\tau) \left[\left(\frac{\partial}{\partial\tau} - \mu\right)\delta_{\gamma,\delta} + t_{\gamma\delta}\left(0,0\right)\right] c_{0\delta\sigma}(\tau) \\ + U \sum_{\gamma} n_{0\gamma\uparrow}\left(\tau\right) n_{0\gamma\downarrow}\left(\tau\right) \Bigg\}, \end{aligned} \tag{2.46}$$

$$\Delta S = \int_0^\beta d\tau \sum_{i,\gamma,\delta,\sigma} \left[t_{\gamma\delta}\left(i,0\right) c^{\dagger}_{i\gamma\sigma}\left(\tau\right) c_{0\delta\sigma}\left(\tau\right) + t_{\gamma\delta}\left(0,i\right) c^{\dagger}_{0\gamma\sigma}\left(\tau\right) c_{i\delta\sigma}\left(\tau\right)\right], \tag{2.47}$$

$$\begin{aligned} S^{(0)} = \int_0^\beta d\tau \Bigg\{ \sum_{i,j\neq 0,\gamma,\sigma} c^{\dagger}_{i\gamma\sigma}(\tau) \left[\left(\frac{\partial}{\partial\tau} - \mu\right)\delta_{\gamma,\delta} + t_{\gamma\delta}\left(0,0\right)\right] c_{j\delta\sigma}(\tau) \\ + U \sum_{i\neq 0,\gamma} n_{0\gamma\uparrow}\left(\tau\right) n_{0\gamma\downarrow}\left(\tau\right) \Bigg\}, \end{aligned} \tag{2.48}$$

we expand Z in powers of ΔS and obtain the effective action,

$$S_{\text{eff}} = -\int_0^\beta d\tau_1 d\tau_2 \sum_{\gamma,\delta,\sigma} c^\dagger_{0\gamma\sigma}(\tau_1)\mathcal{G}^{-1}_{\gamma\delta\sigma}(\tau_1-\tau_2)c_{0\delta\sigma}(\tau_2) + U\int_0^\beta d\tau \sum_\gamma n_{0\gamma\uparrow}(\tau)n_{0\gamma\downarrow}(\tau). \tag{2.49}$$

Here, the Green's function for the effective medium $\mathcal{G}^{-1}_{\gamma\delta\sigma}(\omega)$ is obtained as

$$\mathcal{G}^{-1}_{\gamma\delta\sigma}(\omega) = \omega + \mu - t_{\gamma\delta}(0,0) - \sum_{ij}\sum_{\gamma'\delta'} t_{\gamma\gamma'}(i,0)\, G^{(0)}_{\gamma'\delta'\sigma}(i,j:\omega)\, t_{\delta'\delta}(j,0), \tag{2.50}$$

where the cavity Green's function is defined by

$$G^{(0)}_{\gamma\delta\sigma}(i,j:\tau) = -\left\langle T_\tau c_{i\gamma\sigma}(\tau)\, c^\dagger_{j\delta\sigma}(0)\right\rangle^{(0)}. \tag{2.51}$$

We can also use the corresponding effective Hamiltonian to the action (2.49),

$$H = \sum_{\gamma,\delta,\sigma} t_{\gamma\delta}(0,0)\, c^\dagger_{0\gamma\sigma}c_{0\delta\sigma} - \mu\sum_{\gamma,\sigma} c^\dagger_{0\gamma\sigma}c_{0\gamma\sigma} + U\sum_\gamma n_{0\gamma\uparrow}n_{0\gamma\downarrow} + \sum_{l,\sigma}\varepsilon_l a^\dagger_{l\sigma}a_{l\sigma} + \sum_{l,\gamma,\sigma}\left(V_{l\gamma}a^\dagger_{l\sigma}c_{0\gamma\sigma} + \text{H.c.}\right). \tag{2.52}$$

In this case, the Green's function for the effective medium is computed as

$$\mathcal{G}^{-1}_{\gamma\delta\sigma}(\omega) = (\omega+\mu)\,\delta_{\gamma,\delta} - t_{\gamma\delta}(0,0) - \Delta_{\gamma\delta}(\omega), \tag{2.53}$$

where the hybridization function is given by

$$\Delta_{\gamma\delta}(\omega) = \sum_l \frac{V_{l\gamma}V_{l\delta}}{(\omega-\epsilon_l)} = G^{(0)}_{\gamma\delta\sigma}(i,j:\tau). \tag{2.54}$$

By generalization of Eq. (2.26), the relation between the cavity Green's function $G^{(0)}_{\gamma'\delta'\sigma}(i,j:\omega)$ and the lattice full Green's function $G_{\gamma\delta\sigma}(i,j:\omega)$ is the matrix formula,

$$\hat{G}^{(0)}_\sigma(i,j) = \hat{G}_\sigma(i,j) - \hat{G}_\sigma(i,0)\,\hat{G}^{-1}_\sigma(0,0)\,\hat{G}_\sigma(0,j). \tag{2.55}$$

By using this relation, Eq. (2.53) is transformed into

$$\begin{aligned}
\hat{\mathcal{G}}_{\sigma}^{-1}(\omega) &= [\omega+\mu]\,\hat{1} - \hat{t}\,(0,0) - \sum_{ij}\hat{t}\,(i,0)\,\hat{G}_{\sigma}^{(0)}\,(i,j)\,\hat{t}\,(j,0) \\
&= [\omega+\mu]\,\hat{1} - \hat{t}\,(0,0) - \sum_{ij}\hat{t}\,(i,0)\,\hat{G}_{\sigma}\,(i,j)\,\hat{t}\,(j,0) \\
&+ \sum_{ij}\hat{t}\,(i,0)\,\hat{G}_{\sigma}\,(i,0)\,\hat{G}_{\sigma}^{-1}\,(0,0)\,\hat{G}_{\sigma}\,(0,j)\,\hat{t}\,(j,0) \\
&= [\omega+\mu]\,\hat{1} - \hat{t}\,(0,0) - \frac{1}{N'}\sum_{\tilde{\mathbf{k}}}\hat{t}\left(\tilde{\mathbf{k}}\right)\hat{\tilde{G}}_{\sigma}\left(\tilde{\mathbf{k}}\right)\hat{t}\left(\tilde{\mathbf{k}}\right) \\
&+ \left[\frac{1}{N'}\sum_{\tilde{\mathbf{k}}}\hat{t}\left(\tilde{\mathbf{k}}\right)\hat{\tilde{G}}_{\sigma}\left(\tilde{\mathbf{k}}\right)\right]\hat{G}_{\sigma}^{-1}\,(0,0)\left[\frac{1}{N'}\sum_{\tilde{\mathbf{k}}}\hat{\tilde{G}}_{\sigma}\left(\tilde{\mathbf{k}}\right)\hat{t}\left(\tilde{\mathbf{k}}\right)\right].
\end{aligned} \tag{2.56}$$

Here, $\hat{\tilde{G}}_{\sigma}\left(\tilde{\mathbf{k}}\right)$ is the Green's function given by Eq. (2.43) and the argument ω in $\hat{\tilde{G}}_{\sigma}$ is omitted for convenience. By ignoring the momentum dependence of the self-energy, $\hat{\tilde{G}}_{\sigma}\left(\tilde{\mathbf{k}}\right)$ is approximated as

$$\begin{aligned}
\hat{\tilde{G}}_{\sigma}\left(\tilde{\mathbf{k}}:\omega\right) &\to \left[(\omega+\mu)\,\hat{1} - \hat{t}\left(\tilde{\mathbf{k}}\right) - \hat{\Sigma}_{\sigma}\,(\omega)\right]^{-1} \\
&= \left[\hat{X}_{\sigma}\,(\omega) - \hat{t}\left(\tilde{\mathbf{k}}\right)\right]^{-1}.
\end{aligned} \tag{2.57}$$

Under this approximation, the summations over the wave vector in Eq. (2.56) are computed as

$$\frac{1}{N'}\sum_{\tilde{\mathbf{k}}}\hat{t}\left(\tilde{\mathbf{k}}\right)\hat{\tilde{G}}_{\sigma}\left(\tilde{\mathbf{k}}\right)\hat{t}\left(\tilde{\mathbf{k}}\right) = -\hat{t}\,(0,0) - \hat{X}_{\sigma} + \hat{X}\hat{G}_{\sigma}\,(0,0)\,\hat{X}_{\sigma}, \tag{2.58}$$

$$\frac{1}{N'}\sum_{\tilde{\mathbf{k}}}\hat{t}\left(\tilde{\mathbf{k}}\right)\hat{\tilde{G}}_{\sigma}\left(\tilde{\mathbf{k}}\right) = -\hat{1} + \hat{X}_{\sigma}\hat{G}_{\sigma}\,(0,0)\,, \tag{2.59}$$

$$\frac{1}{N'}\sum_{\tilde{\mathbf{k}}}\hat{\tilde{G}}_{\sigma}\left(\tilde{\mathbf{k}}\right)\hat{t}\left(\tilde{\mathbf{k}}\right) = -\hat{1} + \hat{G}_{\sigma}\,(0,0)\,\hat{X}_{\sigma}. \tag{2.60}$$

Finally, the Green's function for the effective medium is obtained as

$$\hat{\mathcal{G}}_{\sigma}^{-1}(\omega) = \left(\frac{1}{N'}\sum_{\tilde{\mathbf{k}}}\left[(\omega+\mu)\,\hat{1} - \hat{t}\left(\tilde{\mathbf{k}}\right) - \hat{\Sigma}_{\sigma}\,(\omega)\right]^{-1}\right)^{-1} + \hat{\Sigma}_{\sigma}\,(\omega)\,. \tag{2.61}$$

This can be calculated by the self-energy defined in the effective cluster model, $\hat{\Sigma}_\sigma(\omega)$. By solving the effective action (2.49), the self-energy $\hat{\Sigma}_\sigma(\omega)$ is obtained and then the effective medium is recomputed by Eq. (2.61). Iterating this procedure, we determine the effective medium self-consistently.

The cellular dynamical mean field theory has been applied to the one-dimensional Hubbard model and extended Hubbard model [122, 123] and it has been shown that the results are in good agreement with those of the Bethe ansatz and density matrix renormalization group. Recently, this method has been successfully applied to the two-dimensional Hubbard model related to the high-T_c cuprate [124] and the periodic Anderson model which describes the quantum phase transition in the f-electron systems [125]. The Mott transition in the Hubbard model with geometrical frustration, which is related to the metal-insulator transition observed in the κ-type organics, has been also studied [27, 126, 127] by using the cellular dynamical mean field theory. The combination of this method with the band calculations have been proposed and challenge for giving quantitative explanation of experimental results has been done [128]. In the cellular dynamical mean field theory, however, has a problem that the translational symmetry is broken in the procedure of mapping onto the effective cluster model, which causes a problem in particular in describing the d-wave superconductivity [105]. The periodized cluster dynamical mean field theory recently proposed keeps the translational symmetry and improves this point [129].

2.2.2 Dynamical Cluster Approximation

In this subsection, another cluster extension of the dynamical mean field theory, the dynamical cluster approximation is briefly introduced and it is compared with the cellular dynamical mean field theory. In the single-site dynamical mean field theory, the $\mathbf{k}$-dependence of the self-energy is ignored. In other words, the self-energies $\Sigma_\sigma(\mathbf{k})$ at all $\mathbf{k}$ points are replaced with one self-energy $\Sigma_\sigma(\mathbf{k}_\Gamma : \omega)$ at the Γ point. Here, $\mathbf{k}_\Gamma = (0, 0, \dots)$. In this case, the lattice Green's function is given by

$$G_\sigma(\mathbf{k} : \omega) = \left[\omega + \mu - \varepsilon_{\mathbf{k}} - \Sigma_\sigma(\omega)\right]^{-1}. \tag{2.62}$$

In the dynamical cluster approximation, the Brillouin zone is divided into several regions called the *coarse grained cell*. The number of coarse grained cell N_c corresponds to the cluster size in the cellular dynamical mean field theory, as explained below. For each coarse grained cell, a *cluster momentum* $\mathbf{K}$, which is a typical $\mathbf{k}$ point in each coarse grained cell, is assigned. By using the cluster momentum $\mathbf{K}$, $N' = N/N_c$ self-energies with wave vector $\mathbf{k}$

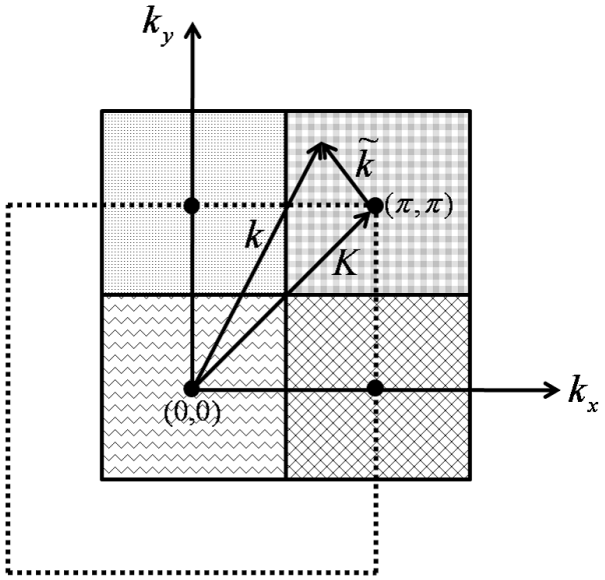

Figure 2.4: An example for division of the Brillouin zone of the square lattice. The cluster size is $N_c = 4$. The dashed square denotes the first Brillouin zone and four filled circles denote the cluster momenta.

in each coarse grained cell, $\Sigma_\sigma(\mathbf{k})$, are approximately replaced with one self-energy with cluster momentum $\mathbf{K}$, $\Sigma_\sigma(\mathbf{K})$. In Fig. (2.4), the two-dimensional Brillouin zone is divided into $N_c = 4$ coarse grained cells and N self-energies $\Sigma_\sigma(\mathbf{k})$ are replaced with four self-energies $\Sigma_\sigma(\mathbf{K})$. Therefore, in the dynamical cluster approximation, the Green's function is written in terms of N_c self-energies $\Sigma_\sigma(\mathbf{K})$ as

$$G_\sigma(\mathbf{k} : \omega) = \left[\omega + \mu - \varepsilon_{\mathbf{k}} - \Sigma_\sigma(\mathbf{K} : \omega)\right]^{-1}. \tag{2.63}$$

Note that in the Green's function with the wave vector $\mathbf{k}$, the self-energy with the cluster momentum $\mathbf{K}$ in the coarse grained cell which includes $\mathbf{k}$. For $N_c = 1$, this approximation corresponds to the single-site dynamical mean field theory and for $N_c = N$, it becomes exact. In the cellular dynamical mean field theory, the effective cluster model is derived in the real space, while in the dynamical cluster approximation, the momentum space is coarse-grained and the effective cluster model is constructed in the momentum space.

Let us now consider the effective Hamiltonian in the dynamical cluster approximation. The Hubbard model in $\mathbf{k}$ space reads,

$$H = \sum_{\mathbf{k},\sigma} \left(\varepsilon_{\mathbf{k}} - \mu\right) c^\dagger_{\mathbf{k}\sigma} c_{\mathbf{k}\sigma} + \frac{U}{N} \sum_{\mathbf{k},\mathbf{k}',\mathbf{q}} c^\dagger_{\mathbf{k}+\mathbf{q}\uparrow} c_{\mathbf{k}\uparrow} c^\dagger_{\mathbf{k}'-\mathbf{q}\downarrow} c_{\mathbf{k}'\downarrow}. \tag{2.64}$$

Here, $\varepsilon_{\mathbf{k}}$ is the dispersion relation, that is, the usual Fourier transformation defined by (2.38) of the hopping integral t_{ij}. In the dynamical cluster approximation, the $\mathbf{k}$ space is coarse-grained, as above mentioned. So, the dispersion is averaged in each coarse grained cell,

$$\varepsilon_{\mathbf{k}} \to \bar{\varepsilon}_{\mathbf{K}} = \frac{1}{N'} \sum_{\tilde{\mathbf{k}}} \varepsilon_{\mathbf{K}+\tilde{\mathbf{k}}}. \tag{2.65}$$

Here, the wave vector $\mathbf{k}$ is replaced with the cluster momentum $\mathbf{K}$ in the coarse grained cell which includes $\mathbf{k}$ and also, the summation over $\tilde{\mathbf{k}}$ is taken in each coarse grained cell which includes $\mathbf{k}$. The interaction term is also averaged. For a generalized $\mathbf{q}$-dependent interaction $U_{\mathbf{q}}$, the averaged interaction reads

$$U_{\mathbf{q}} \to \bar{U}_{\mathbf{Q}} = \frac{1}{N'} \sum_{\tilde{\mathrm{q}}} U_{\mathbf{Q}+\tilde{\mathbf{q}}}. \tag{2.66}$$

In the Hubbard model without $\mathbf{q}$-dependence of the interaction, simply $\bar{U} = U$. The cluster part is coupled to the effective medium so that the total effective Hamiltonian is the multi-impurity Anderson Hamiltonian as well as that in the cellular dynamical mean field theory (2.52),

$$\begin{aligned} H_{\text{eff}} = &\sum_{\mathbf{K},\sigma} \bar{\varepsilon}_{\mathbf{K}} c^{\dagger}_{\mathbf{K}\sigma} c_{\mathbf{K}\sigma} + \frac{U}{N_c} \sum_{\mathbf{K},\mathbf{K}',\mathbf{Q}} c^{\dagger}_{\mathbf{K}+\mathbf{Q}\uparrow} c_{\mathbf{K}\uparrow} c^{\dagger}_{\mathbf{K}-\mathbf{Q}\downarrow} c_{\mathbf{K}\downarrow} \\ &+ \sum_{\mathbf{k},\sigma} E_{\mathbf{k}} a^{\dagger}_{\mathbf{k}\sigma} a_{\mathbf{k}\sigma} + \frac{1}{N'} \sum_{\mathbf{K},\tilde{\mathbf{k}},\sigma} \left[V_{\mathbf{K}\tilde{\mathbf{k}}} c^{\dagger}_{\mathbf{K}\sigma} a_{\mathbf{K}+\tilde{\mathbf{k}}\sigma} + \text{H.c.} \right]. \end{aligned} \tag{2.67}$$

Here, $a^{\dagger}_{\mathbf{k}\sigma}$ ($a_{\mathbf{k}\sigma}$) creates (annihilates) a fermion in the effective medium. The bath fermion has the dispersion $E_{\mathbf{k}}$ and it is coupled to the cluster fermion by $V_{\mathbf{K}\tilde{\mathbf{k}}}$. The coarse grained Green's function defined by $\bar{G}_{\sigma}(\mathbf{K} : \tau) = -\langle T_{\tau} c_{\mathbf{K}\sigma}(\tau) c^{\dagger}_{\mathbf{K}\sigma}(\tau) \rangle$ and the self-energy $\Sigma_{\mathbf{K}\sigma}$ is computed in the effective cluster Hamiltonian (2.67). These satisfy the Dyson equation, $\bar{G}_{\sigma}(\mathbf{K}) = \mathcal{G}_{\sigma}(\mathbf{K}) + \mathcal{G}_{\sigma}(\mathbf{K}) \Sigma_{\sigma}(\mathbf{K}) \bar{G}_{\sigma}(\mathbf{K})$. Here, the Green's function for the effective medium $\mathcal{G}_{\mathbf{K}\sigma}$ is calculated as

$$\mathcal{G}^{-1}_{\sigma}(\mathbf{K} : \omega) = \omega + \mu - \bar{\varepsilon}_{\mathbf{K}} - \Delta(\mathbf{K} : \omega) - \Sigma_{\sigma}(\mathbf{K} : \omega), \tag{2.68}$$

$$\Delta(\mathbf{K} : \omega) = \frac{1}{N} \sum_{\tilde{\mathbf{k}}} \frac{|V_{\mathbf{K}\tilde{\mathbf{k}}}|^2}{\omega - E_{\mathbf{K}+\tilde{\mathbf{k}}}}, \tag{2.69}$$

where $\Delta(\mathbf{K} : \omega)$ is the hybridization function. On the other hand, for given the self-energy $\Sigma_{\sigma}(\mathbf{K} : \omega)$, the coarse grained Green's function is also obtained

by averaging the lattice Green's function given by Eq. (2.63) in each coarse grained cell as

$$\bar{G}_\sigma(\mathbf{K}:\omega) = \frac{1}{N'}\sum_{\tilde{\mathbf{k}}} \frac{1}{\omega+\mu-\varepsilon_{\mathbf{K}+\tilde{\mathbf{k}}}-\Sigma_\sigma(\mathbf{K},\omega)}. \tag{2.70}$$

Therefore, by using the above expression and the Dyson equation, the Green's function for the effective medium is recomputed as

$$\mathcal{G}_\sigma^{-1}(\mathbf{K}:\omega) = \left[\frac{1}{N'}\sum_{\tilde{\mathbf{k}}} \frac{1}{\omega+\mu-\varepsilon_{\mathbf{K}+\tilde{\mathbf{k}}}-\Sigma_\sigma(\mathbf{K}:\omega)}\right]^{-1} + \Sigma_\sigma(\mathbf{K}:\omega). \tag{2.71}$$

Also, the hybridization function is

$$\Delta(\mathbf{K}:\omega) = \omega+\mu-\left[\frac{1}{N'}\sum_{\tilde{\mathbf{k}}} \frac{1}{\omega+\mu-\varepsilon_{\mathbf{K}+\tilde{\mathbf{k}}}-\Sigma_\sigma(\mathbf{K}:\omega)}\right]^{-1}. \tag{2.72}$$

These equations determine the bath parameters in the effective Hamiltonian (2.67). By solving the effective Hamiltonian, we again compute the coarse-grained Green's function and the self-energy. This procedure is iterated until numerical convergence is reached.

If we choose a specific **k**-space cluster with a corresponding real-space cluster, we can derive the dynamical cluster approximation also using the same procedure as the cellular dynamical mean field theory. The difference between the dynamical cluster approximation and cellular dynamical mean field theory is whether the periodic boundary condition is imposed on the cluster or the open one is. In the cellular dynamical mean field theory, as explained in the previous subsection, the open boundary condition is employed. On the other hand, the dynamical cluster approximation is formulated in **k** space, which indicates that the periodic boundary condition is imposed on the cluster. This difference influences the Fourier transformation of the hopping matrix element. To convert the cellular dynamical mean field theory to the dynamical cluster approximation, in the derivation of the cellular dynamical mean field theory explained in the previous subsection, we should just change $t_{\gamma\delta}(\mathbf{k})$ into $\varepsilon_{\gamma\delta}(\mathbf{k})$,

$$\begin{aligned}\varepsilon_{\gamma\delta}\left(\tilde{\mathbf{k}}\right) &= \frac{1}{N'}\sum_{i,j} e^{-i\tilde{\mathbf{k}}\cdot(\tilde{\mathbf{r}}_i+\mathbf{R}_\gamma-\tilde{\mathbf{r}}_j-\mathbf{R}_\delta)} t_{\gamma\delta}\left(i,j\right) \\ &= e^{-i\tilde{\mathbf{k}}\cdot(\mathbf{R}_\gamma-\mathbf{R}_\delta)} t_{\gamma\delta}\left(\tilde{\mathbf{k}}\right),\end{aligned} \tag{2.73}$$

which corresponds to change from the open boundary condition to the periodic one. Note that in this case, the relation between the cavity Green's function and the lattice full Green's function given by Eq. (2.55) is not justified. The effective action and Green's function for the effective medium are obtained as

$$S_{\text{eff}} = -\int_0^\beta d\tau_1 d\tau_2 \sum_{\gamma,\delta,\sigma} c^\dagger_{0\gamma\sigma}(\tau_1)\mathcal{G}^{-1}_{\gamma\delta\sigma}(\tau_1-\tau_2)c_{0\delta\sigma}(\tau_2) + U\int_0^\beta d\tau \sum_\gamma n_{0\gamma\uparrow}(\tau)n_{0\gamma\downarrow}(\tau), \tag{2.74}$$

$$\hat{\mathcal{G}}^{-1}_\sigma(\omega) = \left(\frac{1}{N'}\sum_{\tilde{\mathbf{k}}}\left[(\omega+\mu)\,\hat{1} - \hat{\varepsilon}_{\tilde{\mathbf{k}}} - \hat{\Sigma}_\sigma(\omega)\right]^{-1}\right)^{-1} + \hat{\Sigma}_\sigma(\omega)\,. \tag{2.75}$$

Furthermore, the effective medium $\hat{\mathcal{G}}^{-1}_\sigma(\omega)$ is diagonalized by the Fourier transformation from the sublattice representation to the cluster-momentum one, because the cluster is translationally symmetric due to the periodic boundary condition. The Fourier transformation is defined by

$$c_{i\gamma\sigma} = \frac{1}{\sqrt{N_c}}\sum_{\mathbf{K}} e^{i\mathbf{K}\cdot\mathbf{R}_\gamma} c_{i\mathbf{K}\sigma}. \tag{2.76}$$

We thus obtain

$$S_{\text{eff}} = -\int_0^\beta d\tau_1 d\tau_2 \sum_{\mathbf{K},\sigma} c^\dagger_{0\mathbf{K}\sigma}(\tau_1)\mathcal{G}^{-1}_{\mathbf{K}\sigma}(\tau_1-\tau_2)c_{0\mathbf{K}\sigma}(\tau_2) + \int_0^\beta d\tau \frac{U}{N_c}\sum_{\mathbf{K},\mathbf{K}',\mathbf{Q}} c^\dagger_{0\mathbf{K}+\mathbf{Q}\uparrow}(\tau)c_{0\mathbf{K}\uparrow}(\tau)c^\dagger_{0\mathbf{K}'-\mathbf{Q}\downarrow}(\tau)c_{0\mathbf{K}'\downarrow}(\tau), \tag{2.77}$$

$$\mathcal{G}^{-1}_\sigma(\mathbf{K}:\omega) = \left[\frac{1}{N'}\sum_{\tilde{\mathbf{k}}}\frac{1}{\omega+\mu-\varepsilon_{\mathbf{K}+\tilde{\mathbf{k}}}-\Sigma_\sigma(\mathbf{K}:\omega)}\right]^{-1} + \Sigma_\sigma(\omega), \tag{2.78}$$

which are consistent with the effective Hamiltonian (2.67) and the effective medium (2.71), respectively.

The dynamical cluster approximation has been successfully applied to the two-dimensional Hubbard model [130–132]. In these studies, the cluster size dependence has been systematically investigated and much better convergence than the simulations in the finite size system has been obtained. Also, the doping dependence of the d-wave superconductivity, antiferromagnetism [133] and pseudo-gap [120] have been studied and the phase diagram

has been obtained, which qualitatively explain the experimental results in High-T_c cuprates. This method has been also successful applied to the triangular lattice Hubbard model and it has been found that geometrical frustration stabilizes the Fermi-liquid metallic state [134].

Chapter 3

Linearization of DMFT and Cluster DMFT

In the previous chapter, we reviewed the (ordinal) dynamical mean field theory and its cluster extensions, *i.e.*, the cellular dynamical mean field theory and the dynamical cluster approximation. In these theories, the original lattice model is mapped onto an effective model, in which a single impurity site or a cluster is embedded in an effective medium. At this point, we need some solvers for this effective model. For example, we can use numerical techniques, such as quantum Monte Carlo method [72–74, 135], exact diagonalization [136], numerical renormalization group [88] and so on. They are *semi-exact*, but require quite heavy computations. On the other hand, we can also use approximations as in the iterative perturbation theory [137–139] or in the dynamical mean field theory with non-crossing approximation [140, 141]. They do not need heavy numerical calculation, but works only in the limited parameter region of the interaction and the temperature.

If we focus on the absolute zero temperature, the two-site (linearized) dynamical mean field theory is considered to be effective [142]. Although the calculation scheme is extremely simplified, its solution still captures the low-energy features of the Green's functions properly. Further, it can be applied in the wide region of interaction parameter, even where the iterative perturbation theory or the non-crossing approximation solvers break down, and provides a unified description of the system from weak to strong coupling regime.

In the present chapter, we will review the framework of the two-site dynamical mean field theory using the Hubbard model as an example. Then, we extend it to the cluster version, which are called the linearized cellular dynamical mean field theory and the linearized dynamical cluster approximation, which enable us to discuss the (short-range) spatial fluctuation effects.

3.1 Two-Site Dynamical Mean Field Theory

In the present section, we briefly review the two-site dynamical mean field theory. As an example of lattice systems, we deal with the Hubbard Hamiltonian (2.1),

$$H = \sum_{i,j,\sigma} t_{ij} c_{i\sigma}^{\dagger} c_{j\sigma} - \mu \sum_{i,\sigma} c_{i\sigma}^{\dagger} c_{i\sigma} + U \sum_{i} n_{i\uparrow} n_{i\downarrow}. \tag{3.1}$$

Let us begin with approximating the local (site-diagonal) Green's function to

$$\begin{aligned} G_{\mathrm{loc}\sigma}(\omega) \equiv G_{00\sigma}(\omega) &= \overline{\left[\omega - \varepsilon_{\mathbf{k}} + \mu - \Sigma_{\sigma}(\omega)\right]^{-1}} \\ &= \int d\varepsilon \frac{\rho_0(\varepsilon)}{\omega + \mu - \Sigma_{\sigma}(\omega) - \varepsilon}, \end{aligned} \tag{3.2}$$

by neglecting the $\mathbf{k}$-dependence of the self-energy. Here, we follow the notations introduced in the section 2.1, and define the average of the $\mathbf{k}$-dependent quantity $O(\mathbf{k})$ as

$$\overline{O(\mathbf{k})} = \frac{1}{N} \sum_{\boldsymbol{k}} O(\mathbf{k}). \tag{3.3}$$

With this average, the non-interacting density of states is expressed as

$$\rho_0(\varepsilon) = \overline{\delta(\varepsilon - \varepsilon_{\mathbf{k}})}. \tag{3.4}$$

This lattice model is mapped onto the effective impurity model described by the Anderson Hamiltonian (2.23), where the medium around the impurity

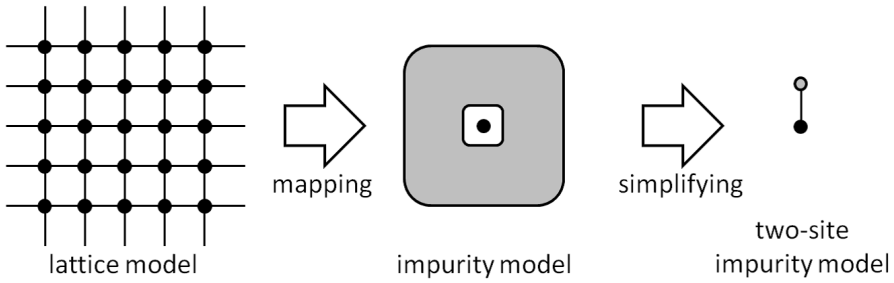

Figure 3.1: The concept of the two-site dynamical mean field theory. The lattice model is mapped onto an effective Anderson model, and the medium for the impurity is approximately represented by a single site.

is represented by an infinite number of bath sites. In the two-site dynamical mean field theory, the number of bath sites is reduced to one: the effective impurity model consists of two sites, a single impurity and a single bath sites. The relationship among the original lattice model, the effective impurity and the simplified two-site models are summarized in Fig. 3.1. The Hamiltonian of this two-site model is given as

$$\begin{aligned} H_{\mathrm{imp}} = & \sum_{\sigma} (t_0 - \mu) c_\sigma^\dagger c_\sigma + U n_{\mathrm{c}\uparrow} n_{\mathrm{c}\downarrow} \\ & + \sum_{\sigma} \varepsilon_{\mathrm{a}\sigma} a_\sigma^\dagger a_\sigma + \sum_{\sigma} \left[V_\sigma a_\sigma^\dagger c_\sigma + \mathrm{H.c.} \right], \end{aligned} \tag{3.5}$$

with

$$t_0 \equiv t_{ii} = \overline{\varepsilon_{\mathbf{k}}} = \int d\varepsilon \, \varepsilon \rho_0(\varepsilon), \tag{3.6}$$

which is assumed to be zero in the previous section 2.1. In this Hamiltonian, the energy levels of the bath site $\varepsilon_{\mathrm{a}\sigma}$ and the hybridization V_σ are the unknown parameters. Without loss of generality, the hybridization parameter V_σ can be assumed to be real.

Now, let us give an initial guess for the parameters $\varepsilon_{\mathrm{a}\sigma}$ and V_σ. Then, the medium Green's function, *i.e.*, the bare impurity Green's function ($U = 0$), is explicitly written as

$$\mathcal{G}_\sigma(\omega) = \left[\omega + \mu - t_0 - \Delta_\sigma(\omega) \right]^{-1}, \tag{3.7}$$

with

$$\Delta_\sigma(\omega) = \frac{V_\sigma^2}{\omega - \varepsilon_{\mathrm{a}\sigma}}. \tag{3.8}$$

The full impurity Green's function ($U \neq 0$) can also be calculated numerically. Actually, it is represented in the Lehmann-Kallen form as

$$G_{\mathrm{imp}\sigma}(\omega) = \sum_{m(\neq 0)} \frac{\left| \langle m | c_\sigma^\dagger | 0 \rangle \right|^2}{\omega + i0 - E_m + E_0} + \sum_{m(\neq 0)} \frac{\left| \langle m | c_\sigma | 0 \rangle \right|^2}{\omega + i0 - E_0 + E_m}, \tag{3.9}$$

at zero temperature, where the eigenpairs E_m and $|m\rangle$ are computed by means of the exact diagonalization of the Hamiltonian (3.5), and $m = 0$ denotes the ground state. At the same time, the impurity self-energy is evaluated with the Dyson equation as

$$\begin{aligned} \Sigma_{\mathrm{imp}\sigma}(\omega) &= \mathcal{G}_\sigma^{-1}(\omega) - G_{\mathrm{imp}\sigma}^{-1}(\omega) \\ &= \omega + \mu - t_0 - \Delta_\sigma(\omega) - G_{\mathrm{imp}\sigma}^{-1}(\omega), \end{aligned} \tag{3.10}$$

which also gives

$$G_{\mathrm{imp}\sigma}(\omega) = \left[\omega + \mu - t_0 - \Sigma_{\mathrm{imp}\sigma}(\omega) - \Delta_\sigma(\omega)\right]^{-1}. \tag{3.11}$$

If an *exact* solver for the impurity model with infinite bath sites is available, the parameters in the effective impurity model are chosen in such a way that the self-consistent condition (2.9),

$$\mathcal{G}_\sigma^{-1}(\omega) = G_{\mathrm{loc}\sigma}^{-1}(\omega) + \Sigma_\sigma(\omega), \tag{3.12}$$

or equivalently,

$$G_{\mathrm{imp}\sigma}(\omega) = G_{\mathrm{loc}\sigma}(\omega), \tag{3.13}$$

is fulfilled. At this point, the local self-energy in the original lattice model is identified with that in the effective impurity model,

$$\Sigma_\sigma(\omega) = \Sigma_{\mathrm{imp}\sigma}(\omega). \tag{3.14}$$

However, in the two-site dynamical mean field theory, such a consistency can no longer be satisfied exactly, since we have only a few tunable parameters, $\varepsilon_{c\sigma}$ and V_σ. Instead, we search their values in such a way that the *essential functional features* of the left-hand side is well reproduced by the right-hand side in Eq. (3.13).

The numerically evaluated self-energy is expanded in the *low*-frequency regime as

$$\Sigma_\sigma(\omega) = \Sigma_{\mathrm{imp}\sigma}(\omega) = a_\sigma + b_\sigma\omega + \mathcal{O}(\omega^2), \tag{3.15}$$

where the coefficient b_σ relates to the renormalization factor Z_σ via

$$Z_\sigma \equiv \left[1 - \left.\frac{d\Sigma_\sigma(\omega)}{d\omega}\right|_{\omega=0}\right]^{-1} = \frac{1}{1-b_\sigma}. \tag{3.16}$$

This factor Z_σ should be a positive number, if we assume that the quasiparticle is well-defined and has a positive mass.

Inserting the expansion (3.15) into $G_{\mathrm{loc}\sigma}(\omega)$ and $G_{\mathrm{imp}\sigma}(\omega)$, their coherent parts, *i.e.*, their low-frequency contributions, are evaluated as

$$G_{\mathrm{loc}\sigma}^{(\mathrm{coh})}(\omega) = \overline{\left[Z_\sigma^{-1}\omega - \delta\varepsilon_{\mathbf{k}} - \xi_\sigma\right]^{-1}} \tag{3.17}$$

$$G_{\mathrm{imp}\sigma}^{(\mathrm{coh})}(\omega) = \left[Z_\sigma^{-1}\omega - \xi_\sigma - \Delta_\sigma(\omega)\right]^{-1}, \tag{3.18}$$

with

$$\delta\varepsilon_{\mathbf{k}} = \varepsilon_{\mathbf{k}} - t_0 \tag{3.19}$$

$$\xi_\sigma = t_0 - \mu + a_\sigma. \tag{3.20}$$

Now, we come to the trickiest point in the two-site dynamical mean field theory. We consider the *high*-frequency expansion of these coherent parts,

$$\begin{aligned} G^{(\mathrm{coh})}_{\mathrm{loc}\sigma}(\omega) =& \frac{Z_\sigma}{\omega} + \frac{Z_\sigma^2}{\omega^2}\overline{(\delta\varepsilon_{\mathbf{k}} + \xi_\sigma)} + \frac{Z_\sigma^3}{\omega^3}\overline{(\delta\varepsilon_{\mathbf{k}} + \xi_\sigma)^2} + \mathcal{O}\left(\frac{1}{\omega^4}\right) \\ =& \frac{Z_\sigma}{\omega} + \frac{Z_\sigma^2}{\omega^2}\xi_\sigma + \frac{Z_\sigma^2}{\omega^3}\left(Z_\sigma\overline{(\delta\varepsilon_{\mathbf{k}})^2} + Z_\sigma\xi_\sigma^2\right) + \mathcal{O}\left(\frac{1}{\omega^4}\right) \qquad (3.21) \\ G^{(\mathrm{coh})}_{\mathrm{imp}\sigma}(\omega) =& \frac{Z_\sigma}{\omega} + \frac{Z_\sigma^2}{\omega^2}\xi_\sigma + \frac{Z_\sigma^2}{\omega^3}\left(V_\sigma^2 + Z_\sigma\xi_\sigma^2\right) + \mathcal{O}\left(\frac{1}{\omega^4}\right), \qquad (3.22) \end{aligned}$$

where we used $\overline{\delta\varepsilon_{\boldsymbol{k}}} = 0$ and $\Delta_\sigma(\omega) = \omega^{-1}V_\sigma^2 + \mathcal{O}(\omega^{-2})$. This *high*-frequency expansion might seem to be strange, but it succeeds in capturing the rough functional features of $G^{(\mathrm{coh})}_{\mathrm{loc}\sigma}(\omega)$ and $G^{(\mathrm{coh})}_{\mathrm{imp}\sigma}(\omega)$.

Comparing these two asymptotic expansions, we can derive the self-consistent condition for V_σ as

$$\begin{aligned} V_\sigma^2 &= Z_\sigma\overline{(\delta\varepsilon_{\mathbf{k}})^2} \\ &= Z_\sigma\int d\varepsilon\ (\varepsilon - t_0)^2\rho_0(\varepsilon). \end{aligned} \qquad (3.23)$$

On the other hand, we use the condition for the particle number,

$$n_{\mathrm{loc}\sigma} = n_{\mathrm{imp}\sigma}, \qquad (3.24)$$

to determine $\varepsilon_{\mathrm{a}\sigma}$, where the left- and right-hand sides are defined as

$$n_{\mathrm{loc}\sigma} \equiv -\frac{1}{\pi}\int_{-\infty}^{0} d\omega\ \mathrm{Im}G_{\mathrm{loc}\sigma}(\omega) \qquad (3.25)$$

$$n_{\mathrm{imp}\sigma} \equiv -\frac{1}{\pi}\int_{-\infty}^{0} d\omega\ \mathrm{Im}G_{\mathrm{imp}\sigma}(\omega). \qquad (3.26)$$

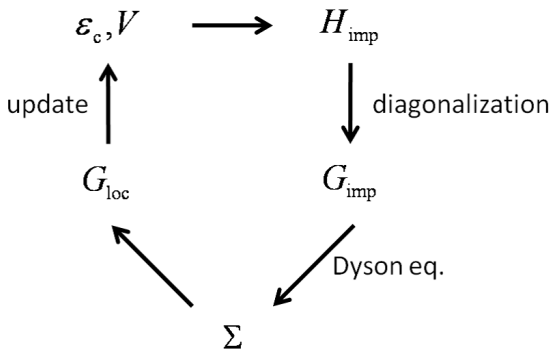

Figure 3.2: Flowchart of the two-site dynamical mean field theory.

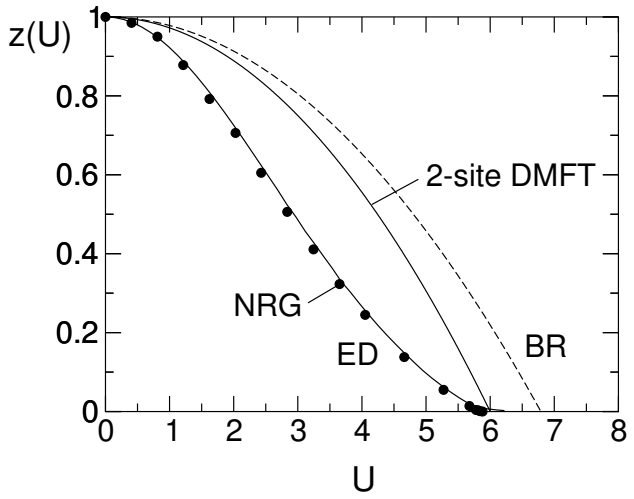

Figure 3.3: U-dependence of renormalization factor Z of the half-filled Hubbard model on the Bethe lattice at absolute zero temperature [142]. Solid and broken lines show the results by the two-site dynamical mean field theory (2-site DMFT) and Brinkman-Rice (BR) approximation [143], respectively. Filled circles and the line along them exhibit semi-exact results by dynamical mean field theory with numerical renormalization group (NRG) [88], and by that with exact diagonalization (ED) [136] solvers, respectively. The two-site dynamical mean field theory well reproduce the semi-exact critical value of U at the Mott transition.

These self-consistent conditions provide a new guess of parameters $\varepsilon_{\mathrm{a}\sigma}$ and V_σ from the initial guess. Iterating this calculation loop until these parameters converge, we finally obtain the self-consistent solutions. The flowchart of this algorithm is schematically drawn in Fig. 3.2.

In Fig. 3.3, we show the renormalization factor of the half-filled Hubbard model on the Bethe lattice at absolute zero temperature, which is calculated with the two-site dynamical mean field theory (2-site DMFT), together with those obtained by means of Brinkman-Rice (BR) approximation, the dynamical mean field theory combined with numerical renormalization group (NRG) solver, and that combined with exact diagonalization (ED) solver. All of these theories show the suppression of the renormalization factor, or equivalently, the enhancement of the quasi-particle mass, as the Coulomb interaction U is increased. The Mott transition is described as the vanishing of the renormalization factor, or the divergence of the quasi-particle mass. It is noteworthy that this critical value U_{c} evaluated by two-site DMFT is quite close to the *semi-exact* ones by the dynamical mean field theory with

NRG or ED solvers. We can also see that the renormalization factor in two-site DMFT is slightly larger than in the semi-exact ones. This is because two-site DMFT focuses only on the low-frequency regime and neglects the high-frequency features, *e.g.*, the Hubbard bands.

3.2 Linearized Cellular Dynamical Mean Field Theory

In the previous section, we briefly reviewed the two-site dynamical mean field theory, where the self-consistent condition is derived in such a way that the low-energy feature of the local Green's function is reproduced by the impurity one. At this point, we linearized the self-energy to evaluate the coherent part of the Green's functions. In the present section, we derive the linearized cellular dynamical mean field theory, which is a cluster extension of the two-site dynamical mean field theory, using the same linearization technique. Such an attempt has been made by E. C. Carter *et al.* [144], however, it was not sufficient to treat an effective medium. We improve it to

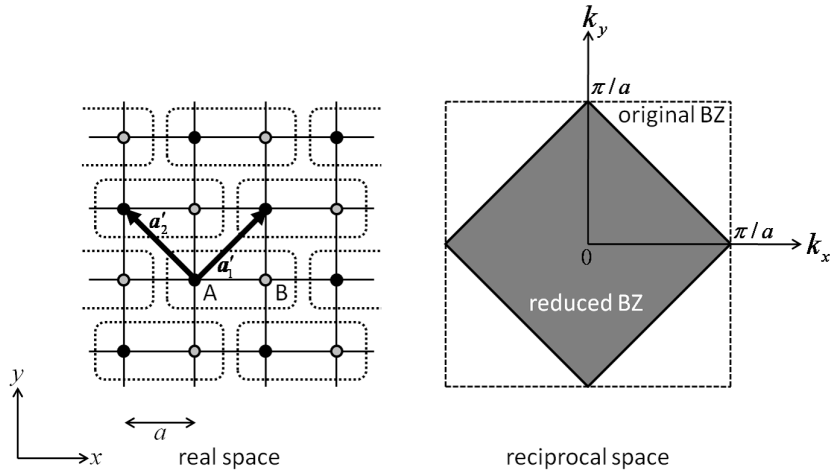

Figure 3.4: Two-dimensional square lattice regarded as an effective non-Bravais lattice with two sublattices (left), and corresponding reduction of Brillouin zone (right). In the left figure, the filled and shaded circles show the sublattices, and two arrows denotes the primitive translation vector for the effective non-Bravais lattice. In the right figure, the square enclosed by the broken line and the shaded one denote the original and reduced Brillouin zones, respectively.

systematically construct the linearized cellular dynamical mean field theory.

We use the sublattice representation introduced in the subsection 2.2.1, and rewrite the Hubbard Hamiltonian as

$$H = \sum_{i,j,\gamma,\delta,\sigma} t_{\gamma\delta}(i,j) c^{\dagger}_{i\gamma\sigma} c_{j\delta\sigma} - \mu \sum_{i,\gamma\sigma} c^{\dagger}_{i\gamma\sigma} c_{i\gamma\sigma} + U \sum_{i} n_{i\gamma\uparrow} n_{i\gamma\downarrow}, \tag{3.27}$$

where the original lattice is divided to $N_{\rm c}$ sublattices distinguished by the Greek indices $\gamma, \delta = 1, 2, \cdots, N_{\rm c}$, and $i, j = 1, 2, \cdots$ denote the indices for the sites in each sublattice. Two examples for the $N_{\rm c} = 2$ case are given in Fig. 3.4 and in Fig. 3.5. Following the spirit of the cluster dynamical mean field theory, we neglect the $\tilde{\mathbf{k}}$-dependence of the self-energy, and approximate the *cluster-local* lattice Green's function to

$$\hat{G}_{{\rm lat}\sigma}(\omega) = \hat{G}_{\sigma}(i, i:\omega) = \overline{\left[(\omega+\mu)\hat{1} - \hat{t}\left(\tilde{\mathbf{k}}\right) - \hat{\Sigma}_{\sigma}(\omega) \right]^{-1}}, \tag{3.28}$$

where we use the notation in the subsection 2.2.1, and the average for the $\tilde{\mathbf{k}}$-dependent quantity $O\left(\tilde{\mathbf{k}}\right)$ is taken as

$$\overline{O\left(\tilde{\mathbf{k}}\right)} = \frac{1}{N'} \sum_{\tilde{\mathbf{k}}} O\left(\tilde{\mathbf{k}}\right) \tag{3.29}$$

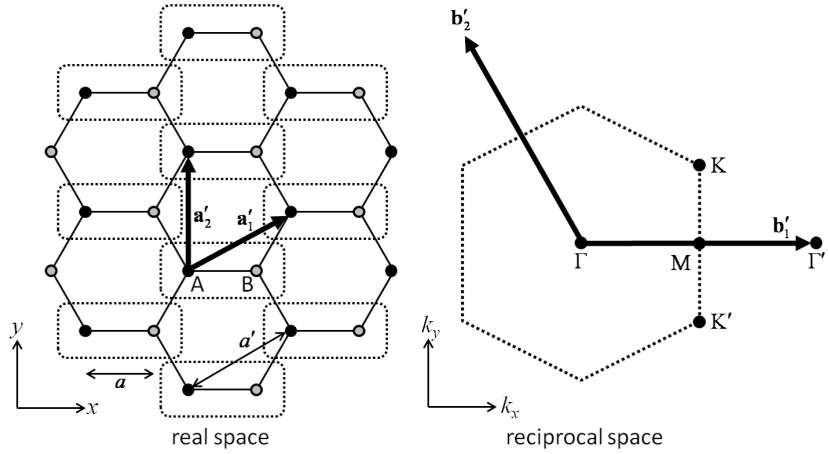

Figure 3.5: Two-dimensional honeycomb lattice (left), and its Brillouin zone (right). In the left figure, the primitive translation vectors, $\mathbf{a}'_1$ and $\mathbf{a}'_2$, are shown together with the lattice constants, $a, a' = \sqrt{3}\ a$. Two sublattices are presented by the filled and shaded circles, and the unit cells are enclosed by the broken lines. In the right figure, the primitive reciprocal vectors are denoted by $\mathbf{b}'_1$ and $\mathbf{b}'_2$. Some points with high symmetry, Γ, K, K′ and M points, are also shown in the Brillouin zone drawn with the broken line.

where $N' = N/N_{\rm c}$ denotes the number of $\tilde{\mathbf{k}}$-points, or equivalently, the number of the cluster cells.

In the linearized cellular dynamical mean field theory, the number of the bath sites is reduced to $N_{\rm c}$ in the effective cluster model. Then, its Hamiltonian reads

$$\begin{aligned} H_{\rm clu} = &\sum_{\gamma,\delta,\sigma} t_{0,\gamma\delta} c^\dagger_{\gamma\sigma} c_{\delta\sigma} - \mu \sum_{\gamma,\sigma} c^\dagger_{\gamma\sigma} c_{\gamma\sigma} + U \sum_{\gamma} n_{\gamma\uparrow} n_{\gamma\downarrow} \\ &+ \sum_{l,\sigma} \varepsilon_{l\sigma} a^\dagger_{l\sigma} a_{l\sigma} + \sum_{l,\gamma,\sigma} \Big[V_{l\gamma\sigma} a^\dagger_{l\sigma} c_{\gamma\sigma} + {\rm H.c.} \Big], \end{aligned} \tag{3.30}$$

with the bath index, $l = 1, 2, \cdots, N_{\rm c}$, and

$$t_{0,\gamma\delta} \equiv t_{\gamma\delta}(0,0) = \overline{t_{\gamma\delta}\left(\tilde{\mathbf{k}}\right)}. \tag{3.31}$$

Here, $c_{\gamma\sigma}$ and $n_{\gamma\sigma}$ are the abbreviations for $c_{0\gamma\sigma}$ and $n_{0\gamma\sigma}$, respectively. The energy levels of the bath sites $\varepsilon_{l\sigma}$ and the hybridization $V_{l\gamma\sigma}$ are treated as unknown parameters. Once an initial guess of these parameters is given, the medium Green's function, *i.e.*, the bare electron Green's function in the effective cluster model, is explicitly written in the matrix form as

$$\hat{\mathcal{G}}_\sigma(\omega) = \Big[(\omega + \mu)\hat{1} - \hat{t}_0 - \hat{\Delta}_\sigma(\omega) \Big]^{-1} \tag{3.32}$$

with

$$\hat{\Delta}_\sigma(\omega) = \hat{V}^\dagger_\sigma \hat{g}_{\rm a}(\omega) \hat{V}_\sigma, \quad g_{{\rm a},lm}(\omega) = \delta_{lm} (\omega - \omega_l)^{-1}. \tag{3.33}$$

We can also numerically evaluate the cluster Green's function, *i.e.*, the full electron Green's function in the effective cluster model. In fact, it is represented in the Lehmann-Kallen form as

$$\begin{aligned} G_{{\rm clu}\gamma\delta\sigma}(\omega) = &\sum_{m(\neq 0)} \frac{\langle 0 | c_{\gamma\sigma} | m \rangle \langle m | c^\dagger_{\delta\sigma} | 0 \rangle}{\omega + i0 - E_m + E_0} \\ &+ \sum_{m(\neq 0)} \frac{\langle 0 | c^\dagger_{\delta\sigma} | m \rangle \langle m | c_{\gamma\sigma} | 0 \rangle}{\omega + i0 - E_0 + E_m}, \end{aligned} \tag{3.34}$$

at absolute zero temperature, where E_m and $|m\rangle$ are the eigenpairs obtained via the numerical diagonalization of the Hamiltonian (3.30), and $m = 0$ denotes the ground state. Then, the cluster self-energy is simultaneously derived by means of the Dyson equation as

$$\begin{aligned} \hat{\Sigma}_{{\rm clu}\sigma}(\omega) &= \hat{\mathcal{G}}^{-1}_\sigma(\omega) - \hat{G}^{-1}_{{\rm clu}\sigma}(\omega) \\ &= (\omega + \mu)\hat{1} - \hat{t}_0 - \hat{\Delta}_\sigma(\omega) - \hat{G}^{-1}_{{\rm clu}\sigma}(\omega), \end{aligned} \tag{3.35}$$

which also implies

$$\hat{G}_{\mathrm{clu}\sigma}(\omega) = \left[(\omega+\mu)\hat{1} - \hat{t}_0 - \hat{\Sigma}_{\mathrm{clu}\sigma}(\omega) - \hat{\Delta}_\sigma(\omega)\right]^{-1}. \tag{3.36}$$

In the ideal cellular dynamical mean field theory, namely, that with an exact solver, the unknown parameters in the effective cluster model are determined with the self-consistent condition,

$$\hat{\mathcal{G}}_\sigma^{-1}(\omega) = \hat{G}_{\mathrm{lat}\sigma}^{-1}(\omega) + \hat{\Sigma}_\sigma(\omega), \tag{3.37}$$

or equivalently,

$$\hat{G}_{\mathrm{clu}\sigma}(\omega) = \hat{G}_{\mathrm{lat}\sigma}(\omega). \tag{3.38}$$

At this point, the cluster-local self-energy in the original lattice model is identified with that in the effective cluster model,

$$\hat{\Sigma}_\sigma(\omega) = \hat{\Sigma}_{\mathrm{clu}\sigma}(\omega). \tag{3.39}$$

However, in the linearized cellular dynamical mean field theory, such a consistency cannot be fulfilled exactly, because of the parameter shortage in the effective cluster model. Instead, we focus only on the low-energy contributions of the Green's functions, *i.e.*, their coherent parts $\hat{G}_{\mathrm{lat}\sigma}^{(\mathrm{coh})}(\omega)$ and $\hat{G}_{\mathrm{clu}\sigma}^{(\mathrm{coh})}(\omega)$. Then, we determine the parameters ε_l and $V_{l\gamma\sigma}$, in such a way that their essential features of the former is well reproduced by the latter.

In order to evaluate the coherent parts, the numerically computed cluster self-energy is linearly expanded as

$$\hat{\Sigma}_\sigma(\omega) = \hat{\Sigma}_{\mathrm{clu}\sigma}(\omega) = \hat{a}_\sigma + \hat{b}_\sigma\omega + \mathcal{O}(\omega^2). \tag{3.40}$$

The renormalization factor $\hat{Z}_\sigma$ is also obtained from $\hat{b}_\sigma$ as

$$\hat{Z}_\sigma = \left[\hat{1} - \left.\frac{d\hat{\Sigma}_\sigma}{d\omega}\right|_{\omega=0}\right]^{-1} = \left[\hat{1} - \hat{b}_\sigma\right]^{-1}. \tag{3.41}$$

Here, we assume that the matrix $\hat{Z}_\sigma$ is positive definite, which implies that the quasi-particles are well-defined and have positive masses.

Inserting the linear expansion of the self-energy into $\hat{G}_{\mathrm{lat}\sigma}(\omega)$ and $\hat{G}_{\mathrm{clu}\sigma}(\omega)$, we obtain their coherent parts as

$$\hat{G}_{\mathrm{lat}\sigma}^{(\mathrm{coh})}(\omega) = \overline{\left[\omega\hat{Z}_\sigma^{-1} - \delta\hat{t}\left(\tilde{\mathbf{k}}\right) - \hat{\xi}_\sigma\right]^{-1}} \tag{3.42}$$

$$\hat{G}_{\mathrm{clu}\sigma}^{(\mathrm{coh})}(\omega) = \left[\omega\hat{Z}_\sigma^{-1} - \hat{\xi}_\sigma - \hat{\Delta}_\sigma(\omega)\right]^{-1} \tag{3.43}$$

with

$$\hat{\xi}_\sigma = \hat{t}_0 - \mu\hat{1} + \hat{a}_\sigma, \tag{3.44}$$

$$\delta t\left(\tilde{\mathbf{k}}\right) = t\left(\tilde{\mathbf{k}}\right) - \hat{t}_0. \tag{3.45}$$

Their high-frequency expansions are

$$\begin{aligned}
\hat{G}^{(\mathrm{coh})}_{\mathrm{lat}\sigma}(\omega) &= \frac{1}{\omega}\hat{Z}_\sigma + \frac{1}{\omega^2}\overline{\hat{Z}_\sigma\left(\delta\hat{t}\left(\tilde{\mathbf{k}}\right) + \hat{\xi}_\sigma\right)\hat{Z}_\sigma} \\
&\quad + \frac{1}{\omega^3}\overline{\hat{Z}_\sigma\left(\delta\hat{t}\left(\tilde{\mathbf{k}}\right) + \hat{\xi}_\sigma\right)\hat{Z}_\sigma\left(\delta\hat{t}\left(\tilde{\mathbf{k}}\right) + \hat{\xi}_\sigma\right)\hat{Z}_\sigma} + \mathcal{O}\left(\frac{1}{\omega^4}\right) \\
&= \frac{1}{\omega}\hat{Z}_\sigma + \frac{1}{\omega^2}\hat{Z}_\sigma\hat{\xi}_\sigma\hat{Z}_\sigma \\
&\quad + \frac{1}{\omega^3}\hat{Z}_\sigma\left(\overline{\delta\hat{t}\left(\tilde{\mathbf{k}}\right)\hat{Z}_\sigma\delta\hat{t}\left(\tilde{\mathbf{k}}\right)} + \hat{\xi}_\sigma\hat{Z}_\sigma\hat{\xi}_\sigma\right)\hat{Z}_\sigma + \mathcal{O}\left(\frac{1}{\omega^4}\right), \qquad (3.46) \\
\hat{G}^{(\mathrm{coh})}_{\mathrm{clu}\sigma}(\omega) &= \frac{1}{\omega}\hat{Z}_\sigma + \frac{1}{\omega^2}\hat{Z}_\sigma\hat{\xi}_\sigma\hat{Z}_\sigma \\
&\quad + \frac{1}{\omega^3}\hat{Z}_\sigma\left(\hat{V}^\dagger_\sigma\hat{V}_\sigma + \hat{\xi}_\sigma\hat{Z}_\sigma\hat{\xi}_\sigma\right)\hat{Z}_\sigma + \mathcal{O}\left(\frac{1}{\omega^4}\right), \qquad (3.47)
\end{aligned}$$

where we use $\overline{\delta\hat{t}\left(\tilde{\mathbf{k}}\right)} = 0$ and $\hat{\Delta}(\omega) = \omega^{-1}\hat{V}^\dagger_\sigma\hat{V}_\sigma + \mathcal{O}(\omega^{-2})$.

Comparing these two expansions, we can derive the self-consistent condition for $\hat{V}_\sigma$ as

$$\hat{V}^\dagger_\sigma\hat{V}_\sigma = \overline{\delta\hat{t}\left(\tilde{\mathbf{k}}\right)\hat{Z}_\sigma\delta\hat{t}\left(\tilde{\mathbf{k}}\right)}. \tag{3.48}$$

Due to the positive definiteness of $\hat{Z}_\sigma$, the expectation value of the right-hand side operator becomes positive for any quantum states, which shows that it is also positive definite. Thus, we can numerically find a unitary matrix $\hat{U}$ and a diagonal real matrix $\hat{D}$ which fulfill

$$\overline{\delta\hat{t}\left(\tilde{\mathbf{k}}\right)\hat{Z}_\sigma\delta\hat{t}\left(\tilde{\mathbf{k}}\right)} = \hat{U}\hat{D}^2\hat{U}^\dagger. \tag{3.49}$$

Then, the hybridization matrix $\hat{V}_\sigma$ can be determined as

$$\hat{V}_\sigma = \hat{D}\hat{U}^\dagger. \tag{3.50}$$

On the other hand, the self-consistent conditions for $\varepsilon_{l\sigma}$ is undertaken by

$$n_{\mathrm{lat}\gamma\sigma} = n_{\mathrm{clu}\gamma\sigma}, \tag{3.51}$$

where the right- and left-hand sides are defined as

$$n_{\mathrm{lat}\gamma\sigma} = -\frac{1}{\pi}\int_{-\infty}^{0} d\omega\ \mathrm{Im}G_{\mathrm{lat}\gamma\gamma\sigma}(\omega) \tag{3.52}$$

$$n_{\mathrm{clu}\gamma\sigma} = -\frac{1}{\pi}\int_{-\infty}^{0} d\omega\ \mathrm{Im}G_{\mathrm{clu}\gamma\gamma\sigma}(\omega), \tag{3.53}$$

respectively. These self-consistent conditions can be used to renew the guess for the parameters $\varepsilon_{l\sigma}$ and $\hat{V}_\sigma$. Iterating this calculation loop until these parameters converge, we finally obtain the self-consistent solutions.

Now, let us consider the case of $N_{\mathrm{c}} = 2$, in more detail. For simplicity, we assume that the lattice system possesses an inversion symmetry whose center locates at the middle point between two sites in a unit cell. Then, the matrix $\delta\hat{t}\left(\tilde{\mathbf{k}}\right)$ has the form,

$$\delta\hat{t}\left(\tilde{\mathbf{k}}\right) = \begin{pmatrix} f_0\left(\tilde{\mathbf{k}}\right) & f_1\left(\tilde{\mathbf{k}}\right) - if_2\left(\tilde{\mathbf{k}}\right) \\ f_1\left(\tilde{\mathbf{k}}\right) + if_2\left(\tilde{\mathbf{k}}\right) & f_0\left(\tilde{\mathbf{k}}\right) \end{pmatrix} \tag{3.54}$$

where, $f_0\left(\tilde{\mathbf{k}}\right)$, $f_1\left(\tilde{\mathbf{k}}\right)$ and $f_2\left(\tilde{\mathbf{k}}\right)$ are real functions satisfying

$$f_0\left(-\tilde{\mathbf{k}}\right) = f_0\left(\tilde{\mathbf{k}}\right),\ f_1\left(-\tilde{\mathbf{k}}\right) = f_1\left(\tilde{\mathbf{k}}\right),\ f_2\left(-\tilde{\mathbf{k}}\right) = -f_2\left(\tilde{\mathbf{k}}\right). \tag{3.55}$$

If spontaneous breaking of the inversion symmetry is absent, two sites in the unit cell are physically equivalent, which implies

$$G_{\mathrm{lat/clu}11\sigma}(\omega) = G_{\mathrm{lat/clu}22\sigma}(\omega), \quad G_{\mathrm{lat/clu}12\sigma}(\omega) = G_{\mathrm{lat/clu}21\sigma}(\omega). \tag{3.56}$$

Thus, $\hat{G}_{\mathrm{lat/clu}\sigma}(\omega)$ and $\hat{\Sigma}_\sigma(\omega)$ can be diagonalized as

$$\begin{pmatrix} \tilde{G}_{\mathrm{lat/clu},1,\sigma}(\omega) & 0 \\ 0 & \tilde{G}_{\mathrm{lat/clu},2,\sigma}(\omega) \end{pmatrix} = \hat{U}^\dagger \hat{G}_{\mathrm{lat/clu}\sigma}(\omega)\hat{U} \tag{3.57}$$

with

$$\hat{U} \equiv \frac{1}{\sqrt{2}}\begin{pmatrix} 1 & -1 \\ 1 & 1 \end{pmatrix}, \tag{3.58}$$

and

$$\tilde{G}_{\mathrm{lat/clu},1,\sigma}(\omega) = G_{\mathrm{lat/clu},11,\sigma}(\omega) + G_{\mathrm{lat/clu},12,\sigma}(\omega) \tag{3.59}$$

$$\tilde{G}_{\mathrm{lat/clu},2,\sigma}(\omega) = G_{\mathrm{lat/clu},11,\sigma}(\omega) - G_{\mathrm{lat/clu},12,\sigma}(\omega). \tag{3.60}$$

Since the matrices $\hat{Z}_\sigma$, $\hat{V}_\sigma^\dagger \hat{V}_\sigma$ and $\overline{\delta\hat{t}\left(\tilde{\mathbf{k}}\right)\hat{Z}_\sigma\delta\hat{t}\left(\tilde{\mathbf{k}}\right)}$ are derived from the Green's functions, they also should be diagonalized with the same unitary matrix $\hat{U}$. In other words, the unitary matrix $\hat{U}$ in Eq. (3.49) and (3.50) are given by Eq. (3.58), and we can define $\tilde{Z}_{1\sigma}$, $\tilde{Z}_{2\sigma}$, $\tilde{V}_{1\sigma}^2$ and $\tilde{V}_{2\sigma}^2$ via

$$\begin{pmatrix} \tilde{Z}_{1\sigma} & 0 \\ 0 & \tilde{Z}_{2\sigma} \end{pmatrix} = U^\dagger \hat{Z}_\sigma U, \quad \begin{pmatrix} \tilde{V}_{1\sigma}^2 & 0 \\ 0 & \tilde{V}_{2\sigma}^2 \end{pmatrix} = U^\dagger V_\sigma^\dagger V_\sigma U. \tag{3.61}$$

Physically, the unitary transformation (3.57) corresponds to the canonical transformation,

$$\begin{pmatrix} \tilde{c}_{1\sigma} \\ \tilde{c}_{2\sigma} \end{pmatrix} \equiv \hat{U}^\dagger \begin{pmatrix} c_{1\sigma} \\ c_{2\sigma} \end{pmatrix}, \tag{3.62}$$

where $\tilde{c}_{1\sigma}$ and $\tilde{c}_{2\sigma}$ annihilates a σ-spin electron occupying the bonding and anti-bonding molecular orbitals, respectively. It is convenient to rewrite the effective cluster model (3.30) in terms of $\tilde{c}_{\gamma\sigma}$ and $\tilde{c}_{\gamma\sigma}^\dagger$:

$$\begin{aligned} \tilde{H}_{\mathrm{clu}} = & \sum_{\gamma,\sigma} \tilde{t}_{0,\gamma} \tilde{c}_{\gamma\sigma}^\dagger \tilde{c}_{\gamma\sigma} - \mu \sum_{\gamma,\sigma} \tilde{c}_{\gamma\sigma}^\dagger \tilde{c}_{\gamma\sigma} + \frac{U}{2} \sum_{\gamma\delta} \tilde{n}_{\gamma\uparrow} \tilde{n}_{\delta\downarrow} \\ & + \frac{U}{2} \left(\tilde{c}_{1\uparrow}^\dagger \tilde{c}_{2\uparrow} \tilde{c}_{1\downarrow}^\dagger \tilde{c}_{2\downarrow} + \tilde{c}_{1\uparrow}^\dagger \tilde{c}_{2\uparrow} \tilde{c}_{2\downarrow}^\dagger \tilde{c}_{1\downarrow} + \mathrm{H.c.} \right) \\ & + \sum_{l,\sigma} \varepsilon_{l\sigma} a_{l\sigma}^\dagger a_{l\sigma} + \sum_{\gamma,\sigma} \left(\tilde{V}_{\gamma\sigma} a_{\gamma\sigma}^\dagger \tilde{c}_{\gamma\sigma} + \mathrm{H.c.} \right), \end{aligned} \tag{3.63}$$

where $\tilde{t}_{0,\gamma}$ is defined via

$$\begin{pmatrix} \tilde{t}_{0,1} & 0 \\ 0 & \tilde{t}_{0,2} \end{pmatrix} = U^\dagger \hat{t}_0 U = \begin{pmatrix} t_{0,11} + t_{0,12} & 0 \\ 0 & t_{0,11} - t_{0,12} \end{pmatrix}. \tag{3.64}$$

In this molecular orbital representation, the bonding and anti-bonding orbitals are coupled only to the first and second baths, respectively, as shown in Fig. 3.6. It is noteworthy that we can directly evaluate $\tilde{Z}_{\gamma\sigma}$ from $\tilde{H}_{\mathrm{clu}}$ as

$$\tilde{Z}_{\gamma\sigma} = \left[1 - \left. \frac{d\tilde{\Sigma}_{\mathrm{clu}\gamma\sigma}}{d\omega} \right|_{\omega=0} \right]^{-1} \tag{3.65}$$

with

$$\tilde{\Sigma}_{\mathrm{clu}\gamma\sigma}(\omega) = (\omega + \mu) - \tilde{t}_{0\gamma} - \frac{\tilde{V}_{\gamma\sigma}^2}{\omega - \varepsilon_{\gamma\sigma}} - \tilde{G}_{\mathrm{clu}\gamma\sigma}(\omega) \tag{3.66}$$

$$\tilde{G}_{\mathrm{clu}\gamma\sigma}(\omega) = \sum_{m(\neq 0)} \frac{\left| \langle m | \tilde{c}_{\gamma\sigma}^\dagger | 0 \rangle \right|^2}{\omega + i0 - E_m + E_0} + \sum_{m(\neq 0)} \frac{\left| \langle m | \tilde{c}_{\gamma\sigma} | 0 \rangle \right|^2}{\omega + i0 - E_0 + E_m}, \tag{3.67}$$

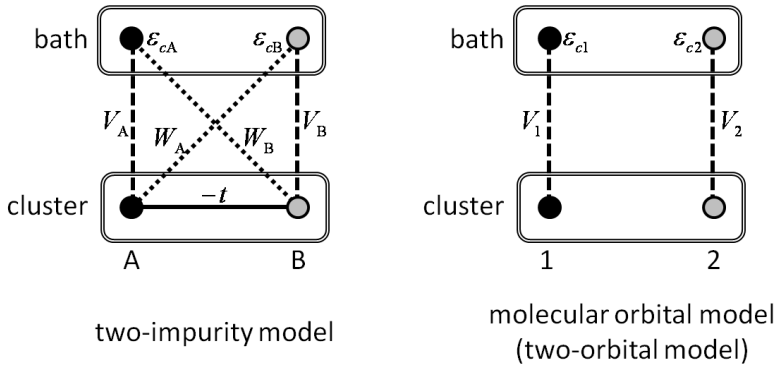

Figure 3.6: Original cluster model (left) and its molecular orbital representation (right).

where the eigenpairs E_m and $|m\rangle$ are calculated with the numerical diagonalization of $\tilde{H}_{\mathrm{clu}}$.

The self-consistent condition (3.48) can be rewritten for $\tilde{V}_{\gamma\sigma}$ as

$$\tilde{V}_{1\sigma}^2 = \tilde{Z}_{1\sigma}\overline{\left(f_0\left(\tilde{\mathbf{k}}\right)+f_1\left(\tilde{\mathbf{k}}\right)\right)^2}+\tilde{Z}_{2\sigma}\overline{\left(f_2\left(\tilde{\mathbf{k}}\right)\right)^2} \tag{3.68}$$

$$\tilde{V}_{2\sigma}^2 = \tilde{Z}_{2\sigma}\overline{\left(f_0\left(\tilde{\mathbf{k}}\right)+f_1\left(\tilde{\mathbf{k}}\right)\right)^2}+\tilde{Z}_{1\sigma}\overline{\left(f_2\left(\tilde{\mathbf{k}}\right)\right)^2}, \tag{3.69}$$

where the right-hand side is derived as

$$\begin{aligned}
&U^\dagger\overline{\delta\hat{t}\left(\tilde{\mathbf{k}}\right)\hat{Z}_\sigma\delta\hat{t}\left(\tilde{\mathbf{k}}\right)}U \\
&=\overline{U^\dagger\delta\hat{t}\left(\tilde{\mathbf{k}}\right)UU^\dagger\hat{Z}_\sigma U^\dagger\delta\hat{t}\left(\tilde{\mathbf{k}}\right)U} \\
&=\begin{pmatrix}
\tilde{Z}_{1\sigma}\overline{\left(f_0\left(\tilde{\mathbf{k}}\right)+f_1\left(\tilde{\mathbf{k}}\right)\right)^2}+\tilde{Z}_{2\sigma}\overline{\left(f_2\left(\tilde{\mathbf{k}}\right)\right)^2} & 0 \\
0 & \tilde{Z}_{2\sigma}\overline{\left(f_0\left(\tilde{\mathbf{k}}\right)+f_1\left(\tilde{\mathbf{k}}\right)\right)^2}+\tilde{Z}_{1\sigma}\overline{\left(f_2\left(\tilde{\mathbf{k}}\right)\right)^2}
\end{pmatrix}.
\end{aligned} \tag{3.70}$$

The other condition (3.51) for $\varepsilon_{l\sigma}$ is also given in terms of $\tilde{G}_{\mathrm{lat/clu}\gamma\sigma}(\omega)$ as

$$\tilde{n}_{\mathrm{lat}\gamma\sigma} = \tilde{n}_{\mathrm{clu}\gamma\sigma} \quad (\gamma = 1, 2), \tag{3.71}$$

with

$$\tilde{n}_{\mathrm{lat}\gamma\sigma} = -\frac{1}{\pi}\int_{-\infty}^{0} d\omega\ \mathrm{Im}\tilde{G}_{\mathrm{lat}\gamma\sigma}(\omega) \tag{3.72}$$

$$\tilde{n}_{\mathrm{clu}\gamma\sigma} = -\frac{1}{\pi}\int_{-\infty}^{0} d\omega\ \mathrm{Im}\tilde{G}_{\mathrm{clu}\gamma\sigma}(\omega). \tag{3.73}$$

3.3 Linearized Dynamical Cluster Approximation

The linearized cellular dynamical mean field theory can be regarded as the fusion of the two-site dynamical mean field theory and the cellular dynamical mean field theory. In the present section, the linearized dynamical cluster approximation is derived, which is another cluster extension of the two-site dynamical mean field theory based on the dynamical cluster approximation.

In subsection 2.2.2, we pointed out that the difference between the cellular dynamical mean field theory and the dynamical cluster approximation arises only from the boundary condition applied to the cluster. Actually, the open and periodic boundary conditions is used in the cellular dynamical mean field theory and the dynamical cluster approximation, respectively. From this viewpoint, we can convert the cellular dynamical mean field theory to the dynamical cluster approximation only by substituting $\tilde{t}\left(\tilde{\mathbf{k}}\right)$ with

$$\begin{aligned}\varepsilon_{\gamma\delta}\left(\tilde{\mathbf{k}}\right) &= \frac{1}{N'}\sum_{i,j} e^{-i(\tilde{\mathbf{r}}_i+\mathbf{R}_\gamma-\tilde{\mathbf{r}}_j-\mathbf{R}_\delta)} t_{\gamma\delta}(i,j) \\ &= e^{-i\tilde{\mathbf{k}}\cdot(\mathbf{R}_\gamma-\mathbf{R}_\delta)} t_{\gamma\delta}\left(\tilde{\mathbf{k}}\right),\end{aligned} \tag{3.74}$$

where we employ the notation used in subsection 2.2.2. Then, the cluster-local lattice Green's function is given as

$$\hat{G}_{\mathrm{lat}\sigma}(\omega) = \overline{\left[(\omega+\mu)\hat{1} - \hat{\varepsilon}\left(\tilde{\mathbf{k}}\right) - \hat{\Sigma}_\sigma(\omega)\right]^{-1}}, \tag{3.75}$$

with the $\tilde{\mathbf{k}}$-independent self-energy, where the $\tilde{\mathbf{k}}$-average is taken as Eq. (3.29).

The effective cluster model used in the linearized dynamical cluster approximation is written as

$$\begin{aligned}H_{\mathrm{clu}} = &\sum_{\gamma,\delta,\sigma} \varepsilon_{0\gamma\delta} c^\dagger_{\gamma\sigma} c_{\delta\sigma} - \mu\sum_{\gamma,\sigma} c^\dagger_{\gamma\sigma} c_{\gamma\sigma} + U\sum_{\gamma} n_{\gamma\uparrow} n_{\gamma\downarrow} \\ &+ \sum_{l,\sigma} \varepsilon_{l\sigma} a^\dagger_{l\sigma} a_{l\sigma} + \sum_{l,\gamma,\sigma}\left[V_{l\gamma\sigma} a^\dagger_{l\sigma} c_{\gamma\sigma} + \mathrm{H.c.}\right],\end{aligned} \tag{3.76}$$

with $l = 1, 2, \cdots, N_{\rm c}$ and $\varepsilon_{0\gamma\delta} = \overline{\varepsilon_{\gamma\delta}\left(\tilde{\mathbf{k}}\right)}$. From an initial guess of the unknown parameters, $\varepsilon_{l\sigma}$ and $V_{l\gamma\sigma}$, we compute the cluster Green's function, $\hat{G}_{{\rm clu}\sigma}(\omega)$, by digonalizing this Hamiltonian and using Lehmann-Kallen representation (3.34). We also obtain the cluster self-energy as

$$\hat{\Sigma}_{{\rm clu}\sigma}(\omega) = (\omega + \mu)\hat{1} - \hat{\varepsilon}_0 - \hat{\Delta}_\sigma(\omega) - \hat{G}^{-1}_{{\rm clu}\sigma}(\omega), \tag{3.77}$$

which is identified with $\Sigma_\sigma(\omega)$. Then, the renormalization factor $\hat{Z}_\sigma$ is computed with Eq. (3.41).

The self-consistent condition for $\hat{V}_\sigma$ is rewritten as

$$\hat{V}^\dagger_\sigma \hat{V}_\sigma = \overline{\delta\hat{\varepsilon}\left(\tilde{\mathbf{k}}\right)\hat{Z}_\sigma \delta\hat{\varepsilon}\left(\tilde{\mathbf{k}}\right)}, \tag{3.78}$$

with

$$\delta\hat{\varepsilon}\left(\tilde{\mathbf{k}}\right) = \hat{\varepsilon}\left(\tilde{\mathbf{k}}\right) - \hat{\varepsilon}_0, \tag{3.79}$$

and those for ε_l are undertaken by Eq. (3.51). Using these conditions in order to renew the guess for the parameters $\hat{V}_\sigma$ and ε_l, we finally obtain the self-consistent solution in an iterative way.

Chapter 4

Mott Transition in Hubbard Model on Square Lattice

In the previous chapter, we have proposed novel linearized theories of the cluster dynamical mean field theory. One is the linearized version of the cellular dynamical mean field theory and the other is that of the dynamical cluster approximation. These methods are on the basis of the cluster dynamical mean field theory combined with the exact diagonalization and describe low energy physics by means of the linearization of the self-energy. Because the linearized cluster dynamical mean field theories are not perturbative methods, in principle, they are applicable to any parameter regions from weak to strong coupling regime. Furthermore, these methods need the least number of effective bath sites so that necessary CPU time and memory are much less than the cluster dynamical mean field theory combined with the exact diagonalization.

In this chapter, we first apply the linearized cellular dynamical mean field theory and dynamical cluster approximation to the Hubbard model on the square lattice at half-filling and examine the validity of these methods. Comparing our results of the linearized methods with those of the ideal cellular dynamical mean field theory and dynamical cluster approximation, *i.e.* the cellular dynamical mean field theory and dynamical cluster approximation combined with the quantum Monte Carlo and numerical renormalization group method, we demonstrate that the Mott transition points obtained by the linearized schemes are in good agreement with those of the ideal cellular dynamical mean field theory and dynamical cluster approximation. We also compare our results with numerically exact results such as large-site quantum Monte Carlo results and we find that the linearized dynamical cluster approximation provides qualitatively good results.

Next, we study the Mott transition with geometrical frustration by con-

sidering the next-nearest neighbor hopping. As frustration is increased, we show that the critical interaction strength becomes large and geometrical frustration stabilizes the metallic phase, which are consistent with previous results. Furthermore, our results of linearized dynamical cluster approximation qualitatively reproduce those of the path integral renormalization group method, although our scheme is highly simplified one.

4.1 Model and Method

Hubbard model: We now consider the Hubbard Hamiltonian on the square lattice with the nearest and next-nearest neighbor hopping integrals,

$$H = -t \sum_{\langle i,j\rangle,\sigma} -t' \sum_{(i,j),\sigma} c^\dagger_{i\sigma} c_{j\sigma} - \mu \sum_{i,\sigma} c^\dagger_{i\sigma} c_{i\sigma} + U \sum_i n_{i\uparrow} n_{i\downarrow}. \tag{4.1}$$

Here, the summation over $\langle i,j\rangle$ is taken between the nearest-neighbor pair of sites and (i,j) denotes the next-nearest-neighbor pair of sites. The system corresponds to the unfrustrated square lattice at $t'/t = 0$, and frustration becomes stronger with increasing t'/t. In the following, we consider the *paramagnetic* phase without any long-range order.

Linearized cellular dynamical mean field theory: Applying the two-site cluster linearized cellular dynamical mean field theory to this model, we obtain the effective Hamiltonian on the molecular-orbital basis,

$$\begin{aligned}\tilde{H}_{\rm clu} = & \, t \sum_{l,\sigma} (-1)^l \tilde{c}^\dagger_{l\sigma} \tilde{c}_{l\sigma} - \mu \sum_{l,\sigma} \tilde{c}^\dagger_{l\sigma} \tilde{c}_{l\sigma} + \frac{U}{2} \sum_{l,l'} \tilde{n}_{l\uparrow} \tilde{n}_{l'\downarrow} \\ & + \frac{U}{2} \left(\tilde{c}^\dagger_{1\uparrow} \tilde{c}_{2\uparrow} \tilde{c}^\dagger_{1\downarrow} \tilde{c}_{2\downarrow} + \tilde{c}^\dagger_{1\uparrow} \tilde{c}_{2\uparrow} \tilde{c}^\dagger_{2\downarrow} \tilde{c}_{1\downarrow} + \text{H.c.} \right) \\ & + \sum_{l,\sigma} \varepsilon_l a^\dagger_{l\sigma} a_{l\sigma} + \sum_{l,\sigma} \left(\tilde{V}_l a^\dagger_{l\sigma} \tilde{c}_{l\sigma} + \text{H.c.} \right), \end{aligned} \tag{4.2}$$

where, ε_l and V_l $(l = 1, 2)$ are the effective bath parameters. The index $l = 1$ $(l = 2)$ denotes the bonding (anti-bonding) orbital. Given the bath parameters, we exactly diagonalize the Hamiltonian and obtain the eigenpairs E_m and $|m\rangle$. We then calculate the Green's function using the Lehmann-Kallen representation,

$$G_{\rm clul}(\omega) = \sum_{m(\neq 0)} \frac{\langle 0|\tilde{c}_{l\sigma}|m\rangle\langle m|\tilde{c}^\dagger_{l\sigma}|0\rangle}{\omega + i0 - E_m + E_0} + \sum_{m(\neq 0)} \frac{\langle 0|\tilde{c}^\dagger_{l\sigma}|m\rangle\langle m|\tilde{c}_{l\sigma}|0\rangle}{\omega + i0 - E_0 + E_m}. \tag{4.3}$$

The self-energy $\Sigma_l(\omega)$ is extracted by the Dyson equation, $\Sigma_l(\omega) = 1/\mathcal{G}_l(\omega) - 1/G_l(\omega)$ and the renormalization factor $Z_l = [1 - \partial\Sigma_l(\omega)/\partial\omega|_{\omega=0}]^{-1}$ is computed by the numerical differentiation. The particle number in the effective cluster Hamiltonian $n_{\mathrm{clu}l}$ is also computed. On the other hand, the Green's function in the lattice system is obtained on the molecular-orbital basis,

$$\begin{aligned}
\tilde{G}_{\mathrm{lat}1}\left(\tilde{\mathbf{k}},\omega\right) &= \left[\omega + i0 + \mu - \Sigma_2(\omega) - \left\{f_0\left(\tilde{\mathbf{k}}\right) + f_1\left(\tilde{\mathbf{k}}\right)\right\}\right]/D\left(\tilde{\mathbf{k}},\omega\right), \\
\tilde{G}_{\mathrm{lat}2}\left(\tilde{\mathbf{k}},\omega\right) &= \left[\omega + i0 + \mu - \Sigma_1(\omega) - \left\{f_0\left(\tilde{\mathbf{k}}\right) + f_1\left(\tilde{\mathbf{k}}\right)\right\}\right]/D\left(\tilde{\mathbf{k}},\omega\right), \\
D\left(\tilde{\mathbf{k}},\omega\right) &= \left[\omega + i0 + \mu - \Sigma_1(\omega) - \left\{f_0\left(\tilde{\mathbf{k}}\right) + f_1\left(\tilde{\mathbf{k}}\right)\right\}\right] \\
&\quad \times \left[\omega + i0 + \mu - \Sigma_2(\omega) + \left\{f_0\left(\tilde{\mathbf{k}}\right) + f_1\left(\tilde{\mathbf{k}}\right)\right\}\right] - f_2\left(\tilde{\mathbf{k}}\right)^2.
\end{aligned} \tag{4.4}$$

The particle number in the lattice system $n_{\mathrm{lat}l}$ is computed by

$$\tilde{n}_{\mathrm{lat}l} = -\frac{1}{\pi}\int_{-\infty}^{0} d\omega\ \mathrm{Im}\overline{\tilde{G}_{\mathrm{lat}l}\left(\tilde{\mathbf{k}},\omega\right)}. \tag{4.5}$$

By linearization of the self-energy, the self-consistent equations is obtained as,

$$\tilde{V}_{1\sigma}^2 = \tilde{Z}_{1\sigma}\overline{\left(f_0\left(\tilde{\mathbf{k}}\right) + f_1\left(\tilde{\mathbf{k}}\right)\right)^2} + \tilde{Z}_{2\sigma}\overline{\left(f_2\left(\tilde{\mathbf{k}}\right)\right)^2}, \tag{4.6}$$

$$\tilde{V}_{2\sigma}^2 = \tilde{Z}_{2\sigma}\overline{\left(f_0\left(\tilde{\mathbf{k}}\right) + f_1\left(\tilde{\mathbf{k}}\right)\right)^2} + \tilde{Z}_{1\sigma}\overline{\left(f_2\left(\tilde{\mathbf{k}}\right)\right)^2}, \tag{4.7}$$

$$\tilde{n}_{\mathrm{lat}l\sigma} = \tilde{n}_{\mathrm{clu}l\sigma} \quad (l = 1, 2). \tag{4.8}$$

The coefficients $\overline{\left(f_0\left(\tilde{\mathbf{k}}\right) + f_1\left(\tilde{\mathbf{k}}\right)\right)^2}$ and $\overline{\left(f_2\left(\tilde{\mathbf{k}}\right)\right)^2}$ in the above equations are numerically computed. For $t'/t = 0$, $\overline{\left(f_0\left(\tilde{\mathbf{k}}\right) + f_1\left(\tilde{\mathbf{k}}\right)\right)^2} = \overline{\left(f_2\left(\tilde{\mathbf{k}}\right)\right)^2} = 1.5t^2$.

Linearized dynamical cluster approximation: As mentioned in the section 3.3, the linearized dynamical cluster approximation is obtained by sustituting $\tilde{t}\left(\tilde{\mathbf{k}}\right)$ with $\varepsilon\left(\tilde{\mathbf{k}}\right)$ via Eq. (3.74). Therefore, we should only rewrite the

effective Hamiltonian on the molecular-orbital basis,

$$\begin{aligned}\tilde{H}_{\rm clu} &= \varepsilon_0 \sum_{l,\sigma} (-1)^l \tilde{c}^\dagger_{l\sigma} \tilde{c}_{l\sigma} - \mu \sum_{l,\sigma} \tilde{c}^\dagger_{l\sigma} \tilde{c}_{l\sigma} + \frac{U}{2} \sum_{l,l'} \tilde{n}_{l\uparrow} \tilde{n}_{l'\downarrow} \\ &+ \frac{U}{2} \left(\tilde{c}^\dagger_{1\uparrow} \tilde{c}_{2\uparrow} \tilde{c}^\dagger_{1\downarrow} \tilde{c}_{2\downarrow} + \tilde{c}^\dagger_{1\uparrow} \tilde{c}_{2\uparrow} \tilde{c}^\dagger_{2\downarrow} \tilde{c}_{1\downarrow} + \text{H.c.} \right) \\ &+ \sum_{l,\sigma} \varepsilon_l a^\dagger_{l\sigma} a_{l\sigma} + \sum_{l,\sigma} \left(\tilde{V}_l a^\dagger_{l\sigma} \tilde{c}_{l\sigma} + \text{H.c.} \right), \end{aligned} \tag{4.9}$$

with $\varepsilon_0 = 0.4053t$, and the coefficients $\overline{\left(f_0\left(\tilde{\mathbf{k}}\right) + f_1\left(\tilde{\mathbf{k}}\right)\right)^2} = 1.379t^2$ and $\overline{\left(f_2\left(\tilde{\mathbf{k}}\right)\right)^2} = 0$ in Eqs. (4.6) and (4.7). In the effective Hamiltonian (4.9), the molecular orbital $l = 1$ ($l = 2$) corresponds to the cluster momentum $\mathbf{K}_\Gamma$ ($\mathbf{K}_{\rm M}$) mode. Notice that the linearized dynamical cluster approximation for the square lattice system can directly calculate the Green's function $\overline{\tilde{G}_{{\rm lat}l}\left(\tilde{\mathbf{k}}, \omega\right)}$ without summation over $\tilde{\mathbf{k}}$ of $\tilde{G}_{{\rm lat}l}\left(\tilde{\mathbf{k}}, \omega\right)$ because it is the Bravais lattice. Accordingly, we can simply compute $\overline{\tilde{G}_{{\rm lat}l}\left(\tilde{\mathbf{k}}, \omega\right)}$ as follows;

$$\overline{\tilde{G}_{{\rm lat}l}\left(\tilde{\mathbf{k}}, \omega\right)} = \int d\varepsilon \frac{\rho_{0,l}(\varepsilon)}{\omega + \mu - \varepsilon - \Sigma_l(\omega)}, \tag{4.10}$$

with

$$\rho_{0,l}(\varepsilon) = \overline{\delta(\varepsilon - \varepsilon_{\mathbf{K}_l + \tilde{\mathbf{k}}})}, \tag{4.11}$$

where, $\mathbf{K}_{1/2}$ denotes $\mathbf{K}_{\Gamma/{\rm M}}$.

4.2 Mott Transition in Hubbard Model on Square Lattice

In this section, we apply the linearized cellular dynamical mean field theory and dynamical cluster approximation to the Hubbard model at half-filling on the square lattice and examine the validity of the linearized schemes. We study the Mott transition and show that the linearized cellular dynamical mean field theory and dynamical cluster approximation give qualitatively good results in the weak to intermediate coupling regime.

The Hubbard model on the square lattice has been studied intensively and extensively because it is believed to capture the essential physics of the

strongly correlated electron systems, *e.g.* high-T_c superconductivity, magnetism, metal-insulator transition, etc [131, 145–156]. In particular, with respect to the metal-insulator transition in this model at zero temperature, there are two conflicting opinions. The first opinion explains that the antiferromagnetic order due to the purely local correlations is the origin of the metal-insulator transition in the Hubbard model on the square lattice [152–154]. It is well-known that the zero-temperature antiferromagnetic transition point in the square lattice Hubbard model at half-filling is the infinitesimal interaction due to the perfect nesting. In other words, in this opinion, the antiferromagnetic transition point can be different from the pure Mott transition point. The antiferromagnetic transition occurs at infinitesimal U but the pure Mott transition in the *paramagnetic* solution occurs at finite U. On the other hand, the second opinion argues that the Mott insulating gap is present for all $U > 0$, even if the long-range order is not considered, due to the non-local *fluctuations* as in one-dimensional systems and there is no adiabatic continuity between non-interacting and interacting eigenstates, which breaks down the perturbation theory [155]. This problem has stood for a long time.

There are a lot of theories which describe the Mott transition in the Hubbard model. There are analytical methods such as the coherent potential approximation, Gutzwiller approximation, slave-boson mean field theory, etc., which are essentially included in the dynamical mean field theory. Numerical methods are the exact diagonalization for small-site cluster, the quantum Monte Carlo simulation, variational Monte Carlo, cellular dynamical mean field theory, dynamical cluster approximation, etc. Each method describes the Mott transition in the *paramagnetic* phase of the square lattice Hubbard model but gives different results. The essential difference is whether there is the finite critical interaction strength U_c at zero temperature or not. In the dynamical mean field theory, the Mott transition is induced by the local correlations and the transition point U_c is of the order of the band-width. The variational Monte Carlo method including the Gutzwiller and doublon-holon factor as a variational parameter also gives finite U_c. Although the value of U_c is decreased as the cluster size is enlarged, the cellular dynamical mean field theory gives finite U_c. These theories correspond to the first opinion above mentioned. On the other hand, the quantum Monte Carlo simulation shows no evidence of the finite-U Mott transition, *i.e.* the system is insulating for all $U > 0$. In the Hubbard model at half-filling on the square lattice, there is no minus sign problem so that the quantum Monte Carlo works well at low temperatures. Also in the exact diagonalization calculations, the tendency of the Mott transition has not been observed on the perfect square lattice. These results correspond to the second picture for the metal-insulator tran-

sition. Recently, S. Moukouri *et al.* [131] and T. D. Stanescu *et al.* [150] have independently addressed this problem by using the dynamical cluster approximation and the dynamical Green function approach, respectively. In these studies, the *paramagnetic* Mott transition point is the infinitesimal U. They argue that the insulating state is induced by non-local correlations and the perturbation theory cannot describe the *paramagnetic* insulating phase.

As above mentioned, approximate theories tend to provide the first picture and numerical simulations provide the second one. So, the second opinion is expected to be correct but a simplified theory which describes the second picture has not been established so far. Hence, it is desirable to establish the approximate method which does not need heavy numerical computations

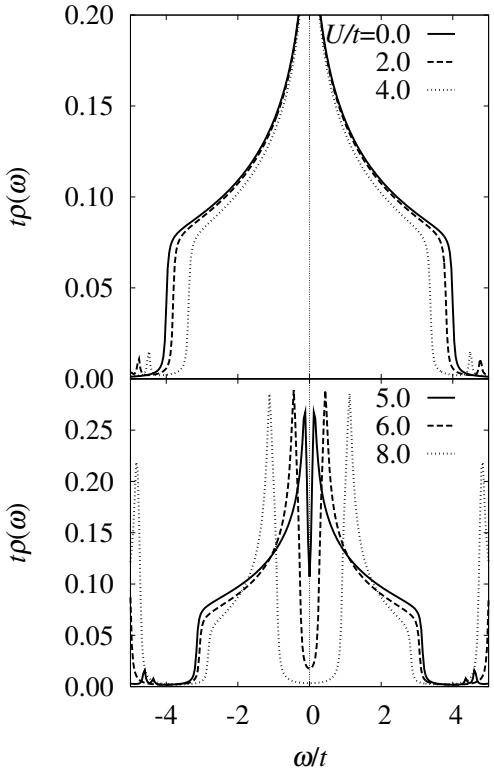

Figure 4.1: Density of states $\rho(\omega)$ for several U obtained by the linearized cellular dynamical mean field theory. In the upper panel, the density of states for $U/t = 0.0, 2.0, 4.0$ is shown. We can see the quasi-particle peak at the Fermi level ($\omega = 0$) sharper as U increases. In the lower panel, those for $U/t = 5.0, 6.0, 8.0$. In contrast, there is no quasi-particle peak and the gap gradually opens.

but leads to the infinitesimal transition point. It is also our aim to construct the simple method which gives the infinitesimal Mott transition point.

4.2.1 Results of Linearized Cellular Dynamical Mean Field Theory

We now study the metal-insulator transition in the square lattice Hubbard model by means of the linearized cellular dynamical mean field theory. In Fig. 4.1, we first show the density of states $\rho(\omega)$ for several U. In the upper (lower) panel in Fig. 4.1, the density of states in the metallic (insulating) phase is shown. We find that the Mott transition occurs at $U_c/t \sim 5.0$. In the metallic phase, as U/t is increased, the quasi-particle band is renormalized and narrowed near the transition point at $U/t = 4.0$. For $U/t \sim 5.0$, we find that the insulating gap appears. With increasing U/t, the gap gradually increases and the peaks at the gap edges evolve. The transition point $U_c/t \sim 5.0$ we obtain is in good agreement with that obtained by the cellular dynamical mean field theory combined with the continuous-time quantum Monte Carlo method, $U_c/t \sim 6.05$ [145]. In addition, the narrow Mott gap with the pronounced peaks at the gap edges is also described by our linearized scheme as well as by the cellular dynamical mean field theory. Therefore, our linearized scheme is qualitatively good approximation for the Mott transition

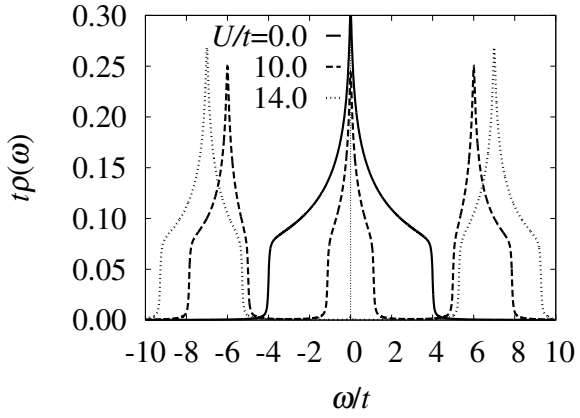

Figure 4.2: Density of states $\rho(\omega)$ for various U obtained by the two-site dynamical mean field theory. For $U/t = 0.0, 10.0$, the system is metallic. As U/t increases, the system undergoes the Mott transition at $U_c/t = 12$. In the insulating phase, for $U/t = 14.0$, the wide Mott gap appears around the Fermi level.

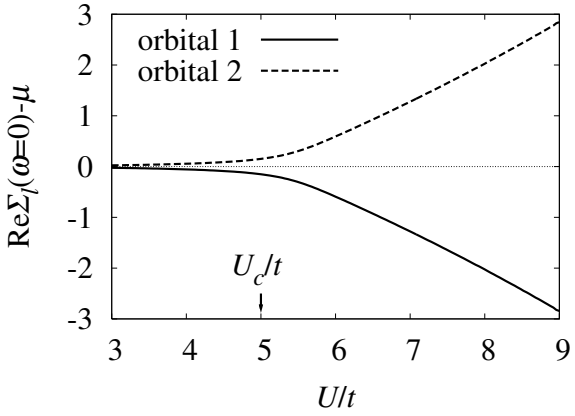

Figure 4.3: $\mathrm{Re}\Sigma_l(\omega = 0) - \mu$ as a function of U. The amplitudes of them abruptly begin to increase linearly at $U = U_c$ as U increases.

in the square lattice.

We note that it is impossible to describe the insulating phase with the narrow gap by using the single-site dynamical mean field theory. As a reference, the density of states calculated by the two-site dynamical mean field theory is shown in Fig. 4.2. In the single-site dynamical mean field theory, as U/t increases, the effective mass gets enhanced and the quasi-particle band is strongly renormalized. At the transition point U_c, the effective mass diverges accompanied by opening the wide Mott gap. The value of the critical interaction strength is also quite different. Our transition point by the linearized cellular dynamical mean field theory is $U_c/t \sim 5.0$ and the transition point by the two-site dynamical mean field theory is $U_c/t = 12.0$. This indicates that the mechanism of the metal-insulator transition in the two-dimensional square lattice is quite different from that of the infinite-dimensional system and the single-site dynamical mean field theory not including the non-local correlations cannot capture the nature of the transition. As discussed in the previous section, the exact Mott-transition point in the square lattice Hubbard model is expected to be infinitesimal U. The cluster extension drastically reduces the critical interaction strength so that it is essentially important.

In order to discuss the mechanism of the Mott transition, we investigate the effective chemical potential for the Green's function on the molecular-orbital basis. In the Green's function in Eq. (4.4), the constant part of the self-energy on the molecular-orbital basis, $\mathrm{Re}\Sigma_l(0)$ leads to the chemical potential shift in the low energy regime. Therefore, we define the effective

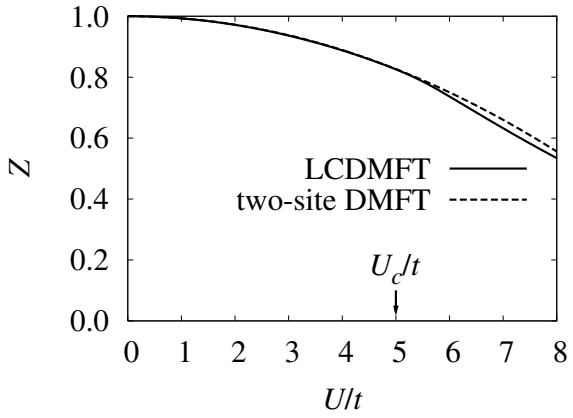

Figure 4.4: The renormalization factor Z as a function of U obtained by the linearized cellular dynamical mean field theory (LCDMFT) and by the two-site dynamical mean field theory (two-site DMFT) for comparison. For $U < U_c$, the renormalization factor Z obtained by the linearized cellular dynamical mean field theory is the very same value as that by the two-site dynamical mean field theory.

chemical potential as $\mu_{\mathrm{eff}l} = \mu - \mathrm{Re}\Sigma_l(0)$. As shown in Fig. 4.3, the difference between the effective chemical potential for the bonding and anti-bonding orbitals, $\mu_{\mathrm{eff2}} - \mu_{\mathrm{eff1}}$, gradually increases with increasing U/t. The difference causes the split of the bonding and anti-bonding bands, and induces the metal-insulator transition, which indicates the antiferromagnetic short-range order. As U/t is further increased, $\mu_{\mathrm{eff2}} - \mu_{\mathrm{eff1}}$ drastically increases for $U > U_c$. Because the size of the insulating gap is proportional to $\mu_{\mathrm{eff2}} - \mu_{\mathrm{eff1}}$, the gap for U_c is very small and it increases with increase of U/t. So, in our theory, the small gap which cannot be reproduced by the single-site dynamical mean field theory is described. We thus conclude that the mechanism of the Mott transition in the square lattice Hubbard model is induced by the antiferromagnetic short-range order. In our theory, this short-range order is described by the well-defined split of the bonding and anti-bonding orbitals.

In the single-site dynamical mean field theory, the renormalization factor Z is regarded as the order parameter of the zero-temperature Mott transition. That is, for finite Z, the system is metallic and is insulating for $Z = 0$. So, investigation of the renormalization factor is important to discuss the difference of the mechanism of the Mott transition. In Fig. 4.4, the renormalization factors Z calculated by the linearized cellular dynamical mean field theory (LCDMFT) and by the two-site dynamical mean field theory

(two-site DMFT) are shown. In the metallic phase, for $U/t < U_c/t \sim 5.0$, Z by the linearized cellular dynamical mean field theory takes almost the same value as that by the two-site dynamical mean field theory. The important point is that Z is finite for $U > U_c$, that is, the effective mass of quasiparticles is finite in the insulating phase. This clearly demonstrates that the divergence of the effective mass is not the mechanism of the Mott transition in the square lattice Hubbard model. In the insulating phase, for $U/t > 5.0$, Z by the linearized cellular dynamical mean field theory becomes smaller than that by the two-site dynamical mean field theory. This is expected to be due to the antiferromagnetic correlations but Z remains finite.

In the two-site dynamical mean field theory, it is known that Z is overestimated for $U < U_c$. Also in the linearized cellular dynamical mean field theory, Z in the metallic phase is larger than that in the ideal cellular dynamical mean field theory [145, 147]. More important difference is the order of the transition. In the ideal cellular dynamical mean field theory, the transition is the first order and in our linearized scheme it is crossover. This is an artifact due to our linearization scheme. To improve this point, it is necessary to increase the number of bath site in the effective cluster model.

In summary, our linearized cellular dynamical mean field theory captures the nature of the Mott transition in the square lattice Hubbard model. We conclude that the mechanism of the Mott transition in this model is the antiferromagnetic short-range order and it is described by split of the bonding and anti-bonding orbitals in our theory. The Mott transition point is drastically reduced by the cluster extension and this result is consistent with that of the ideal cellular dynamical mean field theory. The demerit of our linearized scheme is the order of the transition, which is expected to be improved by increase of the number of bath site in the effective cluster model.

4.2.2 Results of Linearized Dynamical Cluster Approximation

We next apply the linearized dynamical cluster approximation to the square lattice Hubbard model and examine its validity. To investigate the metal-insulator transition, we show the density of states $\rho(\omega)$ for several U in Fig. 4.5. We find that the insulating gap opens for infinitesimal U and the gap gradually increases as U/t is increased. This result is quite different from that of the cellular dynamical mean field theory. In the cellular dynamical mean field theory, there is finite critical interaction strength. In our linearized cellular dynamical mean field theory, as discussed in the previous subsection, the transition point is $U_c/t \sim 5.0$. On the other hand, in the linearized dy-

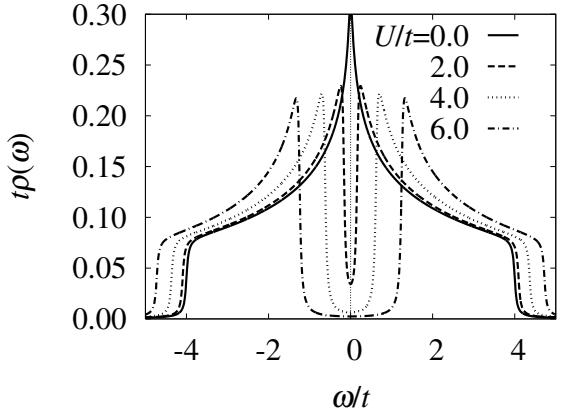

Figure 4.5: Density of states $\rho(\omega)$ for $U/t = 0.0, 2.0, 4.0, 6.0$ obtained by the linearized dynamical cluster approximation. The gap opens for $U/t = 2.0, 4.0, 6.0$.

namical cluster approximation, the transition point is $U_c/t \sim 0$. This result is consistent with that of the ideal two-site cluster dynamical cluster approximation, that is, the dynamical cluster approximation combined with the numerical renormalization group method [151]. As discussed in the previous section, the exact Mott transition point is expected to be $U_c = 0$ in the square lattice Hubbard model due to the perfect nesting. Therefore, our linearized dynamical cluster approximation gives a fairly good approximation and captures the nature of the metal-insulator transition in the Hubbard model on the square lattice. Note that the finite density of states at the Fermi level is due to the finite damping parameter used in numerical computations.

Because our linearized scheme is a simplified method, we obtain several semi-analytical results. This is also a merit of our method. One of useful semi-analytical results is the quasi-particle dispersion. In terms of the linearized self-energy, $\Sigma_{\mathbf{K}}(\omega) \sim \mathrm{Re}\Sigma_{\mathbf{K}}(0) + (1 - 1/Z_{\mathbf{K}})\,\omega$, the Green's function is obtained as,

$$G(\mathbf{k}, \omega) \sim \frac{Z_{\mathbf{K}}}{\omega + i0 - Z_{\mathbf{K}}\,(\varepsilon_{\mathbf{k}} - \mu_{\mathrm{eff}\mathbf{K}})}. \tag{4.12}$$

Here, $\mu_{\mathrm{eff}\mathbf{K}} = \mu - \mathrm{Re}\Sigma_{\mathbf{K}}(0)$. In the above equation, the effective dispersion is naturally defined as $\varepsilon_{\mathrm{eff}\mathbf{k}} \equiv Z_{\mathbf{K}}\,(\varepsilon_{\mathbf{k}} - \mu_{\mathrm{eff}\mathbf{K}})$. In Fig. 4.6, the effective dispersions for $U/t = 0.0, 6.0$ are shown. In the effective dispersion, we can see the clear insulating gap and it gradually increases with increase of U/t. The gap formation is understood by the effective chemical potential shift,

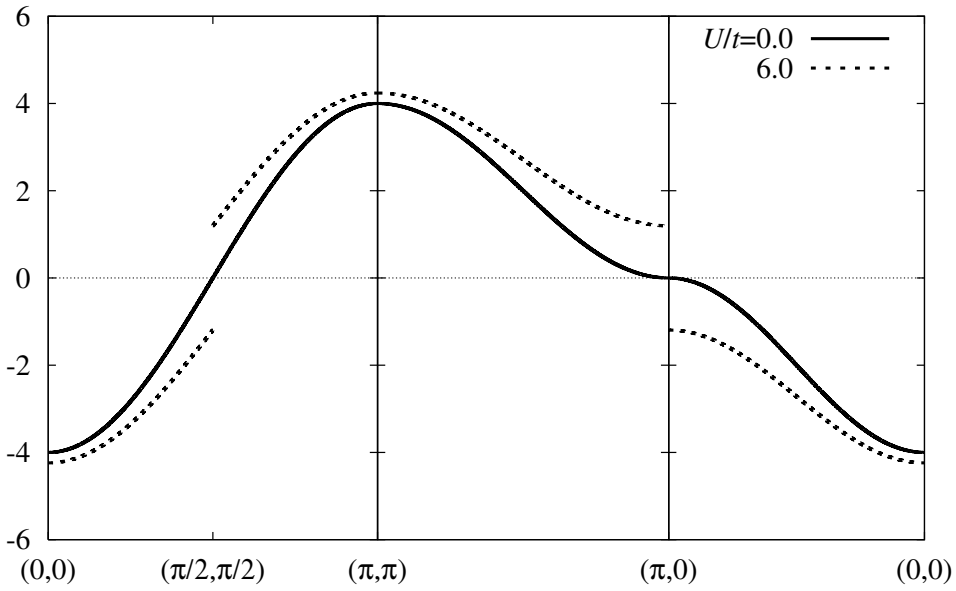

Figure 4.6: Effective dispersion $\varepsilon_{\mathrm{eff}\mathbf{k}}$ for $U/t = 0.0, 6.0$. The effective dispersion for the non-interacting system has no gap, while the open gap appears at the Fermi surface ($|k_x| + |k_y| = \pi$) for finite Coulomb interaction U.

as discussed in the previous subsection. The short-range antiferromagnetic correlations hybridize the $\mathbf{K} = (0, 0)$ and $\mathbf{K} = (\pi, \pi)$ modes, and induce the insulating gap. Also, by the interaction effects, the quasi-particle band-width becomes smaller than the original band-width, which is due to the renormalization factor $Z_{\mathbf{K}}$.

By using the effective dispersion, the size of gap is well defined. In the case of square lattice, $Z_{\mathbf{K}_\Gamma} = Z_{\mathbf{K}_\mathrm{M}}$ and $\mathrm{Re}\Sigma_{\mathbf{K}_\Gamma}(0) = -\mathrm{Re}\Sigma_{\mathbf{K}_\mathrm{M}}(0)$ because of the symmetry. Therefore, the gap has simplified form, $\Delta = 2Z_{\mathbf{K}_\Gamma}|\mathrm{Re}\Sigma_{\mathbf{K}_\Gamma}(0)|$. Note that in this formula, determination of the size of the gap does not suffer from an ambiguity due to the artificial damping parameter. In the left panel of Fig. 4.7, we show the size of the gap Δ/t as a function of U/t. We can clearly see that the size of the gap is non-zero for the infinitesimal U and it gradually increases as U/t increases. In the right panel of Fig. 4.7, for comparison, the gap obtained by the ideal dynamical cluster approximation [131] is shown. In this calculation, up to 64-site cluster model is used and it is solved by the quantum Monte Carlo method. We find that the results are good agreement with our results for $U/t < 8$. For $U/t > 8$, the gap of the dynamical cluster approximation changes its behavior and increases

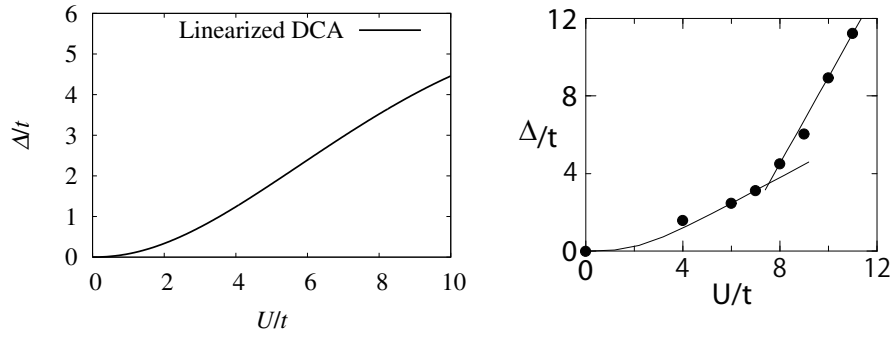

Figure 4.7: The gap Δ as a function of U obtained by the linearized dynamical cluster approximation (left) and Δ at $T/t = 1/128$ by the dynamical cluster approximation combined with the quantum Monte Carlo method [131] (right).

proportionally to U/t. The behavior $U/t > 8$ is different from our results. For $U/t > 8$, our linearized dynamical cluster approximation underestimates the size of the gap. It is due to the linearization of the self-energy. In the strong coupling regime, the insulating gap is originated from the charge excitation, that is, the gap is due to the Hubbard gap. Our linearized dynamical cluster approximation starts from not the real space but $\mathbf{k}$ space and the self-energy is linearized so that our methods cannot reproduce the atomic limit and is not good approximation in the strong coupling regime. Therefore, our linearized dynamical cluster approximation is good in the weak to intermediate coupling regime but not good in the strong coupling regime.

In summary, our linearized cluster dynamical mean field theory has described the Mott transition at infinitesimal U and given semi-analytical results. We have obtained the quasi-particle dispersion, which determines the well-defined size of the gap. The size of the gap is in very good agreement with that of the ideal dynamical cluster approximation for weak to intermediate coupling regime. In the strong coupling regime, our method underestimates the size of the gap. As mentioned in Chap. 2, the cellular dynamical mean field theory is formulated in the real-space while the dynamical cluster approximation is based on wave vector representation. Thereby, the dynamical cluster approximation is suitable to describe the physics in the region where electrons show wave nature, namely, the behavior in the weak to intermediate coupling regime. On the other hand, the cellular dynamical mean field theory is adapted for the strong coupling physics which require the ability to describe localization of electrons. In fact, the linearized dynamical cluster approximation describes the insulating state at infinitesimal U and the

exponentially small gap behavior but does not describe the gap whose size is proportional to U/t in the strong coupling regime. Therefore, both the linearized schemes are complementary.

4.3 Mott Transition in Hubbard Model on Square Lattice with Geometrical Frustration

In this section, we study the Mott transition in the Hubbard model on the square lattice with the next-nearest-neighbor hopping integral t' and discuss the effects of geometrical frustration on the Mott transition. Geometrical frustration has attracted much interest in the field of strongly correlated electron systems. The discovery of heavy fermion behavior in the pyrochlore compound LiV_2O_4 [16–19] and superconductivity in the triangular lattice compound $Na_xCoO_2 \cdot yH_2O$ [157] has stimulated intensive studies of frustrated electron systems. Geometrical frustration has also uncovered new aspects of the Mott metal-insulator transition, which is now one of the central issues in the physics of strongly correlated electron systems. In particular, recent experiments on the triangular lattice organic materials κ-(BEDT-TTF)$_2X$ [20–22, 24, 25] have revealed various interesting physics, such as a novel spin liquid state in the Mott insulating phase, unconventional superconductivity, etc. Since the path integral renormalization group study of the triangular lattice Hubbard model [76], the correlated electrons on the anisotropic triangular lattice have been intensively studied so far [27,134,158]. Another interesting feature in this system is the reentrant behavior of the finite-temperature Mott transition. Recently, this reentrant Mott transition in the moderately frustrated regime has been explained by the cellular dynamical mean field theory [27]. In their paper, common features of the finite-temperature Mott transition in the *paramagnetic* phase are discussed: The critical interaction strength and critical temperature decreases as t' decreases. However, their cellular dynamical mean field theory does not give good approximation in weakly frustrated regime at very low temperature and unified understanding has not yet been obtained. Therefore, it is desirable to systematically study the Mott transition in the weakly frustrated regime at very low temperature. In this section, we study the Mott transition in the *paramagnetic* phase of the square lattice Hubbard model with the next-nearest-neighbor hopping integral by means of the linearized dynamical cluster approximation. At zero temperature, the system should be antiferromagnetically ordered. In the following, however, we investigate the

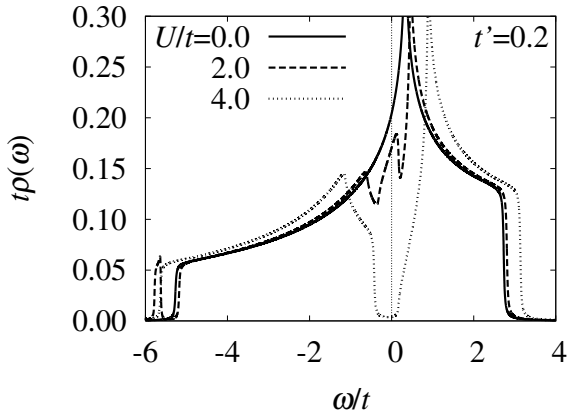

Figure 4.8: Density of states for $U/t = 0.0, 2.0, 4.0$ in the case of $t'/t = 0.2$. For $U/t = 0.0, 2.0$ the system is metallic. On the other hand there exists the open gap for $U/t = 4.0$. This behavior is essentially different from the unfrustrated square lattice Hubbard model where the metallic solution never appears for finite U.

paramagnetic Mott transition at *zero temperature*. This corresponds to investigation of the Mott transition at very low but finite temperature, because at finite temperature, the magnetic order is forbidden by the Mermin-Wagner theorem. Our linearized dynamical cluster approximation is also applicable to calculations at finite temperature.

We now investigate the metal-insulator transition for $t'/t = 0.1$, 0.2, 0.3. In Fig. 4.8, we show the typical density of states for $t'/t = 0.2$. As U/t increases, the gap gradually develops and for $U/t = 4.0$, one can find the clear gap around the Fermi level. The point is that there exists the *finite* critical interaction strength for the Mott transition. This behavior is essentially different from that in the square lattice Hubbard model at $t'/t = 0$. In the square lattice Hubbard model, the system is insulating for any finite U due to the perfect nesting. By introducing frustration, t', the perfect nesting is relaxed and the metallic state is induced.

In a lot of approximated methods, such as the slave-boson mean field theory, variational Monte Carlo, cellular dynamical mean field type approximations, the transition point is of the order of the band-width for $t'/t = 0$ and small t'/t does not change the nature of the *paramagnetic* Mott transition, as mentioned in previous sections. Therefore, in these methods, we cannot discuss the effects of weak frustration on the *paramagnetic* Mott transition. On the other hand, our linearized dynamical cluster approximation,

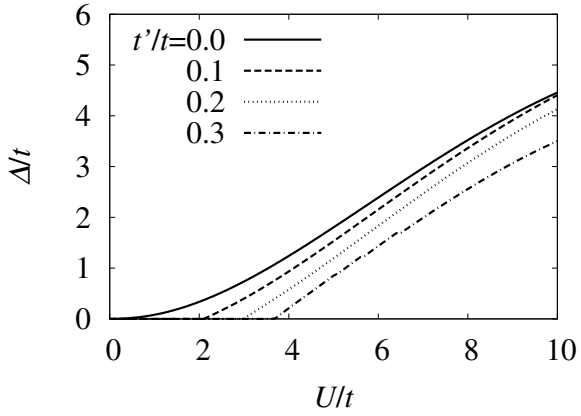

Figure 4.9: Gap Δ as a function of U for $t'/t = 0.0, 0.1, 0.2, 0.3$ calculated in the framework of the linearized dynamical cluster approximation. In the frustrated systems, the gap opens at the finite U unlike the behavior in the unfrustrated systems ($t'/t = 0.0$). As t'/t increases, the critical interaction strength becomes large.

despite of many simplifications, describes the infinitesimal U Mott transition for small t'/t and clarifies the difference between frustrated and unfrustrated systems. This is a surprising result.

In order to clearly see the behavior of the metal-insulator transition, we determine the size of the insulating gap analyzing the effective dispersion. The effective dispersion is calculated in terms of the renormalization factor and effective chemical potential, as well as in the previous section. By using the effective dispersion, the size of gap is computed as,

$$\Delta = Z_{\mathbf{K}_{\rm M}} \left(\varepsilon_{\mathbf{k}=(\pi/2,\pi/2)} - \mu_{\rm eff\mathbf{K}_{\rm M}} \right) - Z_{\mathbf{K}_\Gamma} \left(\varepsilon_{\mathbf{k}=(0,\pi)} - \mu_{\rm eff\mathbf{K}_\Gamma} \right). \tag{4.13}$$

In Fig. 4.9, we show the size of the gap Δ/t for $t'/t = 0.0, 0.1, 0.2, 0.3$. As t'/t is increased, the transition point U_c becomes large. We thus confirm that geometrical frustration stabilizes the metallic state, which is consistent with the result of the previous studies. For $U > U_c$, the gap gradually increases with increase of U. The size of the gap around the transition is much smaller than the size of the Hubbard gap which is of the order of U. This is a similar situation to the case of the unfrustrated system for $t'/t = 0$ and different from the picture of the single-site dynamical mean field theory. Therefore, in our theory, the mechanism of the Mott transition in the weakly frustrated Hubbard model is not the dynamical mean field theory type, *i.e.*, the Brinkmann-Rice + Mott-Hubbard picture, but due to the antiferromagnetic

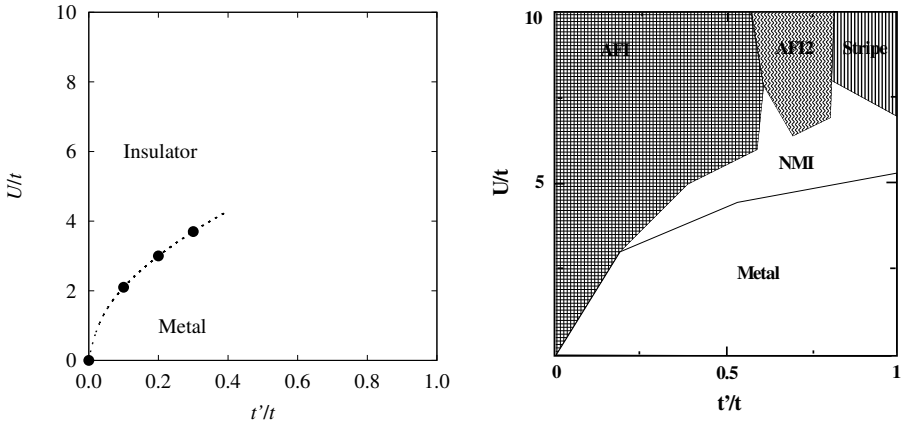

Figure 4.10: Phase diagrams in the t'-U plane obtained by the linearized dynamical cluster approximation (left) and by the path integral renormalization group method [77] (right). The results of the critical value U_c obtained by the linearized dynamical cluster approximation are in good agreement with those by the path integral renormalization group method. In the right panel, NMI and AFI means nonmagnetic and antiferromagnetic insulator, respectively. The difference of AFI and AFI2 phases is the period of the order, namely, AFI phase has 2×2 superstructure and AFI2 phase has 2×4 superstructure. Stripe-ordered insulating phase appears for large t'/t and U/t in the right panel. The dashed line in the left panel is guide to the eyes.

short-range correlations. In weakly frustrated systems, the antiferromagnetic correlations are strong as well as in the perfect square lattice system but the system keeps metallic for small U due to imperfect nesting. For $U > U_c$, the energy of the insulating gap induced by antiferromagnetic short-range order overcomes the kinetic energy and the system becomes insulator.

In the left panel of Fig. 4.10, we summarize our results in the phase diagram in the t'-U plane. For $t'/t = 0$, the system is insulating for any finite U. By introducing the frustration, the metallic phase is induced and as t'/t increases, its region is expanded. As a reference, in the right panel of Fig. 4.10, the phase diagram obtained by the path integral renormalization group method [77] is shown. The path integral renormalization group is expected to be the most sophisticated numerical simulations for the finite-size system in the theoretical methods which is applicable to the frustrated Hubbard models, although it needs extremely high computational costs. We find that, surprisingly, the transition points by the linearized dynamical cluster approximation show very good agreement with those by the path integral renormalization group method. We thus conclude that our theory captures the nature of the Mott transition in weakly frustrated Hubbard models.

Note that the insulating phase obtained by the path integral renormalization group method is the antiferromagnetically ordered in the thermodynamic limit. So, these results may not seem to be comparable. However, the path integral renormalization group results are not expected to drastically change at very low but finite temperature. Therefore, our results are expected to be consistent with the path integral renormalization group results at infinitesimal temperature. In the strongly frustrated regime, $t'/t > 0.5$, there are some important open problems, *e.g.* whether there is the nonmagnetic ground state or not. In our linearized dynamical cluster approximation, however, the two-site cluster effective model is employed so that variations from the perfectly nested square lattice are incorporated by change of the bare dispersion while the frustration effects themselves are not included. Also, our linearized method is not good at strong coupling regime, as discussed in the previous section. As shown in Fig. 4.10, as frustration is strengthened, the transition point becomes large. Therefore, the linearized dynamical cluster approximation used in this study cannot describe the Mott transition in the strongly frustrated regime. To discuss strong frustration, we should improve our formulations and employ the effective model with more than three-site cluster.

In summary, we have studied the *paramagnetic* Mott transition in the weakly frustrated Hubbard model by means of the linearized dynamical cluster approximation. It has been shown that the critical interaction strength of the Mott transition is for $t'/t = 0$ and it gradually increases with increase of t'/t. The phase diagram in the t'-U plane is obtained and it is in surprising agreement with the path integral renormalization group phase diagram. We have obtained the semi-analytical results for the quasi-particle dispersion and insulating gap and concluded that the Mott transition in the weakly frustrated systems is caused by the competition between the antiferromagnetic short-range order and itinerancy of electrons. Our method used in this study cannot describe the Mott transition in the strongly frustrated regime. The improvement of our method to study this regime is our future work.

Chapter 5

Mott Transition in Hubbard Model on Honeycomb Lattice

In the honeycomb lattice, a combination of nontrivial topology and electronic correlations drives a rich variety of phenomena, *e.g.*, superconductivity in MgB_2 [34], layered nitride superconductors [159–161], spin antiferromagnetism in transition metal oxide $InCu_{2/3}V_{1/3}O_3$ [162, 163], topologically driven quantum phase transitions in anyonic quantum liquids [164], and such exotic behaviors currently attract much attention experimentally and theoretically. Further, the honeycomb optical lattice has already been realized by using three coplanar laser beams [165–171]. The discovery of graphene, monolayer graphite, [28, 172, 173] has also promoted research of the honeycomb lattice systems for several years. Graphene has characteristic properties ascribable to propagation of its electrons as massless Dirac fermions in low-energy region and these days various unique behaviors have been reported [50, 174].

The interesting feature of the tight-binding model on the honeycomb lattice is reduction of Fermi surface to two points at half-filling. It results in the existence of pseudogap at Fermi level and linearity of the non-interacting density of states in the low-energy region. Therefore, there is no nesting unlike the square lattice, and the staggered susceptibility $\chi(2\mathbf{k}_{\rm F})$ does not diverge, where $\mathbf{k}_{\rm F}$ denotes the Fermi wave number. In fact, in the Hubbard model on the honeycomb lattice, the static mean field theory predicts that the transition from paramagnetic semi-metal to antiferromagnetic insulator occurs at $U_{\rm AF}/t = 2.23$. This is the first example of Mott-Hubbard transition at finite Hubbard U among two-dimensional bipartite lattices.

Regarding the charge and spin degrees of freedom, an important feature of low-dimensional systems is the presence of strong quantum fluctuations which inhibit long-range order. In particular, the honeycomb lattice has the

minimal possible coordination number $z = 3$ among two-dimensional systems. For example, the square lattice, which is one of typical two-dimensional systems, has the coordination number $z = 4$. For this reason, stronger quantum fluctuations exist in the honeycomb lattice than in the square lattice, where non-local correlations are essentially important to describe the Mott transition as mentioned in the previous chapter. Thus, it is necessary to employ a theory which incorporates non-local correlations such as the cluster dynamical mean field theory in order to investigate the honeycomb lattice.

In the present chapter, we investigate the Mott transition and antiferromagnetism in the Hubbard model on the honeycomb lattice. We first show that quantum fluctuations raise antiferromagnetic transition point strongly by means of the two-site dynamical mean field theory. Further, we address the Mott transition by means of the linearized dynamical cluster approximation and we conclude that nonmagnetic insulating phase is stable in weak to intermediate coupling regime.

5.1 Model and Method

Hubbard model: We now consider the Hubbard Hamiltonian on the honeycomb lattice with the nearest-neighbor hopping integral, $-t$,

$$H = -t \sum_{\langle i,j\rangle,\sigma} c^{\dagger}_{i\sigma} c_{j\sigma} - \mu \sum_{i,\sigma} c^{\dagger}_{i\sigma} c_{i\sigma} + U \sum_{i} n_{i\uparrow} n_{i\downarrow}. \tag{5.1}$$

Here, the summation over $\langle i, j\rangle$ is taken between the nearest-neighbor pair of sites.

Two-site dynamical mean field theory for antiferromagnetic order: The two-site dynamical mean field theory is also useful to investigate antiferromagnetic ordered state. We can evaluate quantum fluctuation effects on antiferromagnetic long-range order. In order to employ the two-site dynamical mean field theory for antiferromagnetic state, the term denoting a virtual staggered magnetic field,

$$h_s \sum_{i,\sigma} e^{i\mathbf{Q}\cdot\mathbf{r}_i} c^{\dagger}_{i\sigma} c_{i\sigma}, \tag{5.2}$$

with $\mathbf{Q} = (\pi, \pi)$ is added to the Hamiltonian (5.1). We use this term only for giving the initial guess of the energy levels of the bath site $\varepsilon_{\mathrm{a}\sigma}$ and the hybridization V_σ, and the limit of $h_s \to 0$ is taken at an early step in the calculation loop. Only the first and second order moments of the bare density

of states,

$$\int d\varepsilon\ \varepsilon\rho_0(\varepsilon) = 0 \tag{5.3}$$

$$\int d\varepsilon\ (\varepsilon - t_0)^2\rho_0(\varepsilon) = 3.0t^2, \tag{5.4}$$

are needed for the self-consistent condition (3.23) in the framework of the two-site dynamical mean field theory. The staggered magnetization is defined as $m \equiv \langle n_\uparrow \rangle - \langle n_\downarrow \rangle$.

Linearized dynamical cluster approximation: The calculation procedure for the honeycomb lattice is basically similar to that for the square lattice as mentioned in the section 4.1. The effective cluster Hamiltonian is the same as that for the square lattice (4.9). Of course, the parameters are different, namely, $\varepsilon_0 = 1.466t$, and the coefficients $\overline{\left(f_0\left(\tilde{\mathbf{k}}\right) + f_1\left(\tilde{\mathbf{k}}\right)\right)^2} = 0.7126t^2$ and $\overline{\left(f_2\left(\tilde{\mathbf{k}}\right)\right)^2} = 0.1369t^2$. It is noteworthy that it is impossible to derive an explicit expression of the Green's function $\overline{\tilde{G}_{\mathrm{lat}l}\left(\tilde{\mathbf{k}}, \omega\right)}$ for the honeycomb lattice system unlike the square lattice system, because the honeycomb lattice is non-Bravais one. In other words, the Green's function in the matrix form $\hat{\tilde{G}}_{\mathrm{lat}}\left(\tilde{\mathbf{k}}, \omega\right)$ is non-diagonal in wave vector representation. So, we should take the summation over $\tilde{\mathbf{k}}$ to obtain $\overline{\tilde{G}_{\mathrm{lat}l}\left(\tilde{\mathbf{k}}, \omega\right)}$ from $\tilde{G}_{\mathrm{lat}l}\left(\tilde{\mathbf{k}}, \omega\right)$ numerically.

5.2 Feature of Honeycomb Lattice Systems

The Hubbard model on the honeycomb lattice has a unique feature unlike the conventional two-dimensional systems such as square lattice systems. In this section, we overview it in brief. For the Hubbard Hamiltonian (5.1), the bare dispersion for two sublattices shown in Fig. 3.5 is given as

$$\hat{\varepsilon}(\mathbf{k}) = \begin{pmatrix} 0 & \varepsilon_{\mathrm{AB}}(\mathbf{k}) \\ \varepsilon^*_{\mathrm{AB}}(\mathbf{k}) & 0 \end{pmatrix}, \tag{5.5}$$

where

$$\varepsilon_{\mathrm{AB}}(\mathbf{k}) = -t\left[\exp\left(\frac{1}{\sqrt{3}}ik_x a'\right) + 2\exp\left(-\frac{1}{2\sqrt{3}}ik_x a'\right)\cos\left(\frac{1}{2}k_y a'\right)\right]. \tag{5.6}$$

The bare dispersion is obtained as the eigenenergies of Eq. (5.5);

$$\varepsilon_{\pm}(\mathbf{k}) = \pm t\sqrt{3 + 2\cos(k_y a') + 4\cos\left(\frac{\sqrt{3}}{2}k_x a'\right)\cos\left(\frac{1}{2}k_y a'\right)}, \tag{5.7}$$

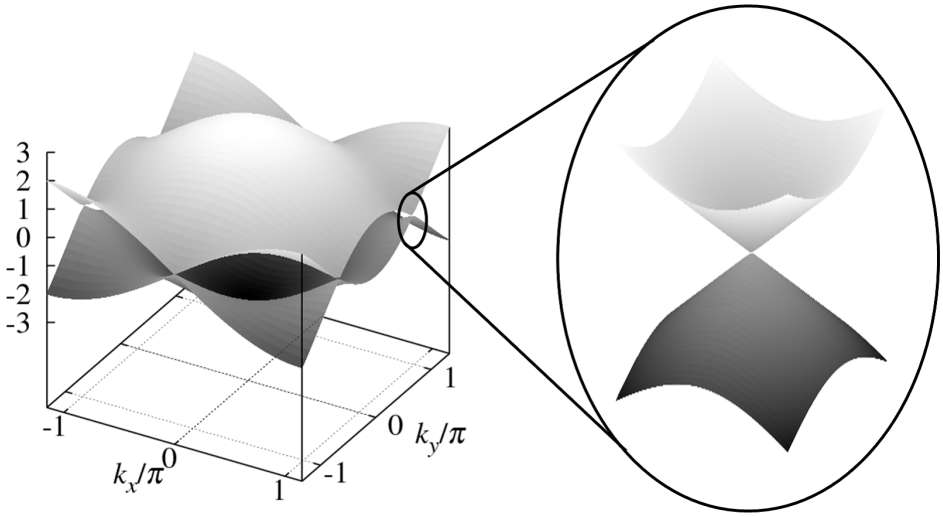

Figure 5.1: Dispersion in the honeycomb lattice (left) and a zoom of it near the K point (right). There are two bands which contact each other only at the K and K′ points. The Dirac cones are located at the K and K′ points.

where the plus (minus) sign applies to the upper (lower) band. This dispersion is linear in the vicinity of K (K′) point,

$$\varepsilon_{\pm}(\mathbf{k}) \sim \pm v_{\mathrm{F}}|\mathbf{k} - \mathbf{k}_{\mathrm{K/K'}}|, \tag{5.8}$$

where $v_{\mathrm{F}} = (\sqrt{3}/2)ta'$ denotes the Fermi velocity. We show the full band structure and magnify it near the K point in Fig. 5.1. We can see the upper and lower bands contact each other only at the K and K′ points. Therefore the K and K′ points are called Dirac points since the band dispersion forms a Dirac cone at around these points.

The non-interacting density of states $\rho_0(\varepsilon)$ is given explicitly as

$$\rho_0(\varepsilon) = \frac{4}{\pi^2}\frac{|\varepsilon|}{t^2}\frac{1}{\sqrt{Z_0}}K\left(\sqrt{\frac{Z_1}{Z_0}}\right), \tag{5.9}$$

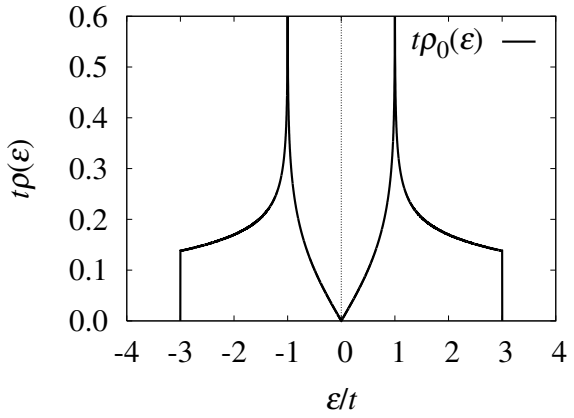

Figure 5.2: Non-interacting density of states $\rho_0(\varepsilon)$. The pseudogap is present at $\varepsilon/t = 0$ and the density of states is linear around it.

where

$$Z_0 = \begin{cases} \left(1 + \left|\frac{\varepsilon}{t}\right|\right)^2 - \frac{[(\varepsilon/t)^2 - 1]^2}{4}, & |\varepsilon/t| \leq 1 \\ 4\left|\frac{\varepsilon}{t}\right|, & 1 \leq |\varepsilon/t| \leq 3 \end{cases}, \tag{5.10}$$

$$Z_1 = \begin{cases} 4\left|\frac{\varepsilon}{t}\right|, & |\varepsilon/t| \leq 1 \\ \left(1 + \left|\frac{\varepsilon}{t}\right|\right)^2 - \frac{[(\varepsilon/t)^2 - 1]^2}{4}, & 1 \leq |\varepsilon/t| \leq 3 \end{cases}, \tag{5.11}$$

which is derived from Eq. (5.7). Here, $K(k)$ is the complete elliptic integral of the first kind for the elliptic modulus k. Around $\varepsilon/t = 0$, the non-interacting density of states (5.9) is approximated by

$$\rho_0(\varepsilon) \sim \frac{1}{\sqrt{3}\,\pi}\frac{|\varepsilon|}{t^2}, \tag{5.12}$$

which reflects the linearity of the dispersion around the Dirac points and means the appearance of pseudogap at $\varepsilon/t = 0$. In Fig. 5.2, the non-interacting density of states is presented. The pseudogap is clearly seen at the Fermi level in Fig. 5.2, which stems from the linear dispersion. Because of the presence of the pseudogap structure, a variety of novel phenomena are expected to be induced.

5.3 Antiferromagnetic Order by Static and Two-Site Dynamical Mean Field Theory

In this section, we first review the analysis by the static mean field theory on the antiferromagnetic long-range order in the Hubbard model on the honeycomb lattice briefly. There we confirm that the results for the honeycomb lattice are quite different from those for the square lattice. Subsequently, we investigate the effects of quantum fluctuations on antiferromagnetic order by means of the two-site dynamical mean field theory.

In the framework of the Hartree-Fock mean field theory, the feature of the honeycomb lattice is taken in through the non-interacting density of states given by Eq. (5.9). The Hartree-Fock mean field theory gives the critical value of the transition to antiferromagnetic insulator $U_{\rm AF}$ as

$$U_{\rm AF}^{-1} = \frac{1}{2}\int_{-\infty}^{0} d\varepsilon \frac{\rho_0(\varepsilon)}{|\varepsilon|}. \tag{5.13}$$

When the non-interacting density of states at the Fermi level is non-zero such as taht for the square lattice, the right-hand side of (5.13) diverges and $U_{\rm AF} = +0$. Meanwhile, in the case of the honeycomb lattice, the non-interacting density of states around $\varepsilon = 0$ is proportional to $|\varepsilon|$, therefore the right-hand side of (5.13) does not diverge and $U_{\rm AF}/t = 2.23$. For $U > U_{\rm AF}$, within the Hartree-Fock mean field theory, the staggered magnetization, $m \equiv \langle n_\uparrow \rangle - \langle n_\downarrow \rangle$, is determined by

$$1 = \frac{1}{2}\int_{-\infty}^{0} d\varepsilon \frac{\rho_0(\varepsilon)}{m^2 + (2\varepsilon/U)^2}. \tag{5.14}$$

Thus, it predicts that staggered magnetization m grows as

$$m \sim 2\pi\sqrt{3}\frac{t^2}{U}\left(\frac{1}{U_{\rm AF}} - \frac{1}{U}\right), \tag{5.15}$$

for small m. The existence of the pheudogap at Fermi level in the non-interacting density of states causes the unusual behavior of magnetization. That is the antiferromagnetic solution by the Hartree-Fock mean field theory, which neglects the quantum fluctuations. Generally the quantum fluctuations stabilize the metallic state and raise the critical value $U_{\rm AF}$. In order to take into account the quantum fluctuation, we next analyze the antiferromagnetic order by means of the two-site dynamical mean field theory.

We first present the staggered magnetization m obtained by the two-site dynamical mean field theory in Fig. 5.3. As a reference, the staggered

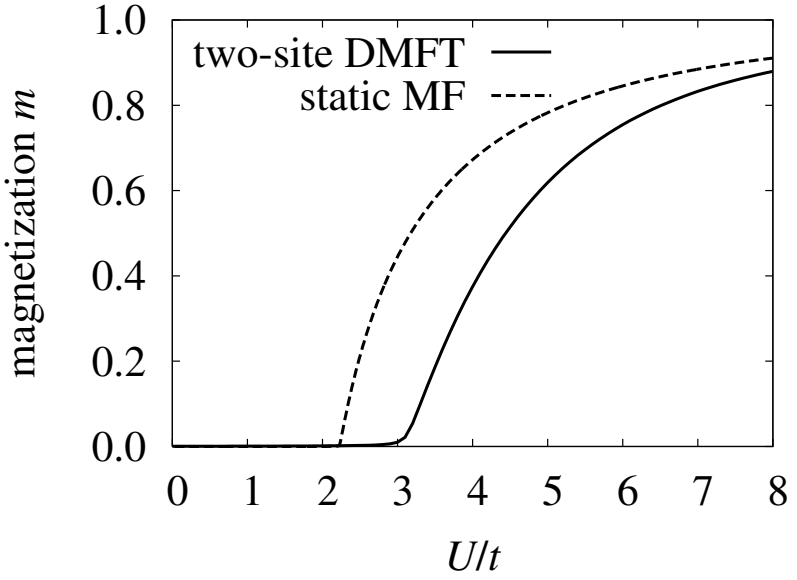

Figure 5.3: U-dependence of the staggered magnetization m by means of two-site dynamical mean field theory (two-site DMFT) and by static mean field theory (static MF) computed via Eq. (5.14).

magnetization by the static mean field theory is also shown in Fig. 5.3. We can see the magnetization $m = 0$ for small U/t. Note that the present system does not show antiferromagnetic long-range order for small U/t, even in the absence of geometric frustration. Further, the magnetization m grows drastically for $U > U_{\rm AF}$ in contrast to square lattice systems where the magnetization grows slowly as U is increased. We find the antiferromagnetic transition point $U_{\rm AF}/t \sim 3.2$ by means of fitting of the results obtained by the two-site dynamical mean field theory for small-m regime via the same function form as (5.15). This value is much larger than that by the static mean field theory. We thus conclude quantum fluctuations strongly raise the antiferromagnetic transition point.

In summary, we have calculated the critical value $U_{\rm AF}/t \sim 3.2$ as a point that staggered magnetization m vanishes by means of fitting of the results obtained by the two-site dynamical mean field theory for small-m regime via the same function form as (5.15). The transition point $U_{\rm AF}/t \sim 3.2$ is much larger than that obtained by the static mean field theory $U_{\rm AF}/t = 2.23$. Therefore we concluded that quantum fluctuations strongly suppress antiferromagnetic long-range order, which is consistent with the results by quantum Monte Carlo simulations [58,59,68], the variational method [60,61] and O(3) nonlinear σ model [67].

5.4 Mott Transition by Linearized Dynamical Cluster Approximation

In this section, we investigate the Mott transition on the honeycomb lattice by applying the linearized dynamical cluster approximation to the Hubbard Hamiltonian (5.1). This method is suitable to describe the Mott transition induced by the moment formation shown in the previous chapter, and thus is expected to provide adequate description of the Mott transition on the honeycomb lattice. In what follows, we assume that there is no long-range order in the system.

The single-particle density of states for various U is firstly shown in Fig. 5.4. We can see that the narrow gap opens at $U = 2.0, 4.0, 6.0$ and that the magnitude of the Mott gap gradually increases as U is increased. Our result shows that the Mott transition occurs at an infinitesimal U on the honeycomb lattice similarly to that on the square lattice. The result is different from those obtained by the other methods which predict it happens at finite U [58, 59, 68]. In order to consider the difference, we estimate the gap Δ. In the framework of the linearized dynamical cluster approximation, the lattice Green's function $\hat{G}_{\mathrm{lat}\sigma}(\mathbf{k}, \omega)$ is given as

$$\hat{G}_{\mathrm{lat}\sigma}(\mathbf{k}, \omega) = \left[(\omega + \mu)\hat{1} - \hat{\varepsilon}(\mathbf{k}) - \hat{\Sigma}_\sigma(\omega) \right]^{-1}. \tag{5.16}$$

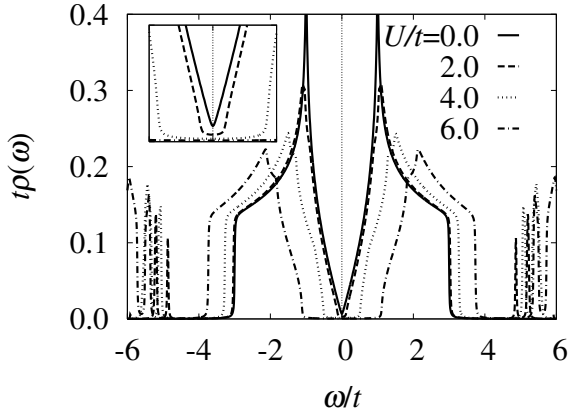

Figure 5.4: Density of states for various U calculated by the linearized dynamical cluster approximation. The open gap appears for finite U. A zoom in of the density of states around the Fermi level is presented in the inset.

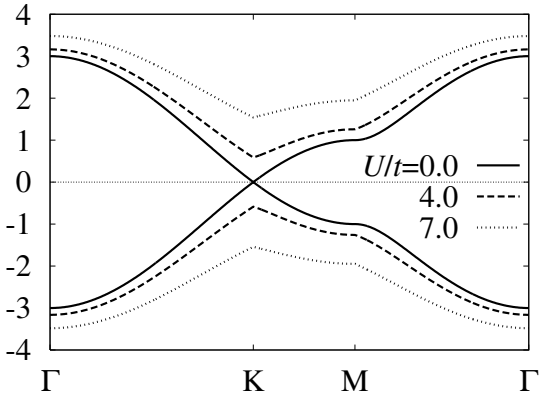

Figure 5.5: Renormalized dispersion for various U. The horizontal axis means the lines in the Brillouin zone, from $\mathbf{k}_\Gamma = (0,0)$ to $\mathbf{k}_\mathrm{K} = (2\pi/\sqrt{3}, 2\pi/3)$, to $\mathbf{k}_\mathrm{M} = (2\pi/\sqrt{3}, 0)$ and to $\mathbf{k}_\Gamma$. At $U = 0$, the upper and lower bands touch each other at the K point, however, they come unstuck for finite U.

Linearly expanding the self-energy in Eq. (5.16), we obtain

$$\hat{G}_{\mathrm{lat}\sigma}(\mathbf{k},\omega) \sim \hat{Z}_\sigma \left[\omega\hat{1} - \hat{Z}_\sigma\left(\hat{\varepsilon}(\mathbf{k}) + \hat{a}_\sigma - \mu\hat{1}\right)\right]^{-1}, \tag{5.17}$$

where $\hat{a}_\sigma = \hat{\Sigma}_\sigma(\omega = 0)$. Thus, we introduce the effective dispersion matrix,

$$\hat{\varepsilon}_{\mathrm{eff}}(\mathbf{k}) \equiv \hat{Z}_\sigma\left(\hat{\varepsilon}(\mathbf{k}) + \hat{a}_\sigma - \mu\hat{1}\right). \tag{5.18}$$

Here, we can compute $\hat{\Sigma}_\sigma$ and $\hat{Z}_\sigma(\omega)$ via the unitary transformation, namely,

$$\hat{\Sigma}_\sigma(\omega) = \hat{U}\hat{\tilde{\Sigma}}_\sigma(\omega)\hat{U}^\dagger \tag{5.19}$$

$$\hat{Z}_\sigma = \hat{U}\hat{\tilde{Z}}_\sigma\hat{U}^\dagger. \tag{5.20}$$

Eventually we obtain the effective dispersion $\varepsilon_{\mathrm{eff}\pm}(\mathbf{k})$ as the eigenvalues of the effective dispersion matrix $\hat{\varepsilon}_{\mathrm{eff}}(\mathbf{k})$. Because we now consider the honeycomb lattice at half-filling with particle-hole symmetry, the following relations are fulfilled;

$$\tilde{a}_{11,\sigma} - \mu = -\left(\tilde{a}_{22,\sigma} - \mu\right) \tag{5.21}$$

$$\tilde{Z}_{11,\sigma} = \tilde{Z}_{22,\sigma}. \tag{5.22}$$

Thereby, the effecitive dispersion matrix $\hat{\varepsilon}_{\mathrm{eff}}(\mathbf{k})$ is rewritten as

$$\hat{\varepsilon}_{\mathrm{eff}}(\mathbf{k}) = \tilde{Z}_{11,\sigma}\begin{pmatrix} 0 & \varepsilon_{\mathrm{AB}}(\mathbf{k}) - (\tilde{a}_{11,\sigma} - \mu) \\ \varepsilon^*_{\mathrm{AB}}(\mathbf{k}) - (\tilde{a}_{11,\sigma} - \mu) & 0 \end{pmatrix}. \tag{5.23}$$

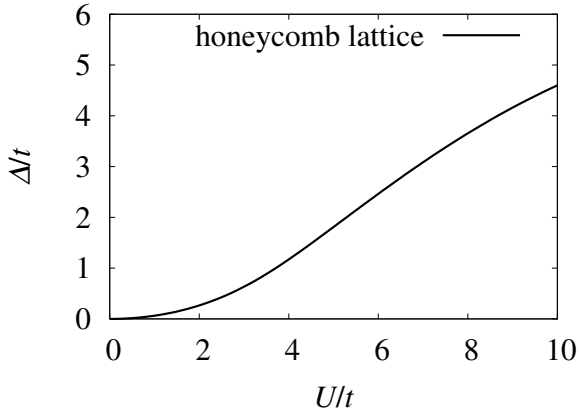

Figure 5.6: U-dependence of gap Δ. The gap Δ is exponentially small but finite for any non-zero U.

By diagonalizing Eq. (5.23), the effective dispersion $\varepsilon_{\text{eff}\pm}(\mathbf{k})$ is obtained as

$$\varepsilon_{\text{eff}\pm}(\mathbf{k}) = \pm\tilde{Z}_{11,\sigma}|\varepsilon_{\text{AB}}(\mathbf{k}) - (\tilde{a}_{11,\sigma} - \mu)|. \tag{5.24}$$

In Fig. 5.5, the effective dispersion computed by Eq. (5.24) for various U is presented. It is drawn that the upper and lower bands contact at K point for $U = 0$ as mentioned in the section 5.2. The semi-analytical investigation allows us to clearly draw the band structure. As increasing U, the two bands move apart from each other. Further, it is found that the effective upper and lower bands has a minimum and maximum value at the K (K′) point respectively for finite U as well as the non-interacting dispersion. In other words, the dispersion only shrinks as U is increased.

We can estimate the value of gap Δ through the effective dispersion Eq. (5.24) as follows;

$$\begin{aligned}\Delta = \min\{\varepsilon_{\text{eff}+}(\mathbf{k}) \quad &| \quad \mathbf{k} \in \text{Brillouin zone}\} \\ - \max\{\varepsilon_{\text{eff}-}(\mathbf{k}) \quad &| \quad \mathbf{k} \in \text{Brillouin zone}\}.\end{aligned} \tag{5.25}$$

Due to the shape of band structure, Eq. (5.25) is specifically transcribed in the case of the honeycomb lattice to

$$\Delta = \varepsilon_{\text{eff}+}(\mathbf{k}_{\mathbf{K}/\mathbf{K}'}) - \varepsilon_{\text{eff}-}(\mathbf{k}_{\mathbf{K}/\mathbf{K}'}). \tag{5.26}$$

The gap generation is shown in Fig. 5.6. As shown in Fig. 5.6, the gap Δ increases with increase of U but the value of gap grows slowly for small U. For this reason, it might be difficult to compute a minute value of gap by

the quantum Monte Carlo simulation due to finite size effects or a statistical error. Perturbation theories from the strong coupling limit are hard to approach $U = 0$ limit. Our results show that the Mott transition occurs at infinitesimal U in the honeycomb lattice systems similarly to that in the square lattice systems caused by non-local correlations. In other words, it is concluded that the mechanism of the Mott transition is the short-range antiferromagnetic correlations which hybridize the two modes both on the honeycomb lattice and on the square lattice and that both the transition points are the same value of infinitesimal U because the hybridization of two modes splits the bands. It implies that the Mott transition in the Hubbard model with only the nearest hopping integral on any bipartite lattice, which is particle-hole symmetric, happens at infinitesimal Hubbard U in general according to the quasi-particle dispersion (5.24). Further, it is quite important that our results conclude that nonmagnetic insulating phase emerges in weak to intermediate coupling regime on the honeycomb lattice because antiferromagnetic long-range order is absent for $U < U_{\rm AF}$ as shown in the previous section.

In summary, we have studied the Hubbard model on the honeycomb lattice by means of the linearized dynamical cluster approximation and shown that the Mott transition point in the honeycomb lattice systems is infinitesimal U similar to that in the square lattice systems. We calculated the quasi-particle dispersion and the gap, and found that the gap slowly increases as U is increased. It was shown that the Mott gap is caused by the short-range antiferromagnetic correlations even though the non-interacting Fermi surface is reduced to the points on the honeycomb lattice. It was found that the split of the bands by non-local correlations is essential to open the Mott gap. According to the absence of antiferromagnetic long-range order for $U/t < U_{\rm AF}/t \sim 3.2$ as shown in the previous section, we concluded that the nonmagnetic insulating state is stable in weak to intermediate coupling regime. This is novel nonmagnetic insulating phase.

Chapter 6

Summary of the Thesis

In this thesis, we proposed novel linearized theories of the cluster dynamical mean field theory. One is the linearized version of the cellular dynamical mean field theory and the other is that of the dynamical cluster approximation. These methods are based on the cluster dynamical mean field theory combined with the exact diagonalization and describe low energy physics by the linearization of the self-energy. Because the linearized cluster dynamical mean field theories are not perturbative methods, they are applicable to any parameter regions from weak to strong coupling regime. Furthermore, these methods need the least number of effective bath sites so that computational costs are much less than the cluster dynamical mean field theory combined with the exact diagonalization. Accordingly, these methods allow us to systematically investigate non-local fluctuation effects at very low computational costs.

We first applied both the methods to the Hubbard model on the square lattice. Our methods are in good agreement with the ideal cellular dynamical mean field theory or dynamical cluster approximation respectively and successfully describe the Mott transition. It is concluded that the mechanism of the Mott transition in this system is antiferromagnetic short-range order. In particular, the linearized dynamical cluster approximation describes the insulating state at any non-zero interaction. Further, the size of Mott gap estimated by means of the linearized dynamical cluster approximation is in very good agreement with that of the ideal dynamical cluster approximation in weak to intermediate coupling regime. We showed that the linearized dynamical cluster approximation is suitable to describe the physics in weak to intermediate coupling regime where electrons represent wave nature. On the other hand, the linearized cellular dynamical mean field theory is adapted for the strong coupling physics which requires the ability to describe localization of electrons. Therefore, both the linearized schemes are complementary.

We next addressed the Mott transition with geometrical frustration by means of the linearized dynamical cluster approximation. We succeeded in systematically describing the Mott transition in the unfrustrated and weakly frustrated square lattice systems and showed that the Mott transition point gradually increases with strengthening geometrical frustration. We have obtained the semi-analytical results for the quasi-particle dispersion and insulating gap, and concluded the Mott transition in the weakly frustrated systems is caused by the competition between the antiferromagnetic short-range order and itinerancy of electrons. To investigate the Mott transition in the strongly frustrated regime, it is necessary to improve our formulation to employ the effective model with more than three-site cluster. This is our future work.

Finally we investigated the Hubbard model on the honeycomb lattice and concluded that the nonmagnetic insulating phase emerges in weak to intermediate coupling regime. We evaluated the antiferromagnetic transition point $U_{\mathrm{AF}}/t \sim 3.2$ by means of the two-site dynamical mean field theory and showed that antiferromagnetic ordered state is absent in weak to intermediate coupling regime, which is quite different from the square lattice system. We subsequently investigated the Mott transition by means of the linearized dynamical cluster approximation. Then we obtained the semi-analytical results for the quasi-particle dispersion and insulating gap, and showed that the Mott transition occurs at infinitesimal interaction strength. We thus concluded that the nonmagnetic insulating state is stable for $U < U_{\mathrm{AF}}$. No materials with honeycomb lattice structure which evidently shows nonmagnetic insulating behavior have been found so far, however, we expect that our findings stimulate and serve for further theoretical and experimental research. The novel methods we proposed, namely the linearized theories of the cluster dynamical mean field theory, are of wide use so that we also expect these schemes to contribute to understanding of various phenomena.

Reference

[1] N. F. Mott, Proc. Phys. Soc. A **62**, 416 (1949).

[2] N. F. Mott, *Metal-Insulator Transition* (Taylor & Francis, London, 1990) 2nd ed.

[3] J. C. Slater, Phys. Rev. **82**, 538 (1951).

[4] M. Imada, A. Fujimori, and Y. Tokura, Rev. Mod. Phys. **70**, 1039 (1998).

[5] D. B. McWhan, A. Menth, J. P. Remeika, W. F. Brinkman, and T. M. Rice, Phys. Rev. B **7**, 1920 (1973).

[6] D. B. McWhan, and A. Menth, Phys. Rev. Lett. **27**, 941 (1971).

[7] A. Georges, G. Kotliar, W. Krauth, and M. J. Rozenberg, Rev. Mod. Phys. **68**, 13 (1996).

[8] F. Aryasetiawan, and O. Gunnarsson, Rep. Prog. Phys. **61**, 237 (1998).

[9] P. Sun, and G. Kotliar, Phys. Rev. Lett. **92**, 196402 (2004).

[10] K Held, O. K. Andersen, M. Feldbacher, A Yamasaki, and Y-F Yang, J. Phys.: Condens. Matter **20**, 064202 (2008).

[11] V. Oudovenko, G. Pálsson, K. Haule, S. Y. Savrasov, and G. Kotliar, cond-mat/0409527.

[12] P. W. Anderson, Mater. Res. Bull. **8**, 153 (1973).

[13] M. P. Shores, E. A. Nytko, B. M. Bartlett, and D. G. Nocera, J. Am. Chem. Soc. 127, 13462 (2005).

[14] J. S. Helton, K. Matan, M. P. Shores, E. A. Nytko, B. M. Bartlett, Y. Yoshida, Y. Takano, A. Suslov, Y. Qiu, J.-H. Chung, D. G. Nocera, and Y. S. Lee, Phys. Rev. Lett. **98**, 107204 (2007).

[15] P. Mendels, F. Bert, M. A. de Vries, A. Olariu, A. Harrison, F. Duc, J. C. Trombe, J. S. Lord, A. Amato, and C. Baines, Phys. Rev. Lett. **98**, 077204 (2007).

[16] S. Kondo, D. C. Johnston, C. A. Swenson, F. Borsa, A. V. Mahajan, L. L. Miller, T. Gu, A. I. Goldman, M. B. Maple, D. A. Gajewski, E. J. Freeman, N. R. Dilley, R. P. Dickey, J. Merrin, K. Kojima, G. M. Luke, Y. J. Uemura, O. Chmaissem, and J. D. Jorgensen, Phys. Rev. Lett. **78**, 3729 (1997).

[17] S. Kondo, D. C. Johnston, and L. L. Miller, Phys. Rev. Lett. **59**, 2609 (1999).

[18] C. Urano, M. Nohara, S. Kondo, F. Sakai, H. Takagi, T. Shiraki, and T. Okubo, Phys. Rev. Lett. **85**, 1052 (2000).

[19] S. Kondo, C. Urano, Y. Kurihara, M. Nohara, and H. Takagi, J. Phys. Soc. Jpn. **69**, Suppl. B. 139 (2000).

[20] Y. Shimizu, K. Miyagawa, K. Kanoda, M. Maesato, and G. Saito, Phys. Rev. Lett. **91**, 107001 (2003).

[21] F. Kagawa, T. Ito, K. Miyagawa, and K. Kanoda, Phys. Rev. B, **69**, 064511 (2004)

[22] F. Kagawa, K. Miyagawa, and K. Kanoda, Nature **436**, 534 (2005).

[23] Y. Kurosaki, Y. Shimizu, K. Miyagawa, K. Kanoda, and G. Saito, Phys. Rev. Lett. **95**, 177001 (2005).

[24] K. Kanoda, J. Phys. Soc. Jpn. **75**, 051007 (2006).

[25] S. Lefebvre, P. Wzietek, S. Brown, C. Bourbonnais, D. Jérome, C. Mézire, M. Fourmigué, and P. Batail, Phys. Rev. Lett. **85**, 5420 (2000).

[26] T. Yoshioka, A. Koga, and N. Kawakami, Phys. Rev. Lett. **103**, 036401 (2009).

[27] T. Ohashi, Tsutomu Momoi, Hirokazu Tsunetsugu, and Norio Kawakami, Phys. Rev. Lett. **100**, 076402 (2008).

[28] K. S. Novoselov, A. K. Geim,S. V. Morosov, D. Jiang, Y. Zhang, S. V. Dubonos, I. V. Gregorieva, and A. A. Firsov, Science **306**, 666 (2004).

[29] P. R. Wallace, Phys. Rev. **71**, 622 (1947).

[30] J. W. McClure, Phys. Rev. **104**, 666 (1956).

[31] J. C. Slonczewski, and P. R. Weiss, Phys. Rev. **109**, 272 (1958).

[32] T. Ando, A. B. fowler, and F. Stern, Rev. Mod. Phys. **54**, 437 (1982)

[33] M. Corso, W. Auwärter, M. Muntwiler, A. Tamai, T. Greber, and J. Osterwalder, Science **303**, 217 (2004).

[34] J. Nagamatsu, N. Nakagawa, T. Muranaka, Y. Zenitani, and J.Akimitsu, Nature (London) **410**, 63 (2001).

[35] G. W. Semenoff, Phys. Rev. Lett. **53**, 2449 (1984).

[36] V. N. Kotov, B. Uchoa, V. M. Pereira, A. H. Castro Neto, and F. Guinea, arXiv: 1012.3484.

[37] O. V. Gamayun, E. V. Gorbar, and V. P. Gusynin, Phys. Rev. B **81**, 075429 (2010).

[38] E. V. Gorbar, V. P. Gusynin, V. A. Miransky, and I. A. Shovkovy, Phys. Rev. B **66**, 045108 (2002).

[39] D. V. Khveshchenko, J. Phys.: Condens. Matter **21**, 075303 (2009).

[40] D. V. Khveshchenko, and H. Leal Nucl. Phys. B **687**, 323 (2004).

[41] G.-Z. Liu, W. Li, and G. Cheng, Phys. Rev. B **79**. 205429 (2009).

[42] J. E. Drut, and T. A. Lähde, Phys. Rev. B **79**. 241405(R) (2009).

[43] J. E. Drut, and T. A. Lähde, Phys. Rev. Lett. **102**. 026802 (2009).

[44] J. E. Drut, and T. A. Lähde, Phys. Rev. B **79**. 165425 (2009).

[45] S. Hands, and C. Strouthos, Phys. Rev. B **78**. 165423 (2008).

[46] V. P. Gusynin, V. A. Miransky, S. G. Sharapov, and I. A. Shovkovy, Phys. Rev. B **74**. 195429 (2006).

[47] D. V. Khveshchenko, Phys. Rev. Lett. **87**. 206401 (2001).

[48] I. L. Aleiner, D. E. Kharzeev, and A. M. Tsvelik, Phys. Rev. B **76**. 195415 (2007).

[49] F. D. M. Haldane, Phys. Rev. Lett. **61**, 2015 (1988).

[50] C. L. Kane, and E. J. Mele, Phys. Rev. Lett. **95**, 226801 (2005).

[51] C.-Y. Hou, C. Chamon, and C. Mudry, Phys. Rev. Lett. **98**, 186809 (2007).

[52] T. Hanisch, B. Kleine, A. Ritzl, and E. Müller-Hartmann, Ann. Phys. **4**, 303 (1995).

[53] N. M. R. Peres, M. A. N. Araújo, and D. Bozi, Phys. Rev. B **70**, 195122 (2004).

[54] J. P. Reed, B. Uchoa, Y. I. Joe, Y. Gan, D. Casa, E. Fradkin, and P. Abbamonte, Science **330**, 805 (2010).

[55] D. V. Khveshchenko, Phys. Rev. Lett. **87**, 206802 (2001).

[56] I. F. Herbut, Phys. Rev. Lett. **97**, 146401 (2006).

[57] C. Honerkamp, Phys. Rev. Lett. **100**, 146404 (2008).

[58] S. Sorella, and E. Tosatti, Europhys. Lett. **19**, 699 (1992).

[59] T. Paiva, R. T. Scalettar, W. Zheng, R. R. P. Singh, and J. Oitmaa, Phys. Rev. B **72**, 085123 (2005).

[60] L. M. Martelo, M. Dzierzawa, L.Siffert, and D. Baeriswyl, Z. Phys. B: Condens. Matter **103**, 335 (1997).

[61] N. Furukawa, J. Phys. Soc. Jpn. **70**, 1483 (2001).

[62] W. Wu, Y.-H. Chen, H.-S. Tao, N.-H. Tong, and W.-M. Liu, Phys. Rev. B **82**, 245102 (2010).

[63] A. Liebsch, arXiv: 1010.4733.

[64] S.-S. Lee, and P. A. Lee, Phys. Rev. Lett. **95**, 036403 (2005).

[65] M. Hermele, Phys. Rev. B **76**, 035125 (2007).

[66] M.-T. Tran, and K. S. Kim, arXiv: 1011.1700.

[67] G. Y. Sun, and S. P. Kou, arXiv: 0911.3002.

[68] Z. Y. Meng, T. C. Lang, S. Wessel, F. F. Assaad, and A. Muramatsu, Nature (London) **464**, 847 (2010).

[69] S. A. Jafari, Eur. Phys. J. B **68**, 537 (2009).

[70] M.-T. Tran, and K. Kuroki, Phys. Rev. B **79**, 125125 (2009).

[71] N. E. Bickers, D. J. Scalapino, and S. R. White, Phys. Rev. Lett. **62**, 961 (1989).

[72] R. Blankenbecler, D. J. Scalapino, and R. L. Sugar, Phys. Rev. D **24**, 2278 (1981).

[73] J. E. Hirsch, Phys. Rev. B **31**, 4403 (1985).

[74] S. R. White, D. J. Scalapino, R. L. Sugar, E. Y. Loh, J. E. Gubernatis, and R. T. Scalettar, Phys. Rev. B **40**, 506 (1989).

[75] M. Imada, and T. Kashima, J. Phys. Soc. Jpn. **69**, 2723 (2000).

[76] T. Kashima, and M. Imada, J. Phys. Soc. Jpn. **70**, 2287 (2001).

[77] T. Mizusaki, and M. Imada, Phys. Rev. B **74**, 014421 (2006).

[78] T. Yoshioka, A. Koga, and N. Kawakami, J. Phys. Soc. Jpn. **77**, 104702 (2008).

[79] W. Metzner, and D. Vollhardt, Phys. Rev. Lett. **62**, 324 (1989).

[80] J. W. Negele, and H. Orland, *Quantum Many-Particle Systems*, edited by D. Pines (PERSEUS BOOKS, 1987).

[81] J. Hubbard, Prc. Roy. Soc. (London) A **284**, 401 (1964).

[82] A. Georges, and G. Kotliar, Phys. Rev. B **45**, 6479 (1992).

[83] M. Jarrell, Phys. Rev. Lett. **69**, 168 (1992).

[84] X. Y. Zhang, M. J. Rozenberg, and G. Kotliar, Phys. Rev. Lett. **70**, 1666 (1993).

[85] M. Caffarel, and W. Krauth, Phys. Rev. Lett. **72**, 1545 (1994).

[86] D. S. Fisher, G. Kotliar, and G. Moeller, Phys. Rev. B **52**, 17112 (1995).

[87] H. Kajueter, and G. Kotliar, Phys. Rev. Lett. **77**, 131 (1996).

[88] R. Bulla, Phys. Rev. Lett. **83**, 136 (1999).

[89] M. J. Rozenberg, Phys. Rev. B **55**, R4855 (1997).

[90] K. Held, and D. Vollhardt, Eur. Phys. J. B **5**, 473 (1998).

[91] J. E. Han, M. Jarrell, and D. L. Cox, Phys. Rev. B **58**, R4199 (1998).

[92] Th. Maier, M. B. Zölfl, Th. Pruschke, and J. Keller, Eur. Phys. J. B **19**, 377 (1999).

[93] T. Momoi, and K. Kubo, Phys. Rev. B **58**, R567 (2000).

[94] V. S. Oudovenko, and G. Kotliar, Phys. Rev. B **65**, 075102 (2002).

[95] S. Florens, A. Georges, G. Kotliar, and O. Parcollet, Phys. Rev. B **66**, 205102 (2002).

[96] A. Koga, Y. Imai, and N. Kawakami, Phys. Rev. B **66**, 165107 (2002).

[97] A. Koga, N. Kawakami, T. M. Rice and M. Sigrist, Phy. Rev. Lett. **92**, 216402 (2004).

[98] M. Jarrell, H. Akhlaghpour, and T. Pruschke, Phys. Rev. Lett. **70**, 1670 (1993).

[99] T. Mutou, and D. S. Hirashima, J. Phys. Soc. Jpn. **64**, 4799 (1995).

[100] Th. Pruschke, R. Bulla, and M. Jarrell, Phys. Rev. B **61**, 12799 (2000).

[101] Y. Shimizu, O. Sakai, and A. C. Hewson, J. Phys. Soc. Jpn. **69**, 1777 (2000).

[102] N. S. Vidhyadhiraja, V. E. Smith, D. E. Logan, and H. R. Krishnamurthy, J. Phys.: Condens. Matter **15**, 4045 (2003).

[103] R. Sato, T. Ohashi, A. Koga, and N. Kawakami, J. Phys. Soc. Jpn. **73**, 1864 (2004).

[104] G. Kotliar, S. Y. Savrasov, G. Pálsson, and G. Biroli, Phys. Rev. Lett. **87**, 186401 (2001).

[105] A. I. Lichtenstein, and M. I. Katsnelson, Phys. Rev. B **62**, 9283(R) (2000).

[106] P. G. J. von Dongen, Phys. Rev. B **50**, 14016 (1994).

[107] A. Shiller, and K. Ingersent, Phys. Rev. Lett. **75**, 113 (1995).

[108] Tran Minh-Tien, Phys. Rev. B **58**, 15965 (1998).

[109] S. Sachdev, and J. Ye, Phys. Rev. Lett. **70**, 3339 (1993).

[110] J. L. Smith, and Q. Si, Phys. Rev. B **61**, 5184 (2000).

[111] R. Chitra, and G. Kotliar, Phys. Rev. B **63**, 115110 (2001).

[112] A. Toschi, A. A. Katanin, and K. Held, Phys. Rev. B **75**, 045118 (2007).

[113] A. N. Rubtsov, M. I. Katsnelson, and A. I. Lichtenstein, Phys. Rev. B **77**, 033101 (2008).

[114] S. Brener, H. Hafermann, A. N. Rubtsov, M. I. Katsnelson, and A. I. Lichtenstein, Phys. Rev. B **77**, 195105 (2008).

[115] H. Hafermann, S. Brener, A. N. Rubtsov, M. I. Katsnelson, and A. I. Lichtenstein, J. Exp. Theor. Phys. Lett. **86**:10, 677 (2007).

[116] G. Biroli, and G. Kotliar, Phys. Rev. B **65**, 155112 (2002).

[117] G. Biroli, O. Parcollet, and G. Kotliar, Phys. Rev. B **69**, 205108 (2004).

[118] M. H. Hettler, A. N. Tahvildar-Zadeh, M. Jarrell, T. Pruschke, and H. R. Krishnamurthy, Phys. Rev. B **58**, R7475 (1998).

[119] M. H. Hettler, M. Mukherjee, M. Jarrell, and H. R. Krishnamurthy, Phys. Rev. B **61**, 12739 (2000).

[120] Th. Maier, M. Jarrell, Th. Pruschke, and J. Keller, Eur. Phys. J. B **13**, 613 (2000).

[121] M. Jarrell, Th. Maier, C. Huscroft, and S. Moukouri, Phys. Rev. B **64**, 195130 (2001).

[122] C. J. Bolech, S. S. Kancharla, and G. Kotliar, Phys. Rev. B **67**, 075110 (2003).

[123] M. Capone, M. Civelli, S. S. Kancharla, C. Castellani, and G. Kotliar, Phys. Rev. B **69**, 195105 (2004).

[124] M. Civelli, M. Capone, S. S. Kancharla, O. Parcollet, and G. Kotliar Phys. Rev. Lett. **95**, 106402 (2005).

[125] P. Sun, and G. Kotliar, Phys. Rev. Lett. **95**, 016402 (2005).

[126] T. Ohashi, N. Kawakami, and H. Tsunetsugu, Phys. Rev. Lett. **97**, 066401 (2006).

[127] Y. Furukawa, T. Ohashi, Y. Koyama, and N. Kawakami, Phys. Rev. B **82**, 161101(R) (2010).

[128] A. I. Poteryaev, A. I. Lichtenstein, and G. Kotliar, Phys. Rev. Lett. **93**, 086401 (2004).

[129] G. Biroli, O. Parcollet, and G. Kotliar, Phys. Rev. B **69**, 205108 (2004).

[130] C. Huscroft, M. Jarrell, Th. Maier, S. Moukouri, and A. N. Tahvildarzadeh, Phys. Rev. Lett. **86**, 139 (2001).

[131] S. Moukouri, and M. Jarrell, Phys. Rev. Lett. **87**, 167010 (2001).

[132] K. Aryanpour, M. H. Hettler, and M. Jarrell, Phys. Rev. B **67**, 085101 (2003).

[133] M. Jarrell, T. Maier, M. H. Hettler, and A. N. Tahvildarzadeh, Europhys. Lett. **56**, 563 (2001).

[134] Y. Imai, and N. Kawakami, Phys. Rev. B **65**, 233103 (2002).

[135] P. Werner, A. Comanac, L. de' Medici, M. Troyer, and A. J. Millis, Phys. Rev. Lett. **97**, 076405 (2006).

[136] M. Caffarel, and W. Krauth, Phys. Rev. Lett. **72**, 1545 (1994).

[137] A. Georges, and G. Kotliar, Phys. Rev. B **45**, 6479 (1992).

[138] X. Y. Zhang, M. J. Rozenberg, and G. Kotliar, Phys. Rev. Lett. **70**, 1666 (1993).

[139] H. Kajueter, and G. Kotliar, Phys. Rev. Lett. **77**, 131 (1996).

[140] H. Keiter, and G. Morandi, Phys. Rep. **109**, 227 (1984).

[141] N. E. Bickers, Rev. Mod. Phys. **59**, 845 (1987).

[142] M. Potthoff, Phys. Rev. B **64**, 165114 (2001).

[143] W. F. Brinkman, and T. M. Rice, Phys. Rev. B **2**, 4302 (1970).

[144] E. C. Carter, and A. J. Schofield, Phys. Rev. B **70**, 045107 (2004).

[145] H. Park, K. Haule, and G. Kotliar, Phys. Rev. Lett. **101**, 186403 (2008).

[146] T. D. Stanescu, M. Civelli, K. Haule, and G. Kotliar, Ann. Phys. **321**, 1682 (2006).

[147] Y. Z. Zhang, and M. Imada, Phys. Rev. B **76**, 045108 (2007).

[148] M. Balzer, B. Kyung, D. Sénéchal, A.-M. S. Tremblay, and M. Potthoff, Europhys. Lett. **85**, 17002 (2009).

[149] G. Li, W. Hanke, A. N. Rubtsov, S. Bäse, and Michael Potthoff, Phys. Rev. B **80**, 195118 (2009).

[150] T. D. Stanescu, and P. Phillips, Phys. Rev. B **64**, 235117 (2001).

[151] T. Pruschke, R. Zitzler, T. A. Maier, and M. Jarrell, in High Performance Computing in Science and Engineering, Munich 2004, Springer Berlin Heidelberg (2005)

[152] M. Vekić, and S. R. White, Phys. Rev. B **47**, 1160 (1993).

[153] P. Nozières, Eur. Phys. J. B **6**, 447 (1998).

[154] J. R. Schrieffer, X. G. Wen, and S. C. Zhang, Phys. Rev. B **39**, 11663 (1989).

[155] P.W. Anderson, Adv. Phys. **46**, 3 (1997); in *The Theory of Superconductivity in the High-T_c Cuprates*, Princeton Series in Physics (Princeton University Press, Princeton, 1997), pp. 291-294.

[156] T. Maier, M. Jarrell, T. Pruschke, and M. H. Hetter, Rev. Mod. Phys. **77**, 1027 (2005).

[157] K. Takada, H. Sakurai, E. Takayama-Muromachi, F. Izumi, R. A. Dilanian, and T. Sasaki, Nature (London) **422**, 53 (2003).

[158] O. Parcollet, G. Biroli, and G. Kotliar, Phys. Rev. Lett. **92**, 226402, (2004).

[159] H. Tou, Y. Maniwa, T. Koiwasaki, and S. Yamanaka, Phys. Rev. Lett. **86**, 5775 (2001).

[160] Y. Taguchi, M. Hisakabe, and Y. Iwasa, Phys. Rev. Lett. **94**, 217002 (2005).

[161] A. Kitora, Y. Taguchi, and Y. Iwasa, J. Phys. Soc. Jpn. **76**, 023706 (2007).

[162] V. Kataev, A. Möller, U. Löw, W. Jung, N. Schittner, M. Kriener, and A. Freimuth, J. Magn. Magn. Mater. **290**, 310 (2005).

[163] M. Yehia, E. Vavilova, A. Möller, T. Taetz, U. Löw, R. Klingeler, V. Kataev, and B. Büchner, Phys. Rev. B **81**, 060414(R) (2010).

[164] C. Gils, S. Trebst, A. Kitaev, A. W. W. Ludwig, M. Troyer, and Z. Wang, Nat. Phys. **5**, 834 (2009).

[165] G. Grynberg, Phys. Rev. Lett. **70**, 2249 (1993).

[166] A. M. Dudarev, R. B. Diener, I. Carusotto, and Q. Niu, Phys. Rev. Lett. **92**, 153005 (2004).

[167] C. Wu, D. Bergman, L. Balents, and S. Das Sarma, Phys. Rev. Lett. **99**, 070401 (2007).

[168] C. Wu, and S. Das Sarma, Phys. Rev. B **77**, 235107 (2008).

[169] L.-M. Duan, E. Demler, and M. D. Lukin, Phys. Rev. Lett. **91**, 090402 (2003).

[170] S. L. Zhu, B. G Wang, and L.-M. Duan, Phys. Rev. Lett. **98**, 260402 (2007).

[171] K. L. Lee, B. Grémaud, R. Han, B.-G. Englert, and C. Miniatura, Phys. Rev. A **80**, 043411 (2009).

[172] A. K. Geim, and K. S. Novoselov, Nature Materials **6**, 183 (2007).

[173] A. H. Castro Neto, F. Guinea, N. M. R. Peres, K. S. Novoselov, and A. K. Geim, Rev. Mod. Phys. **81**, 109 (2009).

[174] V. P. Gusynin, and S. G. Sharapov, Phys. Rev. Lett. **95**, 146801 (2005).